Advances in the modelling of *in-situ* powder diffraction data

Melanie Müller

Advances in the modelling of *in-situ* powder diffraction data

Von der Fakultät Chemie der Universität Stuttgart zur Erlangung der Würde eines Doktors der Naturwissenschaften (Dr. rer. nat.) genehmigte Abhandlung

Vorgelegt von

Melanie Müller

aus Stuttgart

Hauptberichter: Prof. Dr. R. E. Dinnebier

Mitberichter: Prof. Dr. F. Gießelmann

Zweiter Mitberichter: Prof. Dr. P. Scardi

Mitprüfer: Prof. Dr. T. Schleid

Tag der mündlichen Prüfung: 29.11.2013

Max-Planck-Institut für Festkörperforschung, Stuttgart

Università degli Studi di Trento

2013

Approved by:

Prof. Paulo Scardi

Department of Civil, Mechanical and Environmental Engineering, University of Trento, Italy

Prof. Robert Dinnebier

Max Planck Institute for Solid State Research, Stuttgart, Germany

Ph. D. Commission:

Prof. Antonio Marigo

Department of Chemical Sciences, University of Padova, Italy

Prof. Frank Gießelmann

Institute for Physical Chemistry, University of Stuttgart, Germany

Prof. Thomas Schleid

Institute for Inorganic Chemistry, University of Stuttgart, Germany

Preface

This thesis was made in the frame of a cotutelle agreement between the University of Trento (Italy) and the University of Stuttgart (Germany). The research work was carried out at the University of Trento and the Max Planck Institute for Solid State Research (Stuttgart, Germany).

Table of Contents

Abbreviations

9-MA	9-methylanthracene
AC	atomic coordinates
acac	acetylacetonate
CIF	Crystallographic Information File
CZTS	Cu_2ZnSnS_4
EDX	energy dispersive X-ray spectroscopy
esd	estimated standard deviation
ESRF	European Synchrotron Research Facility
FT	Fourier transform
FWHM	Full Width at Half Maximum
IB	integral breadth
irrep	irreducible representation
JMAK	Johnson-Mehl-Avrami-Kolmogorov
HS	high symmetry
HT	high temperature
LS	low symmetry
LT	low temperature
OA	oriented attachment
OW	Ostwald ripening
RB	rigid body
RM	rigid body symmetry mode
RT	room temperature
SEM	scanning electron microscopy
SLG	soda lime glass
SM	symmetry mode
SRXRD	Synchrotron Radiation X-ray Diffraction
TT	thermal treatment
UV	ultraviolet
WPPD	Whole Powder Pattern Decomposition
WPPF	Whole Powder Pattern Fitting
WPPM	Whole Powder Pattern Modelling
XRD	X-ray diffraction

1 Introduction

1.1 *In-situ* powder diffraction

In-situ powder diffraction is one of the most popular and powerful methods to analyse processes which occur within materials once they are subjected to a non-ambient environment. The method itself is non-contact and (mostly) non-destructive and allows following changes in crystal structure, microstructure and phase composition (Norby & Schwarz, 2008). With the development of fast detectors and increased brilliance of 3rd generation synchrotrons, powder diffraction pattern can nowadays be recorded within seconds, making data analysis of huge numbers of datasets a challenge.

Depending on the aim of an *in-situ* diffraction study, there are different methods that can be used to model the obtained data. One popular method of analysing X-ray powder diffraction data is Rietveld refinement. In 1967, Hugo Rietveld (Rietveld, 1967; Rietveld, 1969) developed a method that allows refining structural parameters (atomic positions) from neutron powder diffraction data taking overlapping reflections into account. Starting 1977, the method was also applied to X-ray powder diffraction data (Malmros & Thomas, 1977; Khattak & Cox, 1977; Young *et al.*, 1977). With the development of the method of Pawley (1981), the refinement of unit cell parameters and the extraction of peak intensities from a powder diffraction pattern became possible. A different approach to intensity extraction using the Rietveld recursive formula was later developed by Le Bail *et al.* (1988).

Within the following years, the application of the Rietveld method has been extended to the extraction of non-structural sample properties, e.g. quantitative phase analysis (Hill & Howard, 1987; Bish & Howard, 1988). Furthermore, the influence of the sample microstructure to the peak profile observed in a powder diffraction pattern was also implemented into modelling using the Rietveld approach. The first notice of the influence of the coherent scattering domain[1] size on the peak width observed in a

---

[1] Throughout the thesis the word „domain" will always be used in the sense of coherent scattering domain.

powder diffraction pattern was already made by Scherrer in 1918 (Scherrer, 1918). 69 years later, these findings were introduced into Rietveld refinement by Thompson *et al.* (1987). Among further microstructural effects, which were integrated to Rietveld refinement, are e.g. a phenomenological description of sample texture (Popa, 1992) or a phenomenological model of anisotropic strain broadening (Stephens, 1999).

Recently, the extended method of parametric Rietveld refinement was described (Stinton & Evans, 2007). It allows modelling of *in-situ* powder diffraction data recorded in dependence on external variables (temperature, pressure, time, …) using physically based or phenomenological functions.

A more elaborate way to directly analyse the microstructure of a material is Whole Powder Pattern Modelling (WPPM) (Scardi & Leoni, 2002). In contrast to traditional X-ray line profile analysis methods, like integral breadth methods as the Scherrer formula (Scherrer, 1918) or the Williamson-Hall plot (Williamson & Hall, 1953), which were used for decades, in this approach a powder diffraction pattern is modelled by lattice parameters and defect content (density, outer cut-off radius, and contrast factor of dislocations, twin and deformation fault probabilities, mean and variance of a grain-size distribution, …).

The analysis of X-ray diffraction data is strongly dependent on the investigated material and its peculiarities as well as the desired information. Whole powder pattern fitting (WPPF) methods (as e.g. the Rietveld method) on one hand and WPPM on the other hand, use both the same type of data, though they are suited for different problems. The information obtained with the respective method is specific.

1.2   Thesis outline

The aim of the present thesis is to present the application of WPPF and WPPM to *in-situ* powder diffraction data and to illustrate differences and peculiarities of these methods focusing on two different questions:

1) the analysis of structural phase transition using WPPF:

Rietveld refinement and parametric Rietveld refinement are used to model *in-situ* powder diffraction data of structural phase transitions for a selection of materials with different properties. Special focus is given on the improvement of the structural description of the investigated materials. Different approaches to describe the crystal structure like symmetry modes (Perez-Mato, 2010), polyhedral tilting, rigid body symmetry modes (Müller *et al.*, 2013) among others are used. Depending on the analysed material and its structural peculiarities, the most appropriate description is determined.

2) the analysis of nanocrystalline grain growth using WPPM:

The dependence of preparation conditions in sol-gel synthesis on the properties (e.g. crystal shape and size) of the obtained material as well as their influence on the nanocrystalline growth kinetics are studied using WPPM. Analysis is performed for CeO_2 and Cu_2ZnSnS_4 as those materials possess actual industrial application.

The present thesis can be divided into three main parts. The first part (chapter II) introduces the methods used during the course of the work and their theoretical background.

In chapter III several examples of structural phase transitions treated by sequential and parametric Rietveld refinement are discussed. Except for the photodimerization kinetics of 9-methylanthracene, all transitions under investigation are temperature dependent.

Chapter IV deals with X-ray diffraction analysis of nanocrystalline materials which were prepared by sol-gel synthesis. For CeO_2 and Cu_2ZnSnS_4 (CZTS) the influence of the preparation conditions on the obtained material and on nanocrystalline grain growth are investigated. In case of CZTS, the applicability of the obtained material was tested within thin film solar cells.

2   Theory

2.1   X-ray powder diffraction

Crystalline materials exhibit a three-dimensional periodic arrangement of atoms. This fact, and X-rays being electromagnetic waves with a wavelength λ, which is in the range of interatomic distances, allows diffraction to occur.

If coherent X-ray radiation hits a crystal, the electrons in its atoms are induced to vibrations, which cause X-ray emission of the same wavelength as the initial radiation. In some directions the emitted rays interfere constructively, while in others they cancel each other. Bragg gave in 1912 an explanation of this phenomenon (Bragg, 1913). He described X-ray diffraction as a reflection of X-rays on atomic layers, the so-called lattice planes, comparable to light which is reflected by a mirror. In contrast to light, X-rays can penetrate the material and are therefore reflected on several equivalent planes. In order to obtain constructive interference, the path length difference, which occurs when X-rays hit two parallel lattice planes with distance d, has to be a multiple of the wavelength λ of the radiation. The path length difference depends on the angle of incidence θ of the X-rays and the distance d of the lattice planes:

$$n\lambda = 2d \sin \theta \qquad \text{Bragg equation.} \qquad (2.1)$$

As previously stated, X-rays are emitted by the electrons, which are bound to atoms and not reflected by planes. Atoms in succeeding planes are not necessarily placed one after another. A scheme of such a situation can be seen in Figure 2.1. It can be proven that the Bragg equation is also valid in such cases (Bloss, 1994).

Still, the difference in path length needs to be a multiple of the wavelength λ. In Figure 2.1, the path length can be described as the two distances $\overline{PN}$ and $\overline{NQ}$, which can be given using the distance $\overline{MN}$ and the respective angles.

This leads to the following equation (Bloss, 1994):

$$n\lambda = \overline{MN}\cos(180° - (\alpha + \theta)) + \overline{MN}\cos(\alpha - \theta) \qquad (2.2)$$

$$= \overline{MN}\left[-\cos(\alpha + \theta) + \cos(\alpha - \theta)\right] \qquad (2.3)$$

$$= 2\overline{MN}\left[\sin\alpha \sin\theta\right]. \qquad (2.4)$$

The distance $\overline{MN}$ can be given in terms of the distance d of the lattice planes and the angle α:

$$\overline{MN} = \frac{d}{\sin\alpha} . \qquad (2.5)$$

Using this in equation (2.4) leads to the Bragg equation:
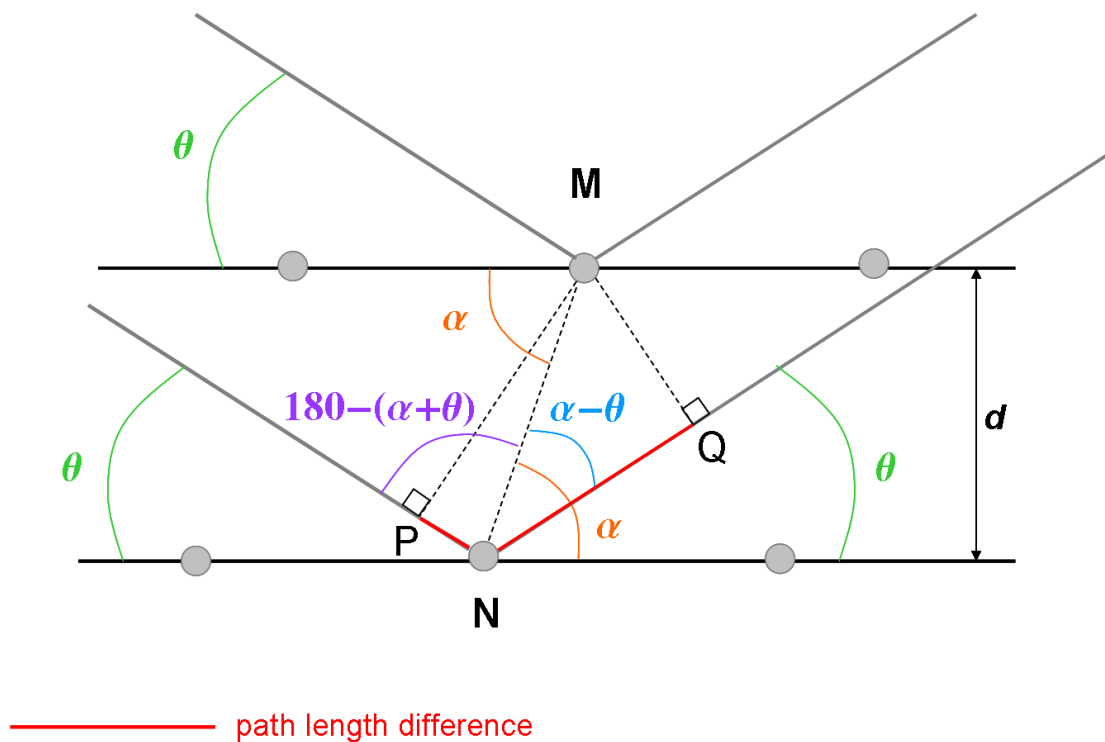
$$n\lambda = 2d\sin\theta . \qquad (2.6)$$

Figure 2.1: Illustration of the Bragg equation.

One of the benefits of powder diffraction is that a powder contains small crystallites, ideally of random orientations. Because of that, there are always some crystals which fulfil the Bragg equation (2.1). For powders the reflected rays form cones with different apex angles. On a screen perpendicular to the direction of the initial beam, the reflected interfered radiation is located on rings, which are called Debye-Scherrer rings. The recorded powder diffraction pattern contains plenty of information about the sample. The position of the peaks $2\theta_0$ provides information about the crystal system, space group and unit cell dimensions. The integral peak intensities are related to the content of the unit cell. The shape and the width of a peak, which is given in terms of the Full Width at Half Maximum (FWHM) or the Integral Breadth[2] (IB), are influenced by domain size and root mean square microstrain (Dinnebier & Billinge, 2008).

Nowadays powder diffraction is widely used for qualitative analysis, quantitative analysis, structure refinement, structure solution and microstructural analysis.

2.2   Full powder pattern analysis

An X-ray powder diffraction pattern can be analysed using different methods depending on sample properties and the desired information. Among them, there are Whole Powder Pattern Fitting (WPPF) and Whole Powder Pattern Modelling (WPPM).

WPPF can be performed using various methods. Some of them require a structural model (e.g. the Rietveld method (Rietveld, 1967)) while others (e.g. the Le Bail (Le Bail *et al.*, 1988) and the Pawley method (Pawley, 1981)) only require knowledge of the lattice parameters and the space group, while the peak intensity is refined and not calculated. The latter are also denoted as Whole Powder Pattern Decomposition (WPPD) methods. In contrast to WPPF, there is the method of WPPM (Scardi & Leoni, 2002). WPPF generally uses arbitrary profile functions to fit the diffraction

---

[2] The Integral Breadth is defined as the ratio of peak area and peak maximum. This equals the width of a rectangle having the same area and the same height as the peak.

patterns. In the WPPM approach instead, physical models of the sample microstructure are applied to analyse the experimental powder diffraction pattern. WPPM is mainly used for nanocrystalline samples (Scardi *et al.*, 2007).

All these methods are based on a least square minimisation process independent from their peculiarities. A minimisation process is performed on the difference between the observed intensity Y_{obs} and a calculated intensity Y_{calc}, which is calculated according to the formalism of the respective method:

$$Min = \sum \left(Y_{obs} - Y_{calc}\right)^2.$$
(2.7)

Even though both approaches, WPPF and WPPM, aim to model the diffraction pattern using a least square minimisation process, the obtained information and the required knowledge about the structure and microstructure of the sample are different.

2.2.1 Pawley and Le Bail fitting

The Pawley and the Le Bail method allow extracting peak intensities from the X-ray powder diffraction pattern without knowledge of the crystal structure, using only lattice parameters and the space group (Pawley, 1981; Le Bail *et al.*, 1988).

In case of the Pawley method within a least square approach, in addition to lattice parameters and profile parameters, all individual peak intensities are freely refined. This can cause problems in case of highly overlapping peaks as negative peak intensities are not excluded within the least square approach. With the number of measured reflections the number of parameters increases. For a huge number of reflections which are weak or heavily overlapped, the method can become numerically unstable (Percharsky & Zavalij, 2009), though nowadays modern Rietveld programs (e.g. TOPAS (Bruker AXS, 2009)) master these problems.

The Le Bail approach can overcome some of these difficulties. During a single least square refinement cycle the intensities of each reflection remain unchanged. At the end of a cycle, intensities are extracted using the Rietveld formula (see chapter 2.2.2)

and the so extracted intensities are used within the next least square refinement cycle. This procedure is performed iteratively until the process converges (Le Bail, 2008). Convergence is usually reached after few cycles. In case of an overestimated background the Le Bail method can also lead to negative peak intensities (Percharsky & Zavalij, 2009).

2.2.2 Rietveld refinement and parametric Rietveld refinement

The Rietveld method was introduced by Hugo Rietveld in the late 1960s (Rietveld, 1967; Rietveld, 1969). He developed this method to overcome problems of overlapping reflections within neutron powder diffraction pattern taking all individual intensities of a step-scanned diffraction pattern with n steps into account (Rietveld, 1993). Thus the angular position $2\theta_i$ within the powder pattern needs to be considered, which can be done using the following equation:

$$2\theta_i = 2\theta_{start} + i\Delta 2\theta \qquad (2.8)$$

(with: $2\theta_{start}$: starting angle; $\Delta 2\theta$: angular step width; $i \in [0,1,....n-1]$ running index).

As stated before, minimisation is performed on the difference between observed intensity Y_{obs} and calculated intensity Y_{calc} which is calculated at any point $2\theta_i$ of the diffraction pattern using the following equation:

$$Y_{calci} = \sum_{ph=1}^{phases}(s_{ph}\sum_{hkl(ph)}(K_{hkl(ph)}\left|F_{hkl}\right|^2\Phi_{hkl(ph)}(2\theta_i - 2\theta_{hkl(ph)}))) + b_{obsi}. \qquad (2.9)$$

The summation is performed over all phases ph that are present in the powder pattern. These phases are scaled with a scaling factor s_{ph}, which is proportional to the weight fraction of each phase. In order to determine the contribution of the different phases at the position $2\theta_i$ within the powder diffraction pattern, which is given by the running index i, a further summation, over all reflections hkl of all phases, contributing to this position is needed. Within this summation over all different reflections hkl, $K_{hkl(ph)}$ represents several correction factors (e.g. Lorentz factor, Polarisation factor,…);

$F_{hkl\text{(ph)}}$ is the structure factor and $\Phi_{hkl\text{(ph)}}(2\theta-2\theta_{hkl\text{(ph)}})$ is the angle dependent profile function which depends on the instrument and the sample (Dinnebier & Müller, 2012). The observed background $b_{\text{obs}i}$ is added.

Before the minimisation process can start, the whole powder diffraction pattern is calculated using a starting model. Within the minimisation process, a weighting factor w_i is introduced for not overestimating peaks with high intensity. In general, there are different definitions of the weighting factor w_i. For this work, a factor as defined in the Rietveld refinement software TOPAS[3] (Bruker AXS, 2009) was applied using the square of the variance of the observed intensity $\sigma(Y_{obs\,i})$ at point i:

$$w_i = \frac{1}{\sigma^2(Y_{obsi})} \,. \tag{2.10}$$

Thus the minimisation formula (equation (2.7)) changes to:

$$Min = \sum_{i=0}^{n-1}(w_i(Y_{obsi} - Y_{calci})^2)\,. \tag{2.11}$$

For *in-situ* powder diffraction a series of measurements is performed in dependence on an external variable (temperature, pressure, time, …)[4]. In *in-situ* powder diffraction usually a huge number of datasets needs to be analysed. Conventionally each powder diffraction pattern is analysed by itself and for all further investigations (e.g. fitting with empirical or physically based functions), the values obtained in those single refinements are used. The approach of parametric Rietveld refinement (Stinton & Evans, 2007) allows refining a series of powder diffraction pattern simultaneously as in this case functional dependencies of parameters are refined instead of refining the single parameter values. This approach is advantageous as the correlation between parameters and the final standard uncertainty can be reduced and non-crystallographic parameters can be refined directly from the measured powder patterns (Stinton & Evans, 2007).

---

[3]Throughout the course of this work all Rietveld refinements were performed using the software TOPAS version 4.2 (Bruker AXS, 2009).

[4] In the present thesis temperature T and time t are used as external variables.

In the following, temperature T is used to define the equations, though any external variable can be treated equally. For each powder diffraction pattern the intensity at each point is a function of several parameters p. Some of those parameters p might be a function of the external variable T. So these parameters can be defined as a function of T and only the parameters of the function are refined. This reduces the total number of parameters drastically. Consequently for parametric Rietveld refinement the minimisation is additionally performed over all patterns (Dinnebier & Müller, 2012):

$$Min = \sum^{patterns}\left(\sum_{i=0}^{n-1}(w_i(Y_{obsi}-Y_{calci}(T))^2)\right). \tag{2.12}$$

2.2.2.1 Agreement factors in Rietveld refinement

For the assessment of the quality of a Rietveld refinement various statistical agreement factors (R-factors) have been introduced. The agreement between the observed and calculated profile is considered in the profile R-factor R_P:

$$R_P = \frac{\sum_{i=0}^{n-1}\left|Y_{obsi}-Y_{calci}\right|}{\sum_{i=0}^{n-1}Y_{obsi}}. \tag{2.13}$$

This value is strongly influenced by the background if the peak to background ratio is low, so that a background corrected R_P' can be defined:

$$R_P{}' = \frac{\sum_{i=0}^{n-1}\left|Y_{obsi}-Y_{calci}\right|}{\sum_{i=0}^{n-1}\left|Y_{obsi}-b_{obsi}\right|}. \tag{2.14}$$

Both R_P and R_P' overemphasize strong reflections, so that a weighting scheme based on the intensities is advisable. This is realised using the weighting factor given in equation (2.10) and can be applied to both previous equations (2.13) and (2.14):

$$R_{wP} = \sqrt{\frac{\sum_{i=0}^{n-1} w_i \left(Y_{obs_i} - Y_{calc_i}\right)^2}{\sum_{i=0}^{n-1} w_i Y_{obs_i}^2}} \qquad (2.15)$$

$$R'_{wP} = \sqrt{\frac{\sum_{i=0}^{n-1} w_i \left(Y_{obs_i} - Y_{calc_i}\right)^2}{\sum_{i=0}^{n-1} w_i \left(Y_{obs_i} - b_{obs_i}\right)^2}} \quad . \qquad (2.16)$$

The expected R-value R_{exp} gives a measure of the value which would be obtained for the best possible fit based on counting statistics. For the calculation of R_{exp} the number of data points M and the number of parameters P are taken into account. Also in this case a background subtracted value (R'_{exp}) is possible.

$$R_{\exp} = \sqrt{\frac{M - P}{\sum_{i=0}^{n-1} w_i Y_{obs_i}^2}} \qquad (2.17)$$

$$R'_{\exp} = \sqrt{\frac{M - P}{\sum_{i=0}^{n-1} w_i \left(Y_{obs_i} - b_{obs_i}\right)^2}} \quad . \qquad (2.18)$$

Using R_{exp} and R_{wP} a further significant measure of the quality of a refinement is the goodness of fit (GOF) which is obtained by dividing R_{wP} by R_{exp}:

$$GOF = \frac{R_{wP}}{R_{\exp}} = \sqrt{\frac{\sum_{i=0}^{n-1} w_i \left(Y_{obs_i} - Y_{calc_i}\right)^2}{M - P}} \quad . \qquad (2.19)$$

2.2.3 Whole Powder Pattern Modelling (WPPM)

Whole powder pattern modelling (WPPM) was developed in order to obtain information about the microstructure of a nanocrystalline sample. In whole powder

pattern modelling the microstructural parameters are refined in the same way as the structural parameters of a sample are used in Rietveld refinement. In WPPM all peaks of a powder diffraction pattern are modelled using physical parameters which describe the microstructure of the sample as well as instrumental effects without the use of arbitrary profile functions as Gaussian or Lorentzian functions.

Among the most important microstructural properties, there are domain[5] size, lattice distortions and lattice faults. The influence of the diffraction domain sizes and shapes and their distribution can be modelled using various shapes and mathematical distribution functions. To model lattice distortion or dislocations, their density, the effective outer cut-off radius, the contrast factor and their character (edge or screw dislocation) need to be considered. Stacking faults can be subdivided in twin and deformation faults. For their implementation two faulting probabilities are needed (Scardi & Leoni, 2002; Scardi & Leoni, 2004).

The intensity of a reflection *hkl* is determined by all contributions from the instrument and the sample and calculated by the following formula:

$$I_{hkl}(s) = \int\limits_{-\infty}^{\infty} T_{hkl}^{IP}(L) A_{hkl}^{D}(L) A_{hkl}^{S}(L) (A_{hkl}^{F} + iB_{hkl}^{F})(L) e^{2\pi iLs} dL . \qquad (2.20)$$

In this equation $T^{IP}(L)$ represents the contribution of the instrument, $A^{D}(L)$ is the Fourier transform (FT) of the contribution of lattice distortions, $A^{S}(L)$ the FT of domain size and shape contribution and $(A^{F} + iB^{F})(L)$ the one from faulting while L is the Fourier length and s the reciprocal distance of the lattice planes (Scardi & Leoni, 2002; Scardi & Leoni, 2004).

In the course of this work, the main feature which was used for modelling of powder diffraction patterns obtained from nanocrystalline materials was the domain shape and size distribution, therefore a more detailed explanation is given on its contribution to the profile.

---

[5] Throughout the thesis the phrase "domain" refers to a coherently scattering domain.

Very early in the history of X-ray diffraction, it was noticed that the domain size of the sample influences the line broadening observed in the diffraction pattern and the following relation was established relating the full width at half maximum (FWHM) of a peak to the edge length Λ of a cube (for domains with a cubic shape) using a cube specific shape factor $K\beta = 2\sqrt{\dfrac{\ln 2}{\pi}}$, the wavelength λ and the Bragg angle θ (Scherrer, 1918):

$$FWHM = 2\sqrt{\frac{\ln 2}{\pi}} \frac{\lambda}{\Lambda} \frac{1}{\cos\theta} \qquad\qquad \text{Scherrer equation.} \qquad\qquad (2.21)$$

Though, a profound understanding of the effect of domain size on a powder diffraction pattern is difficult as no physical principle directly refers to domain morphology because domain size is not a tensor property of a crystal (Scardi & Leoni, 2002; Scardi & Leoni, 2004). The size and the shape of a crystal do not depend on its crystal structure but on preparation technique and treatments. Therefore the crystal shape is independent from the crystal system and frequently simple geometrical shapes (sphere, cube, octahedron, …) are observed (Leoni & Scardi, 2001). Within a real sample a distribution of different domain sizes is likely (Leoni & Scardi, 2001), so crystal shape and size distribution need to be taken into account.

Simple geometric shapes can be characterised by a single length parameter D (e.g. the diameter of a sphere or the edge of a cube). The intensity which is scattered by one small crystal cs with length parameter D is given by (Leoni & Scardi, 2001):

$$I_{cs}(s,D) = k(s)\int_0^\infty A_{CS}(L,D)e^{2\pi i L s} dL. \qquad\qquad (2.22)$$

With $s = 2\sin\theta/\lambda$, L is the length in real space and $A_{cs}(L,D)$ is the Fourier transform (FT) of the diffraction profile for the crystal cs. The prefactor $k(s)$ includes all constants related to experimental geometry.

If a distribution of the length parameter D exists, consequently the crystal volume $V_{cs}(D)$ is summed up in a weight function $w(D) = g(D)V_c(D)$ and the FT of $A(L)$ can be written as (Leoni & Scardi, 2001):

$$A(L) = \frac{\int A_{cs}(L,D)w(D)dD}{\int w(D)dD} . \qquad (2.23)$$

Using such a distribution function, the size Λ, which can be obtained using the Scherrer equation (2.21) is the ratio of the fourth order moment M_4 and the third order moment M_3 of the distribution taking the corresponding shape factor $K\beta$ into account. The $i\text{-}th$ moment M_i of a distribution can be calculated by:

$$M_i = D^i d(D)dD . \qquad (2.24)$$

From this, it follows that Λ is:

$$\Lambda = K\beta \frac{M_4}{M_3} . \qquad (2.25)$$

For the assessment of the quality of modelling basically the same agreement factors as in Rietveld refinement can be used (see equations 2.13 to 2.19).

3   *In-situ* X-ray diffraction analysis of structural phase transitions

The study of phase transitions of materials is of general interest as most material properties are related to the atomic structure of the compound and therefore are different if the crystal structure changes. Soon after the development of X-ray diffraction methods, they were applied to materials at non-ambient conditions e.g. for structure solution of solid carbon dioxide (De Smedt & Keesom, 1925) or nitrogen (Vegard, 1929). Shortly after the development of the Rietveld method (Rietveld, 1967), it was applied to investigate structural changes occurring during phase transitions (e.g. Loopstra, 1970; Hewat, 1973). Nowadays, X-ray powder diffraction is routinely used to analyse such transitions. Modern laboratory powder diffractometers and advanced scattering facilities allow rapid collection of high resolution powder diffraction patterns as a function of parameters like temperature, pressure or simply time. 2D position sensitive detectors enable efficient measurements of a series of powder patterns near a phase transition.

Care must be taken in data analysis: the choice of parameters, especially concerning positional parameters of light atoms, is essential. Sometimes other approaches than the traditional atomic coordinates, might be more suitable for structural descriptions and better/easier to refine. Such an approach is the use of rigid bodies, which were originally developed for single crystal analysis but are applied for description of groups of connected atoms in powder diffraction as well (Dinnebier, 1999). The application of them in structural description is beneficial as the number of parameters is reduced and meaningless changes of individual atomic positions are avoided (Dinnebier, 1999).

Recently symmetry modes (Campbell *et al*., 2006; Orobengoa *et al*., 2009) came into the focus, providing an alternative way to describe the structural changes that happen when partial symmetry loss occurs at a phase transition. Based on the fact, that many crystal structures can be related to a structure with higher symmetry (a parent structure), atomic positions in the low symmetry (LS) structure can be described using the atomic position in the high symmetry (HS) structure plus a distortion vector. Those vectors are defined by one or more symmetry modes. Such modes are order

parameters of the irreducible representations (irrep) of the parent space group symmetry, and have been employed in the determination and direct refinement of displacive superstructures (Campbell *et al.*, 2007; Kerman *et al.*, 2012). Compared to a traditional description based on the coordinates of individual atoms, the symmetry-mode basis has the advantage that nature tends to activate a relatively small fraction of the modes available to a given distortion, so that structural complexity is effectively reduced (Kerman *et al*., 2012).

The rigid body motions encountered in molecular crystals and polyhedral inorganics can be treated strictly in terms of atomic displacements, and therefore can be described using symmetry modes. However, the atoms in the rigid body (RB) will typically possess different symmetry modes which must then be tied together in an unnatural fashion to preserve the internal structure of the RB. This is not a very natural parameter set for a RB containing a large number of atoms. Purely rotational symmetry modes were introduced to address this problem. They are called rigid body symmetry modes (RM) and act directly on position and orientation of a RB, which allows refining rigid body rotations directly in a more practical way (Müller *et al*., 2013).

Depending on the investigated material, its structure and the occurring changes, the most appropriate method to describe structural changes might be different. In the following, the basic features of each method are explained.

3.1   Methodological background

3.1.1   Symmetry mode analysis

The concept of symmetry mode analysis is based on the fact that some crystal structures can be described as a distorted version of a structure with higher symmetry also denoted as parent phase. Distortion in this sense refers to anything that can break the symmetry of the HS structure, e.g. atomic displacement, changes in site occupancy or in directions of magnetic dipoles, so the LS phase will generally have

more structural degrees of freedom than the parent phase. A group-subgroup relationship must exist between the HS parent structure and the LS structure.

The basic idea of describing crystal structures using distortions was already developed in the 1980ies (Kopský, 1980) and even applied in the analysis of structural phase transitions (Zuñiga *et al.*, 1982). At that time symmetry mode decomposition required a deep knowledge of group theory and was therefore difficult and took time for calculation. With the development of free web-based tools (ISODISTORT by Campbell *et al.*, 2006 and AMPLIMODES by Orobengoa *et al.*, 2009) mode decomposition became easy and available to everyone.

The distortions can be classified by the irreducible representations (irrep) of the parent space group symmetry (Stokes *et al.*, 1991) and are referred to as symmetry-adapted distortion modes, or more simply as symmetry modes. The symmetry modes of a given type (e.g. lattice strain, displacement or occupancy) belonging to the same irrep collectively comprise an "order parameter" Q (Stokes *et al.*, 1991). These order parameters tend to place the daughter atoms of a given parent atom onto more general Wyckoff sites and often split a parent atom across multiple unique daughter sites. The key order parameters that define a structural transition have zero amplitude within the HS structure, and take non-zero amplitudes on the LS structure. A parameter in the LS phase r^{LS} can be calculated from its value in the HS phase r^{HS} plus the static contribution of all associated symmetry modes (Perez-Mato *et al.*, 2010):

$$r^{LS} = r^{HS} + \sum_m c_m Q_m \varepsilon_m. \tag{3.1}$$

The m index runs over all of the modes associated with the parent atom, ε_m is the component of the unnormalized polarization vector ε of the mth mode associated with the respective atom and c_m is a normalisation coefficient. Q_m is the amplitude of the mth mode, and equals the root-summed-squared displacement, summed over all supercell atoms affected by the mode (Müller *et al.*, 2011). So each symmetry mode is composed of an amplitude and a unit vector, which indicates the direction.

Within a phase transition, typically only a fraction of all possible symmetry modes is active. This reduction in the number of active parameters can simplify a structure solution and stabilise a difficult structure refinement (Campbell *et al.*, 2007).

In the present thesis symmetry modes were applied for investigation of several phase transitions. In all cases, the decomposition of the crystal structure in terms of symmetry modes was performed using ISODISTORT (Campbell *et al.*, 2006). For decomposition, crystallographic information files (CIFs) of a real or hypothetical HS parent structure and the LS structure were used. ISODISTORT uses group-theoretical methods to compute the symmetry-mode polarization vectors and normalization coefficients (Campbell *et al*., 2006).

For Rietveld refinement a code which relates symmetry modes and structural parameters was obtained from the program. This allows direct refinement of symmetry mode amplitudes within Rietveld refinement using TOPAS (Bruker AXS, 2009).

3.1.2   Rigid bodies and rigid body symmetry modes

Many crystal structures contain groups of atoms with a specific and fixed arrangement, e.g. benzene rings. During refinement, it can be beneficial to treat these atoms as a rigid unit with fixed or constrained arrangement, which is done by describing them as a rigid body (RB). This offers several advantages, since the RB is shifted as a whole unit, avoiding meaningless changes of individual atoms. The number of refined parameters is reduced and the remaining parameters can be refined with higher accuracy. Even hydrogen atoms can be included into the RB if their positions in relation to neighbouring atoms are known (riding model) (Dinnebier, 1999).

In order to position a RB within a crystal structure in general six external parameters need to be defined. The position of the center of the RB is given by three translational parameters, while the orientation is defined by three rotation angles. Those parameters can be reduced if atoms are situated on special positions (Dinnebier, 1999).

There are different ways for the setup of rigid bodies. Within TOPAS (Bruker AXS, 2009) two different approaches can be pursued. The simplest way is to use a fractional Cartesian coordinate system, placing the atoms on distinct positions. In TOPAS (Bruker AXS, 2009) this is done by an operation, which is called "point for site". The other possibility is to use a z-matrix. A z-matrix defines a RB in terms of the internal parameters namely bond lengths, angles and torsion angles (Leach, 2001). In order to generate the z-matrix one starts with one atom or pseudo atom, which is placed in the origin of the internal rigid body coordination system. It is advantageous to use the centre of gravity as origin of the RB, even if no atom is present, to allow for uniform rotations. Based on the center of the RB, all atoms are placed using interatomic distances, angles and torsion angles. In the first column of a z-matrix, starting with the second atom, the distance to a previously defined atom is given, in the second column, starting from the third atom, an angle between the atoms and in the third column, starting with the fourth atom, a torsion angle with respect to previous defined cites is given (Leach, 2001). A comparison of the two possible descriptions of a RB for a tetrahedron is given in Table 3.1 (Dinnebier & Müller, 2012).
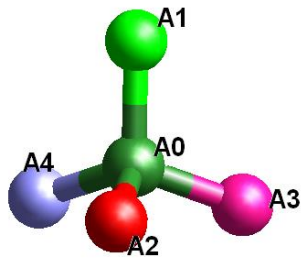
During a phase transition the orientation and position of a RB within a crystal structure might change. In order to follow such changes the up to six position and orientation parameters of the RB need to be followed within refinement of a series of *in-situ* powder diffraction data. This can be performed for simple structures, though, for more complex ones, a different approach reducing the number of parameters even further can be beneficial. Furthermore the interatomic distances and angles within the RB might change so that they need to be analysed as well.

In order to facilitate and enhance the analysis of rigid body rotations during a phase transition, a symmetry adapted parameter set was developed. The new parameter set, which is denoted as rigid body symmetry modes, combines features of rigid bodies and symmetry modes. In this method, the orientation and position of a RB is given by a rotational vector. In general, both, rotational and displacive vectors can be used to describe a crystal structure, though the intrinsic tensor properties are different. An atomic displacement is described by a polar vector, while a rotation vector is an axial

one, which leads to different behaviour with respect to symmetry elements. However it can be shown that intrinsic and extended rigid body rotations can be described within traditional crystallographic space groups (Müller *et al.*, 2013).

Table 3.1: Comparison of different RB descriptions of a tetrahedron composed of five atoms using a) z-matrix notation and b) Cartesian coordinates. The distance between two neighbouring atoms is *r*. The angle of 109.47° is the typical tetrahedron angle.

a)

atom	distance	angle	torsion angle	related atoms
A0				
A1	r			A0
A2	r	109.47		A2 A1
A3	r	109.47	120	A0 A2 A1
A4	r	109.47	240	A0 A3 A2

b)

atom	x	y	z
A0	0	0	0
A1	$r\sin\left(\dfrac{109.47}{2}\right)$	$r\cos\left(\dfrac{109.47}{2}\right)$	0
A2	$-r\sin\left(\dfrac{109.47}{2}\right)$	$r\cos\left(\dfrac{109.47}{2}\right)$	0
A3	0	$-r\cos\left(\dfrac{109.47}{2}\right)$	$r\sin\left(\dfrac{109.47}{2}\right)$
A4	0	$-r\cos\left(\dfrac{109.47}{2}\right)$	$-r\sin\left(\dfrac{109.47}{2}\right)$

3.1.3   The theory of phase transitions (Landau theory)

A phase transition within a material is characterized by a discontinuous change of at least one material property (e.g. density, elasticity, magnetic and electric properties or crystal structure). Throughout the work of this thesis, different structural phase transitions with different mechanisms were studied.

The type of structural change can be used to distinguish structural phase transition into different classes. During a reconstructive phase transition, atomic bonds are broken and/or build. The crystal structure can change completely; therefore this process cannot be continuous. A contrast to such transitions is the displacive transition. During a displacive phase transition, atomic positions change continuously. A third type of transitions is the order-disorder transition, which is characterized by a change in atomic positions between an ordered arrangement and a less ordered arrangement.

In another classification all phase transitions, which are accompanied by a change in the point group symmetry are called ferroic. A ferroic distortion can be further classified as ferroelastic if it changes the shape of the unit cell in such a way as to alter the crystal system (Wadhawan, 1982).

In 1933, Ehrenfest (Ehrenfest, 1933) developed a classification of phase transitions which is based on the thermodynamic free energy G (also known as Gibbs energy). Transitions which are characterized by a jump of the first derivative of the thermodynamic free energy G are called first-order. In case of second-order transitions, volume and entropy change continuously, though the second derivative of the Gibbs free energy G exhibits a jump (Müller, 2012). Nowadays, phase transitions are distinguished in discontinuous and continuous transitions, whereupon still the phrase "first-order transition" is used for discontinuous transitions and "second-order transition" for continuous transitions. In case of a discontinuous or hysteretic transition, the order parameter and the entropy jump at the transition point, while in case of a continuous transition, they change smoothly, requiring that another thermodynamic function is discontinuous (Müller, 2012).

In order to describe phase transitions, Landau developed a phenomenological theory (Landau, 1937). Based on the precondition that there is a group-subgroup relation between the HS and LS structure, a thermodynamic variable needs to exist in order to describe the thermodynamic state of the LS phase (Salje, 1990). Therefore a new variable was introduced: the order parameter Q. The energy difference of the Gibbs energy, which stabilises the LS phase, is thus dependent on the usual parameters (temperature T, pressure p and chemical composition N) and the order parameter Q.

The order parameter decreases continuously to zero at a second-order phase transition, whereas an order parameter can abruptly "jump" at a first-order transition. In case of a temperature dependent phase transition, the order parameter Q can be modelled by an empirical power law of the form:

$$Q = f|T_{crit} - T|^{\beta} \tag{3.2}$$

where T_{crit} is the transition temperature, β[6] is the critical exponent, and f is a prefactor. Typical values of β are ½ for ordinary scalar second-order transitions, or ¼ for a transition at the tricritical point that marks the boundary between first- and second-order transitions. Values between ¼ and ½ might be obtained for a variety of reasons (Salje, 1990; Cowley, 1980).

The Landau critical exponent is derived by calculating the first derivative of the Taylor series expansion of a truncated Gibbs energy with respect to the order parameter and setting it to zero (Landau, 1937; Müller, 2012):

$$\frac{\partial G}{\partial Q} = 0. \tag{3.3}$$

This approach is correct for small values of Q (close to T_{crit}), though it has proven to be applicable in a larger range. A truncation of the Taylor series is possible, if the last term has a positive prefactor, which guarantees that an increase in Q leads to an increase in G (Müller, 2012).

Within the Taylor series of G (also known as Landau potential) only even power terms are allowed as G must be positive, independent from the sign of Q, in case of a continuous phase transition (Müller, 2012):

$$G = G_0 + \frac{1}{2}AQ^2 + \frac{1}{4}BQ^4 + \frac{1}{6}CQ^6. \tag{3.4}$$

---

[6] β is used for both, the crystallographic angle β and the critical exponent β. Therefore each time β is mentioned its meaning will be given.

For temperatures above T_{crit} a minimum is given for the trivial solution $Q = 0$. Below T_{crit} a minimum will be present at $Q \neq 0$, so the dependence of the prefactors A, B and C on temperature must be evaluated. The factor A is the most important one, it need to be zero at the transition temperature T_{crit}, above T_{crit} it must be positive, and below negative. The simplest solution, which fulfils the above requirements, is a linear dependency:

$$A = k(T - T_{crit}) \qquad \text{with} \quad k > 0. \tag{3.5}$$

Assuming B to be $B > 0$, C can be set to zero as its influence in this case is negligible. Under these conditions, the Landau potential is reduced to its 2nd and 4th order terms, which is called 2-4 potential (Salje, 1990; Müller 2012):

$$G = G_0 + \frac{1}{2} AQ^2 + \frac{1}{4} BQ^4. \tag{3.6}$$

Taking the derivative leads to:

$$\frac{\partial G}{\partial Q} = AQ + BQ^3 = 0 \tag{3.7}$$

and $\quad Q(A + BQ^2) = 0$. $\tag{3.8}$

The trivial solution is $Q = 0$ for $T > T_{crit}$. Otherwise the solution is:

$$-\frac{A}{B} = Q^2. \tag{3.9}$$

Using equation (3.5) for A, the following result for $T < T_{crit}$ will be obtained:

$$Q = \sqrt{-\frac{k}{B}} (T - T_{crit})^{\frac{1}{2}} \text{ or more general } Q = f(T - T_{crit})^{\frac{1}{2}}, \tag{3.10}$$

which proves that the critical exponent $\beta = \frac{1}{2}$ for a second-order phase transition (Müller, 2012).

In a similar way it can be shown that in case of a tricritical (also called "weakly" first-order) transition a value of ¼ is obtained (Salje, 1990). In this case the same behaviour of A is assumed, though B is assumed to be not positive, and therefore is set to zero. This requires using the 6th order term with $C > 0$. The resulting potential is denoted as 2-6 potential (Salje, 1990; Müller, 2012):

$$G = G_0 + \frac{1}{2} AQ^2 + \frac{1}{6} CQ^6 . \tag{3.11}$$

As for the previous case, the derivative needs to be taken and the following equations are obtained:

$$\frac{\partial G}{\partial Q} = AQ + CQ^5 = 0 \tag{3.12}$$

$$Q(A + CQ^4) = 0 . \tag{3.13}$$

Using equation (3.5) for A, solutions of equation (3.13) are:

$Q = 0$ for $T > T_{crit}$ and

$$Q = \sqrt[4]{-\frac{k}{C}} (T - T_{crit})^{\frac{1}{4}} \text{ or more general } Q = f(T - T_{crit})^{\frac{1}{4}}. \tag{3.14}$$

So for a tricritical phase transition the critical exponent β is equal to ¼.

It has also been shown that non-standard critical exponents β obtained from fits over extended temperature ranges are often due to temperature-dependent energy-expansion coefficients of order four or higher and have nothing at all to do with critical phenomena (Giddy et al., 1989; Radescu et al., 1995).

As Landau theory can describe ferroic phase transitions, an equation based on equation (3.2) was used in sequential and parametric Rietveld refinements in order to model the behaviour of parameters in dependence on an external variable. Amplitudes, given by the prefactor f, and critical exponents β were refined.

3.2 The first-order phase transition of $CsFeO_2$

The work presented in this chapter was published in: Melanie Müller, Robert E. Dinnebier, Naveed Z. Ali, Branton Campbell and Martin Jansen: *Direct Access to the Order Parameter: Parameterized Symmetry Modes and Rigid Body Movements as a Function of Temperature*. Materials Science Forum (Extending the Reach of Powder Diffraction Modelling) (2010) 651, 79-95.

Sample synthesis was performed by Naveed Zafar Ali (formerly Max Planck Institute for Solid State Research). The synchrotron measurements were performed by Denis Sheptyakov from Laboratory for Neutron Scattering, ETH Zürich (Switzerland) and PSI Villigen (Switzerland).

3.2.1 Introduction

The first-order phase transition of $CsFeO_2$ was investigated using *in-situ* synchrotron powder diffraction data measured in dependence on temperature. Two alternative approaches were used to describe the deviation of the framework crystal structure relative to the high symmetry parent structure: symmetry modes (SM) and rigid body (RB) parameters. In both cases, the relevant parameters were refined as a function of temperature using the method of parametric Rietveld refinement (Müller *et al.*, 2010).

3.2.1.1 The compound $CsFeO_2$

$CsFeO_2$ belongs to the group of alkali metal oxoferrats(III) with composition $AFeO_2$. Those compounds as well as other oxoferrates(III) of light alkali metals are structurally closely related to the group of oxosilicates due to the predominance of tetrahedral coordination of Fe(III) (Frisch & Röhr, 2005). Most of the alkali metal oxoferrats(III) crystallise in structures which can be derived from a stuffed β-cristobalite structure, so they are members of the structure family of feldspars (Nuss *et al.*, 2007).

At ambient conditions, $CsFeO_2$ crystallises in the orthorhombic space group *Pbca*. At about 80°C, it undergoes a first-order phase transition to the cubic space group $Fd\bar{3}m$ (Ali *et al.*, 2010). The LS crystal structure is shown in Figure 3.1. Within the HS cubic structure the Fe-O tetrahedra are arranged in a more ordered way. The difference between the arrangements can be seen in Figure 3.2.
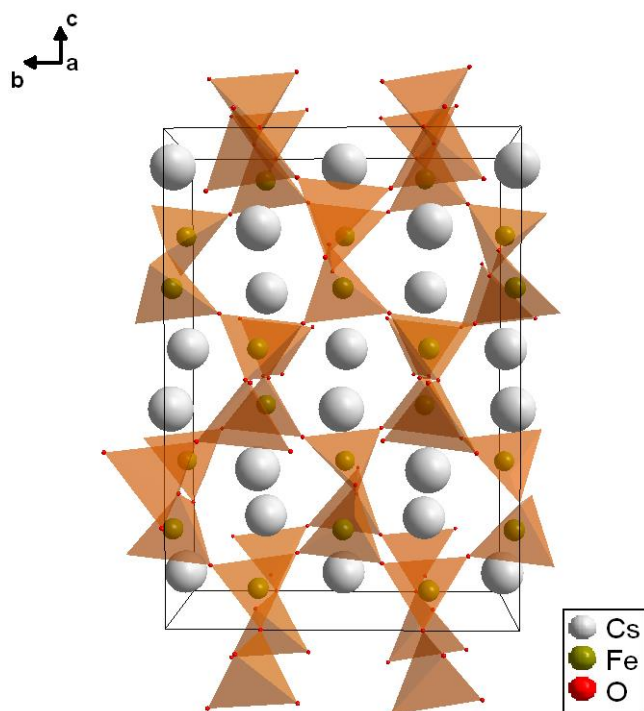
Figure 3.1: An *a*-axis projection of the low-temperature (*Pbca*) crystal structure of $CsFeO_2$ at ambient conditions.
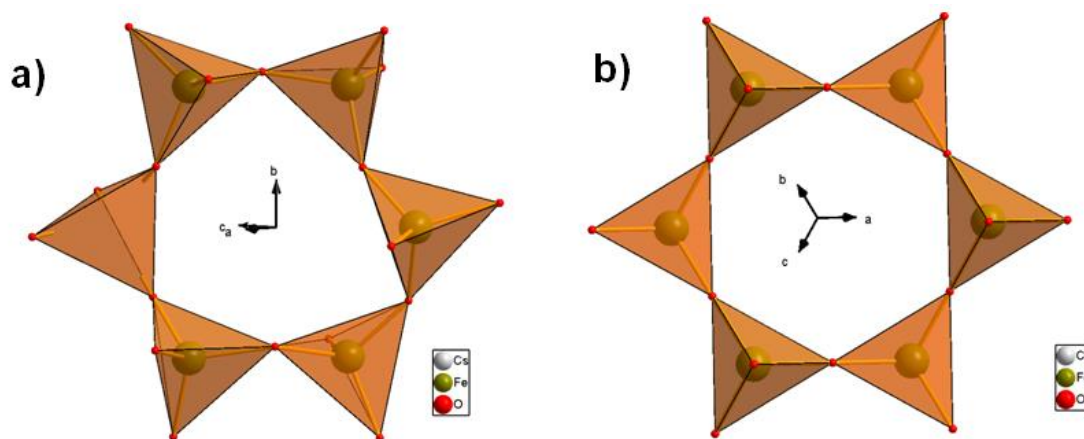
Figure 3.2: Arrangement of six connected Fe-O tetrahedra within the low symmetry orthorhombic (a) and high symmetry cubic (b) structures of $CsFeO_2$. Within the LS structure the tetrahedra are twisted with respect to each other.

3.2.2   Experimental

3.2.2.1   Material synthesis

Sample preparation was performed following the azide/nitrate route (Trinschek & Jansen, 1999; Sofin *et al.*, 2002) using cesium nitrate ($CsNO_3$), cesium azide (CsN_3) and active iron oxide (Fe_2O_3) according to the following equation:

$$5\,CsN_3 + CsNO_3 + 3Fe_2O_3 \rightarrow 6\,CsFeO_2 + 8\,N_2\,. \tag{3.15}$$
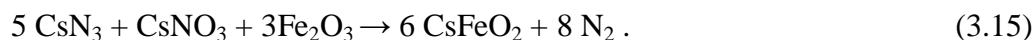
The preparation process was described by Ali *et al.* (2010). After grinding the appropriate amount of the starting materials (see equation (3.15)), the obtained powder was pressed into pellets under nitrogen pressure. These pellets were dried in vacuum at 127°C and given into a steel vessel with silver inlet under argon atmosphere. Following a suitable temperature profile (Ali *et al*., 2010), a powdered sample was obtained, which is sensitive to humidity and thus must be handled in inert atmosphere.

3.2.2.2   Measurement

For temperature dependent *in-situ* powder diffraction measurements, the material was sealed into a Hilgenberg quartz-glass capillary with a diameter of 0.3 mm. Measurements were performed at the Materials Sciences (MS-Powder) beamline of the Swiss Light Source using synchrotron radiation at a wavelength of 0.49701 Å. The powder sample was heated from 30 – 136°C with steps of 1K using a STOE capillary furnace. The diffraction patterns were collected using a Microstrip Mythen-II detector with an acquisition time of 40 seconds for each pattern (4 scans of 10 seconds each) in the angular range from 3.0° – 53.38° 2θ.

3.2.3   Method and Results

Two different models were used for structural description during the phase transition from orthorhombic to cubic $CsFeO_2$. The first approach, which was applied, is the symmetry mode approach, which will be denoted as SM. In order to obtain the required information to do the symmetry mode Rietveld refinements, CIFs of the HS $Fd\bar{3}m$ and LS *Pbca* phases were subjected to the ISODISTORT software to perform an automatic symmetry mode decomposition of the low symmetry distorted structure into modes of the high symmetry cubic parent.

The cubic phase contains in total 32 atoms in the conventional face-centred unit cell, which do not have any general atomic coordinates, so all atoms are placed on special Wyckoff positions. In the orthorhombic phase, however, there are 24 free atomic coordinates. Because the symmetry mode basis is related to the traditional atomic coordinate basis by a linear transformation, there must also be 24 displacive symmetry modes (Müller *et al.*, 2010). A list of all modes is given in Table 3.2. Table 3.2 contains number, name and description of each symmetry mode. Within the mode name the parent space group symmetry, the k-point (the point in reciprocal space that will get intensity if the mode is activated), the space group irrep label and order parameter direction (dictates which space group symmetry operations are preserved by the mode), the parent atom affected by the mode and its Wyckoff site, the irrep of

the point-group symmetry (dictates which site symmetry operations are preserved by the mode) and the order parameter branch are given (Campbell *et al.*, 2006). Furthermore these results are saved in form of a set of linear equations, which can be used in Rietveld refinement.

In order to describe the phase transition the mode amplitudes of ten out of the 24 displacive symmetry modes need to be refined, while the others are set to zero. The following modes were used in refinement (see Table 3.2): two (a_2 and a_4) for caesium, two (a_9 and a_{10}) for iron and six (a_{14}, a_{15}, a_{16}, a_{17}, a_{18} and a_{19}) for oxygen. The a_2-mode affects the *y*-coordinates of both caesium atoms, while a_4 only affects the *x*-coordinate of Cs2. The a_9 mode influences the *y*-coordinate of the Fe1 and Fe2 atoms, while the a_{10} mode influences only the *x*-coordinate of the Fe1 atom. The combination of the oxygen modes a_{14} to a_{19} describes the rotation of the FeO_4 tetrahedron, which should not be substantially distorted (Müller *et al.*, 2010).

Furthermore the crystal structure of $CsFeO_2$ was described using rigid bodies. In order to do so, a RB which can describe the LS and HS crystal structure was developed. It is built of two corner sharing FeO_4 tetrahedra, which can be tilted with respect to each other. The RB consists of two iron and four oxygen atoms, the other atoms, needed to complete the tetrahedra, are generated by space group symmetry (Müller *et al.*, 2010). Within the RB, there are three internal degrees of freedom: two tilting angles and the average interatomic distance *r*. The two tilt angles are (1) the Fe1-O1-Fe2 (*tilt-1*) bond angle and (2) the O4-Fe2-O1-Fe1 torsion angle (*tilt-2*) between the two tetrahedra. The RB and the corresponding tilt angles are shown in Figure 3.3. The z-matrix description of the RB is given in Table 3.3.

Table 3.2: Symmetry-adapted distortion modes available to the ferroelastic phase transition of CsFeO2 from $Fd\bar{3}m$ to *Pbca* symmetry. The ten modes that were actually used for Rietveld refinements appear in bold.

	name	description of mode
1	a1	Fd-3m[0,0,0]GM5+(a,0,0)[Cs:b]T2
2	**a2**	**Fd-3m[0,3/2,0]DT5(0,0,0,0,0,0,0,0,a,-2.414a,2.414a,a)[Cs:b]T2_1(a)**
3	a3	Fd-3m[0,3/2,0]DT5(0,0,0,0,0,0,0,0,a,-2.414a,2.414a,a)[Cs:b]T2_2(a)
4	**a4**	**Fd-3m[1/2,1/2,0]SM2(0,a,0,0,0,0,0,0,0,0,0,0)[Cs:b]T2(a)**
5	a5	Fd-3m[1/2,1/2,1/2]L3+(0,0,0,0,a,-a,-a,a)[Cs:b]T2(a)
6	a6	Fd-3m[0,1,0]X1(0,a,0,0,0,0)[Cs:b]T2(a)
7	a7	Fd-3m[0,0,0]GM5+(a,0,0)[Fe:a]T2(a)
8	a8	Fd-3m[0,3/2,0]DT5(0,0,0,0,0,0,0,0,a,-2.414a,2.414a,a)[Fe:a]T2_1(a)
9	**a9**	**Fd-3m[0,3/2,0]DT5(0,0,0,0,0,0,0,0,a,-2.414a,2.414a,a)[Fe:a]T2_2(a)**
10	**a10**	**Fd-3m[1/2,1/2,0]SM2(0,a,0,0,0,0,0,0,0,0,0,0)[Fe:a]T2(a)**
11	a11	Fd-3m[1/2,1/2,1/2]L3+(0,0,0,0,a,-a,-a,a)[Fe:a]T2(a)
12	a12	Fd-3m[0,1,0]X1(0,a,0,0,0,0)[Fe:a]T2(a)
13	a13	Fd-3m[0,3/2,0]DT5(0,0,0,0,0,0,0,0,a,-2.414a,2.414a,a)[O:c]A2u(a)
14	**a14**	**Fd-3m[0,3/2,0]DT5(0,0,0,0,0,0,0,0,a,-2.414a,2.414a,a)[O:c]Eu_1(a)**
15	**a15**	**Fd-3m[0,3/2,0]DT5(0,0,0,0,0,0,0,0,a,-2.414a,2.414a,a)[O:c]Eu_2(a)**
16	**a16**	**Fd-3m[1/2,1/2,0]SM2(0,a,0,0,0,0,0,0,0,0,0,0)[O:c]A2u(a)**
17	**a17**	**Fd-3m[1/2,1/2,0]SM2(0,a,0,0,0,0,0,0,0,0,0,0)[O:c]Eu_1(a)**
18	**a18**	**Fd-3m[1/2,1/2,0]SM2(0,a,0,0,0,0,0,0,0,0,0,0)[O:c]Eu_2(a)**
19	**a19**	**Fd-3m[1/2,1/2,1/2]L2+(0,0,a,-a)[O:c]Eu(a)**
20	a20	Fd-3m[1/2,1/2,1/2]L3+(0,0,0,0,a,-a,-a,a)[O:c]A2u(a)
21	a21	Fd-3m[1/2,1/2,1/2]L3+(0,0,0,0,a,-a,-a,a)[O:c]Eu_1(a)
22	a22	Fd-3m[1/2,1/2,1/2]L3+(0,0,0,0,a,-a,-a,a)[O:c]Eu_2(a)
23	a23	Fd-3m[0,1,0]X1(0,a,0,0,0,0)[O:c]A2u(a)
24	a24	Fd-3m[0,1,0]X1(0,a,0,0,0,0)[O:c]Eu(a)
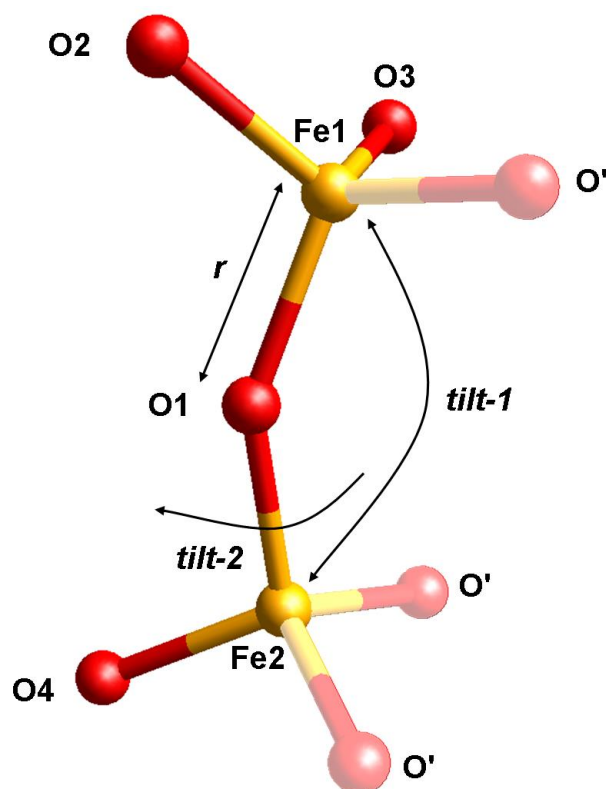
Figure 3.3: Rigid body consisting of the Fe-O double tetrahedron in $CsFeO_2$ exhibiting three internal parameters: *r*, *tilt-1* and *tilt-2*. Solid atoms are implemented into the program; semitransparent atoms are generated due to space group symmetry.

Table 3.3: Z-matrix description of the crystallographically independent atoms of the Fe_2O_7 rigid body. The three internal refinable parameters (*tilt-1*, *tilt-2* and *r*) are displayed in bold.

atom	distance	angle	torsion angle	related atoms
O1				
Fe1	*r*			O1
O2	*r*	109.47		Fe1 O1
O3	*r*	109.47	120	Fe1 O2 O1
Fe2	*r*	*tilt-1*	180	O1 Fe1 O2
O4	*r*	109.47	*tilt-2*	Fe2 O1 O2

For Rietveld refinement, the orientation and position of the RB relative to the internal coordinate system of the crystal were kept constant over the entire temperature range of investigation and only the three internal degrees of freedom were subjected to refinement. As the two caesium atoms in the voids of the framework are independent of the RB, their crystallographically relevant atomic coordinates were refined separately (Müller *et al.*, 2010).

The behaviour of the lattice parameters in dependence on temperature was described using lattice strain. Strain is a symmetric second rank tensor which is represented by a 3×3 matrix. In case of orthorhombic symmetry (actual supercell) it reduces to a diagonal matrix with the following diagonal elements:

$$e_{11s} = \frac{a_s}{a_{s0}} - 1 = \frac{a_s}{a_{P0}/\sqrt{2}} - 1 \qquad\qquad (3.16)$$

$$e_{22s} = \frac{b_s}{b_{s0}} - 1 = \frac{b_s}{\sqrt{2}a_{P0}} - 1 \qquad\qquad (3.17)$$

$$e_{33s} = \frac{c_s}{c_{s0}} - 1 = \frac{c_s}{2a_{P0}} - 1 \qquad\qquad (3.18)$$

with the lattice parameters of the supercell a_s, b_s, c_s and the isothermal lattice parameters a_{s0}, b_{s0} and c_{s0}. The isothermal lattice parameters can be given as well in dependence on the isothermal lattice parameters of the cubic parent cell a_{p0}.

The same description can be used in dependence on the cubic parent cell. In this case, strain is represented by a diagonal matrix with $e_{11p} = e_{22p} = e_{33p}$ and $e_{12p} = e_{23p} = e_{13p} = 0$ (Müller *et al.*, 2010).

Upon formation of the ferroelastic strain, the parent cell becomes a pseudo-cubic monoclinic cell defined by three independent order parameters that we will denote by ε_Γ, where Γ indicates one of three strain mode irreps: Γ_1^+, Γ_3^+ and Γ_5^+. The Γ_1^+ mode causes a thermal expansion. The Γ_3^+ mode affects the ratio of the lattice parameters a and b with respect to the lattice parameter c. And the Γ_5^+ mode results in a monoclinic shear that changes the parent lattice angle γ and gives rise to a non-zero e_{12} strain component.

In the coordinate system of the parent cell, the relationships between the lattice strains, the strain order parameters, the pseudo-cubic cell parameters (a_p, b_p, c_p, γ_p) and the unstrained cubic cell parameter, a_{p0}, can be summed up as

$$e_{11p} = e_{22p} = \varepsilon_{\Gamma_1^+} - \frac{1}{2}\varepsilon_{\Gamma_3^+} = \frac{a_p}{a_{p0}} - 1 = \frac{b_p}{a_{p0}} - 1 \tag{3.19}$$

$$e_{33p} = \varepsilon_{\Gamma_1^+} + \varepsilon_{\Gamma_3^+} = \frac{c_p}{a_{p0}} - 1 \tag{3.20}$$

$$e_{12p} = e_{21p} = \frac{1}{2}\varepsilon_{\Gamma_5^+} = \frac{\pi}{2} - \gamma_p. \tag{3.21}$$

Those two different descriptions of the supercell and the cubic strain can be related to each other by the following equations:

$$e_{11s} = e_{11p} + e_{12p} \tag{3.22}$$

$$e_{22s} = e_{11p} - e_{12p} \tag{3.23}$$

$$e_{33s} = e_{33p}. \tag{3.24}$$

Rietveld refinements were performed throughout the whole temperature range using both models for structural description. This step is necessary in order to investigate the temperature dependence of the symmetry modes or the parameters of the RB. The observed behaviour is then modelled within parametric Rietveld refinement using a conditional statement for all order parameters in the LS phase, and setting them to zero in the HS phase (Müller *et al.*, 2010) using the following pseudo code:

$$\text{If } (\text{T} < T_{crit}) \text{ then } Q(T) = f(T_{crit} - T)^\beta, \text{ else } Q = 0. \tag{3.25}$$

In the rigid body parameter refinement each parameter of the z-matrix has its own refinable coefficient and exponent. Using symmetry modes however, all modes belonging to a single order parameter share the same critical exponent. Furthermore the supercell strain parameters were modeled as power law trends versus temperature. They are viewed as independent coupled order parameters as they cooperate to model

the behaviour of lattice parameters, though each possesses its own power law exponent and coefficient (Müller *et al.*, 2010).

The temperature-independent power law exponents and coefficients were then subjected to parametric refinement, simultaneously against diffraction patterns collected at all temperatures. During parametric refinement the exponents and coefficients of the strain parameters were used to calculate the supercell lattice parameters at each temperature. In order to compensate thermal expansion, a linear extrapolation of the cubic parent cell parameter $a_0(T)$ in dependence on temperature within the low symmetry phase was implemented. The slope (m_0) and the intercept (t_0) of the extrapolation were also part of the parametric refinement. The background was modelled using a Chebyshev polynomial of 8th order in combination with two extra peaks which are used to describe the contribution of the glass capillary. TOPAS (Bruker AXS, 2009) was used to perform the refinements.

The resulting refinement at a single temperature ($T = 55°C$) using symmetry modes is shown in Figure 3.4. The parametric symmetry mode refinement can be seen in Figure 3.5. In this case for all plots from 30°C to 136°C observed, calculated and difference traces are shown in a stacked arrangement.
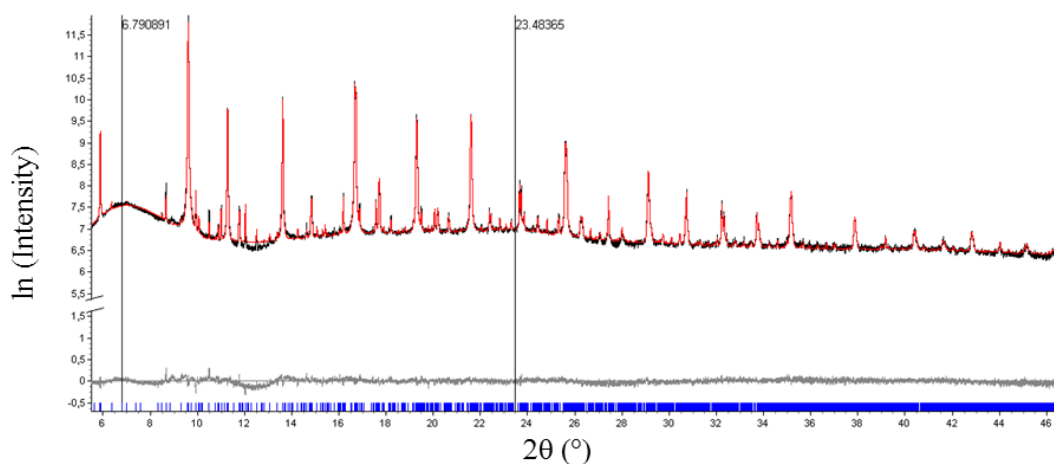
Figure 3.4: Logarithmic plot of the single-point symmetry-mode refinement of $CsFeO_2$ at $T = 55°C$.
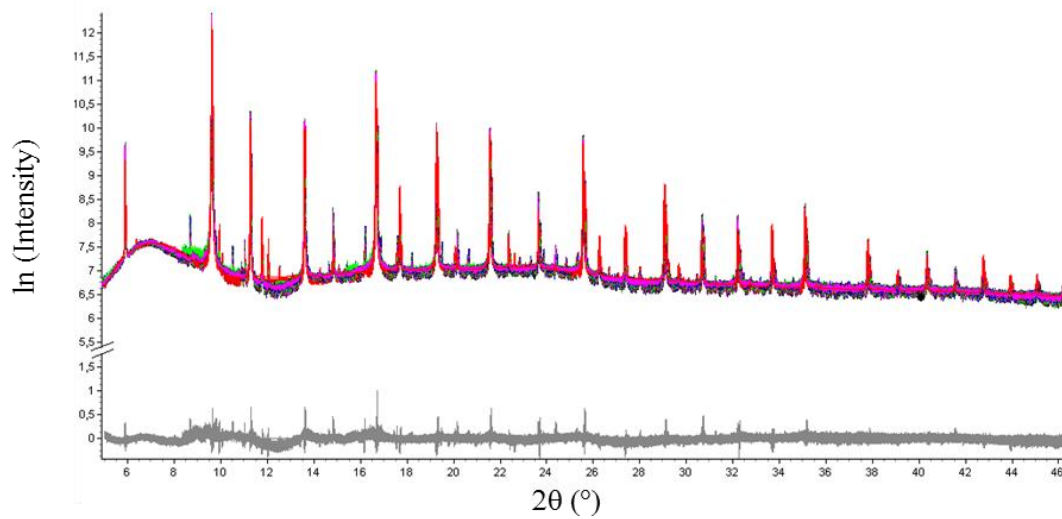
Figure 3.5: Logarithmic plot of the temperature-dependent parametric symmetry-mode refinement of $CsFeO_2$ in the temperature range from 30°C to 136°C. Observed, calculated and difference traces for all temperatures used (1K steps) are shown in a stacked arrangement.

From Figure 3.5, it can be seen that the calculated diffraction patterns are in good agreement with the measured ones, so it can be concluded that the model chosen for refinement is appropriate. For both parametric refinements (using symmetry modes and using rigid bodies) comparable lattice parameter were obtained (Figure 3.6) and the strain values show the same temperature dependence (Figure 3.7). The strain amplitude e_{11} is much larger that the two other e_{22} and e_{33} (Müller *et al.*, 2010).
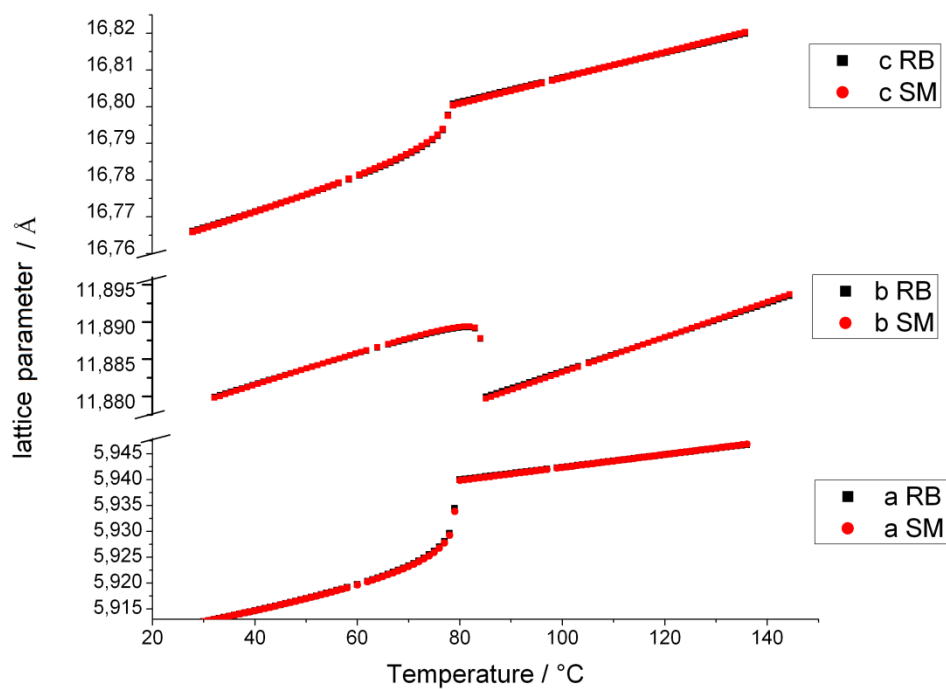
Figure 3.6: Temperature-dependent supercell parameters for $CsFeO_2$ as calculated from parametrically refined power law models of the strain parameters.
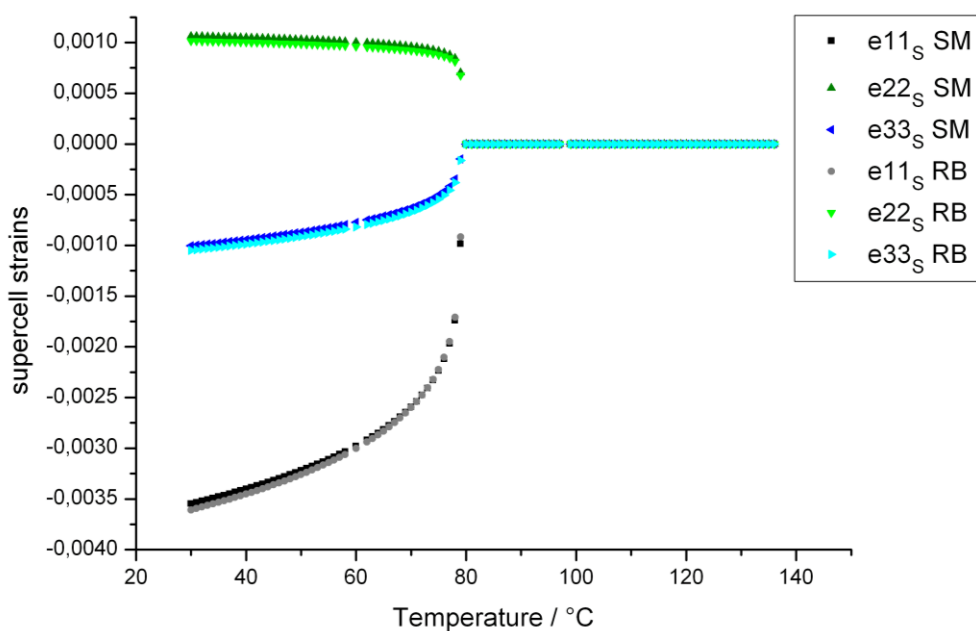
Figure 3.7: Temperature-dependent supercell strains for $CsFeO_2$ as calculated from their parametrically refined power law models.

Within the two approaches the atomic positions were derived using a completely different basis. The SM description is much less restrictive than the RB description, so there are more parameters within the refinement. The temperature dependencies of the displacive degrees of freedom are plotted in Figure 3.8. These curves were obtained in parametric Rietveld refinement. The refined power law coefficients and exponents are listed in Table 3.4. Within the symmetry mode model, for modes associated with a single order parameter, the critical exponent was assumed to be identical. The key parameters which describe the phase transition are DT5 (Δ_5), SM2 (Σ_2) and L2+ (L_2^+). ISODISTORT was used to determine that any two of these could comprise a potentially primary (i.e. capable of producing the symmetry of the distorted phase) pair of coupled order parameters.
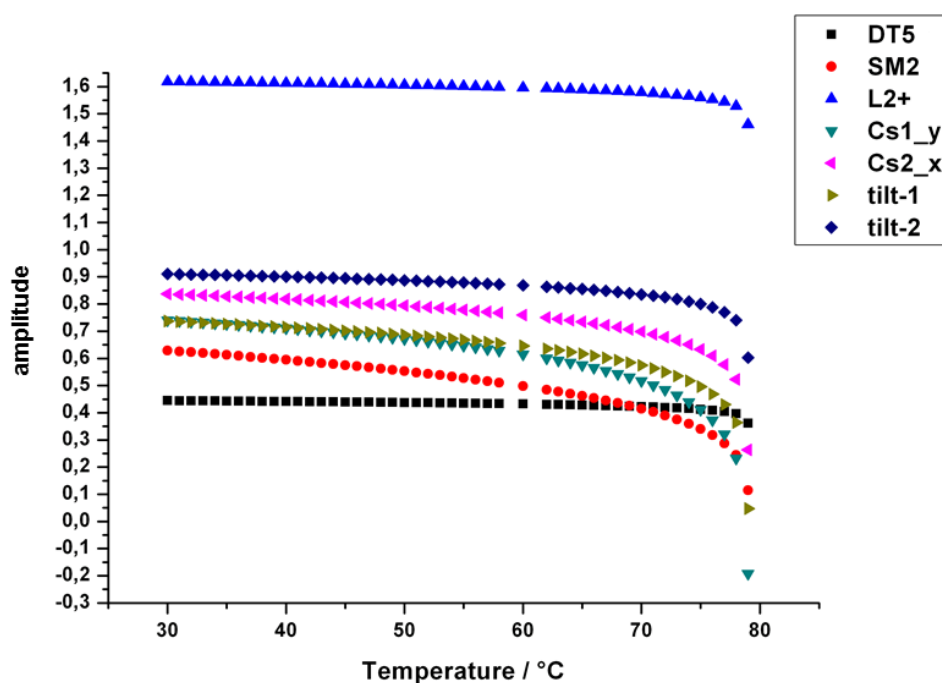
Figure 3.8: Comparison of the root squared sum of the DT5, SM2 and L2+ modes with the normalised internal RB parameters in dependence on temperature.

Within the symmetry mode refinement the DT5, SM2 and L2+ order parameters have influence on atoms within the FeO_4 tetrahedra. In order to preserve the shapes of the

FeO_4 tetrahedra, it can be assumed that they are strongly coupled by physical bonding constraints. E.g. the a_{15} and a_{19} symmetry modes, for example, must cooperate to mimic the RB *tilt-2* angle, and therefore are coupled with the same power law exponents. Because the SM and RB models are roughly equivalent, it is not surprising that the DT5/L2+ power law exponent is similar to that of the RB *tilt-2* angle. Other relationships between the two models include the a_{10} symmetry mode, which approximates the RB *tilt-1* angle, and the a_2 and a_4 symmetry modes which are related to the unconstrained Cs positions of the RB model. In each of these cases, the power law exponents of geometrically related SM and RB parameters are within three standard deviations of one another (Müller *et al.*, 2010).

As expected for a first-order phase transition small values are obtained for the critical exponents (see Table 3.4). This is also evidenced within ISODISTORT, which determined that none of the DT5, SM2 or L2+ order parameters of the $CsFeO_2$ distortion are capable of producing continuous transitions when acting alone, and certainly not when acting simultaneously.

Table 3.4: Comparison of effective power law coefficients and exponents obtained from parametric Rietveld refinement of $CsFeO_2$ in dependence on temperature using symmetry modes and rigid body parameters.

symmetry mode	f	β	rigid body	f	β
a2(Δ_5)	0.066(1)	0.015(1)	Cs1y		0.26(1)
a4(Σ_2)	0.355(1)	0.123(2)	Cs2x		0.11(1)
a9(Δ_5)	0.145(3)	0.015(1)	tilt-1		0.168(2)
a10(Σ_2)	0.241(1)	0.123(2)	tilt-2		0.056(1)
a14(Δ_5)	0.622(12)	0.015(1)			
a15(Δ_5)	0.616(13)	0.015(1)			
a16(Σ_2)	0.213(4)	0.123(2)			
a17(Σ_2)	-0.061(5)	0.123(2)			
a18(Σ_2)	-0.499(5)	0.123(2)			
a19(L_2^+)	1.528(8)	0.015(1)			
ε_{11s}	-0.00172	0.185(1)	ε_{11s}	-0.0017	0.194(1)
ε_{22s}	0.00084	0.059(1)	ε_{22s}	0.00081	0.058(1)
ε_{33s}	-0.00034	0.277(2)	ε_{33s}	-0.00038	0.262(2)

3.2.4   Conclusions

Parametric refinement of structural order parameters that arise at the cubic to orthorhombic structural phase transition of $CsFeO_2$ was performed. Within the parametric refinement two different approaches of structural description were applied. It could be shown that these methods are closely related and give an equivalent description of the phase transition. Parameters describing the displacive movements of the atoms as well as the lattice parameters showed the expected power law behaviour (Müller *et al.*, 2010).

In order to do such a refinement a sufficient number of data points need to be available, especially close to the transition temperature. This can be readily done using synchrotron radiation sources. The present phase transition is not ideally suited to be described with a Landau model, as it is a first-order transition, yet, it could be shown that the applied methods can be used in principal. Especially the identification of symmetry modes, necessary to describe a transition is considerably facilitated (Müller *et al.*, 2010).

3.3 The high-temperature phase transition of CuInSe$_2$

The work presented in this chapter was published in: Melanie Müller, Robert E. Dinnebier and Susan Schorr: *A case study of parameterized Rietveld refinement: The structural phase transition of CuInSe$_2$*. Zeitschrift für Kristallographie - Crystalline Materials (2011) 226(12), 956-962.

Sample synthesis was performed by Susan Schorr (Institute of Geological Sciences, Free University Berlin, Germany). The synchrotron measurements were performed by Susan Schorr and Guillaume Geandier (formerly European Synchrotron Radiation Facility, Grenoble, France). This phase transition was studied before (Schorr & Geandier, 2006) by sequential unconstraint Rietveld refinement without the application of a symmetry modes based decomposition of the involved structures using the same data.

3.3.1 Introduction

CuInSe$_2$ undergoes a structural phase transition from tetragonal chalcopyrite to cubic sphalerite structure type at elevated temperature. The transition has been reinvestigated in detail by sequential and parametric Rietveld refinement using *in-situ* high energy synchrotron powder diffraction data. A symmetry mode description was applied for atomic coordinates, occupancies and lattice parameters. The temperature dependence of these parameters was modeled with a phenomenological power law model according to Landau theory. This allows to directly access the temperature dependence of the order parameter leading to a more detailed understanding of the nature of the phase transition. The results of this study reveal superior statistics and much higher stability of parametric as compared to sequential Rietveld refinement (Müller *et al*., 2011).

3.3.1.1   Crystal structure and applications of CuInSe$_2$

CuInSe$_2$ belongs to the group of ternary $A^IB^{III}C^{VI}_2$ compounds. At room temperature (RT), CuInSe$_2$ crystallises in the tetragonal space group $I\bar{4}2d$. As many compounds of this type, its structure is equal to that of chalcopyrite CuFeS$_2$. Within this structure type, both types of cations are tetrahedrally coordinated by anions (Shay & Wernick, 1975). The structure can be considered as a superlattice structure of the cubic sphalerite structure and can be obtained by doubling the unit cell of ZnS in one direction (Figure 3.9). Tetragonal CuInSe$_2$ can be described by two interpenetrating face centred cubic lattices which are shifted with respect to each other by a translation vector of [¼,¼,¼]. One lattice is built by the anions, the other by the cations which are arranged in an ordered manner (Shay & Wernick, 1975).
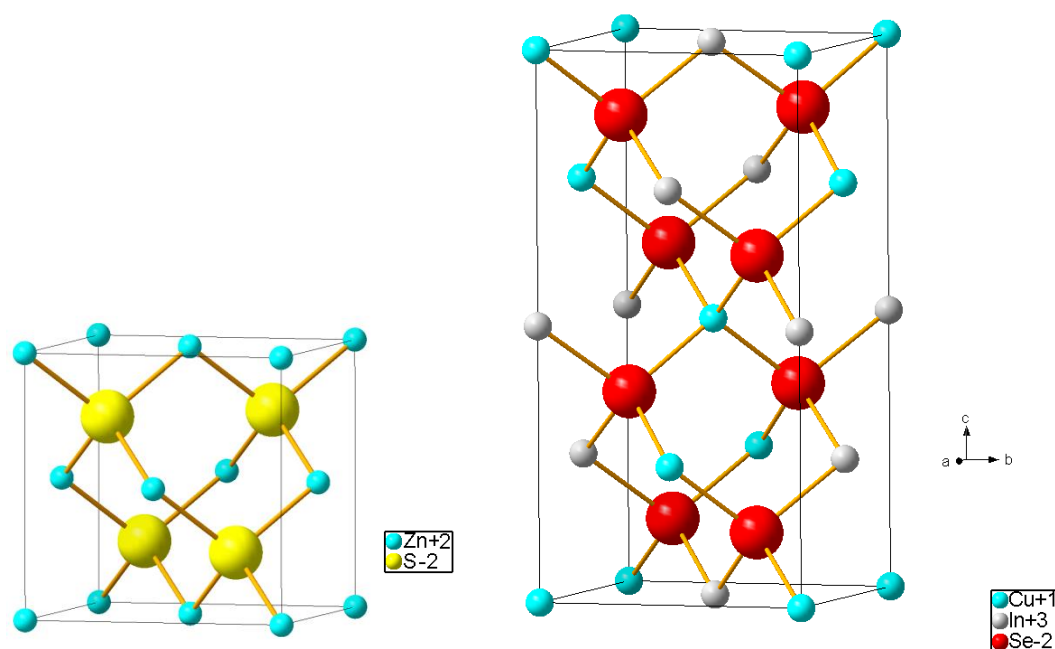
Figure 3.9: Structures of sphalerite (ZnS) (left) and CuInSe$_2$ (right). Their close structural relation is visible.

CuInSe$_2$ is commercially used as an absorber layer within thin film solar cells. CuInSe$_2$ is a semiconductor with a direct band gap of 1.04 eV (Wei & Zunger, 1995) and therefore a suitable material for photovoltaic applications. Additionally, the

compound exhibits an extremely high light absorption coefficient α of $5 \cdot 10^5$ cm^{-1} (Schorr & Geandier, 2006). Within laboratory Cu(In$_x$Ga$_{1-x}$)Se$_2$ solar cells efficiencies of about 20 % have been reached (Jackson *et al.*, 2011).

3.3.2   Experimental

CuInSe$_2$ was prepared by solid state reaction as stated in Schorr & Geandier (2006). For synchrotron measurements the obtained sample was sealed into a silica tube to prevent evaporation.

Temperature dependent *in-situ* powder diffraction data of CuInSe$_2$ were collected at the ID15B high energy beamline at the European synchrotron radiation facility (ESRF) in Grenoble, France. The temperature range of the measurement was 300°C to 875°C. During measurements the sample was heated in a ceramic oven with a heating rate of 300K/h, 100K before the expected phase transition temperature the heating rate was changed to 38K/h. In this region one measurement was performed at every degree. The exposure time was 10 seconds. Further experimental details can be found in Schorr & Geandier (2006).

A two-dimensional simulated Guinier plot (prepared with the Powder 3D software (Hinrichsen *et al.*, 2006)) of the obtained powder diffraction data is shown in Figure 3.10. For this plot the observed intensity is plotted in dependence on the diffraction angle 2θ and temperature. The phase transition can easily be recognized as several diffraction peaks vanish in the high temperature (HT) phase, while others continue to exist.
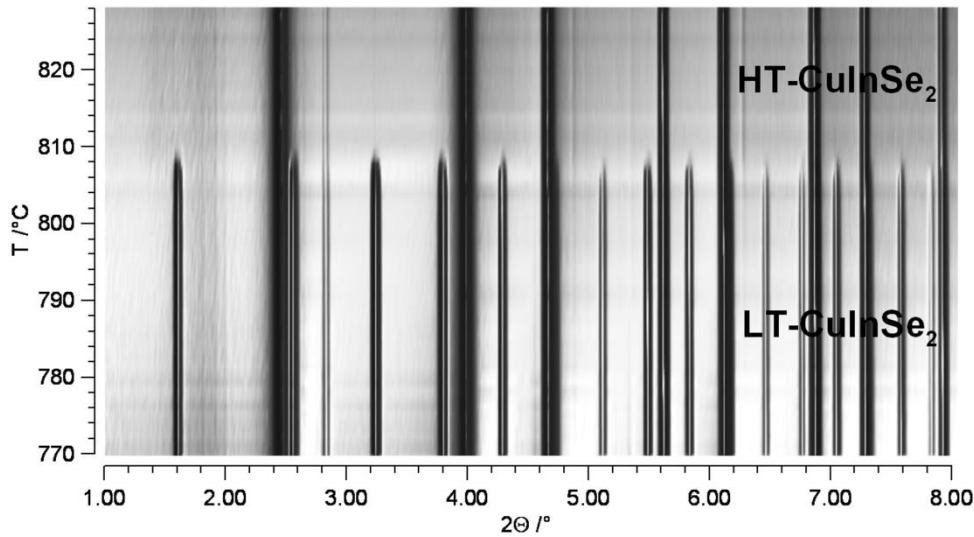
Figure 3.10: So-called simulated two-dimensional temperature dependent Guinier plot of CuInSe$_2$ in the temperature range from 770°C ≤ T ≤ 830°C. The phase transition temperature can be seen in the disappearance of several peaks. The low (LT) and the high temperature (HT) phase are labelled.

3.3.3   Method

CuInSe$_2$ exhibits a structural phase transition from the tetragonal (space group $I\overline{4}2d$) low symmetry structure to a cubic (space group $F\overline{4}3m$) parent structure at a temperature of 808°C (Schorr & Geandier, 2006; Müller *et al.*, 2011). Between those two structures a group-subgroup relation can be established. The corresponding Bärnighausen tree (Bärnighausen, 1980) of the present transition is plotted in Figure 3.11. In total three steps are needed to perform the transition. The exact transition path is: $F\overline{4}3m \rightarrow I\overline{4}m2 \rightarrow P\overline{4}n2 \rightarrow I\overline{4}2d$.

The first step is a translationengleiche transformation of index 3. There is no change in origin, though two axes are changed. This causes a reduction of the site symmetry for both Wyckoff positions within the structure as well as a reduction of their site multiplicity from four to two.

The second transition is klassengleiche with index 2. This transition causes a change in centring from a body centred to a primitive unit cell in combination with a further reduction of the site symmetry for both Wyckoff positions.

The final step is again a klassengleiche transition with index 2. The transition is realised by a change in the axes. The c-axis is doubled, while a and b are transferred to $(a + b)$ and $(a - b)$. The centring changes from primitive to body centred. The Wyckoff position $2a$ within $P\overline{4}n2$ is split in two distinct positions $4a$ and $4b$. In case of the present transition copper occupies the $4a$ site while indium occupies $4b$. The position of selenium changes from $2c$ in $P\overline{4}n2$ to $8d$.
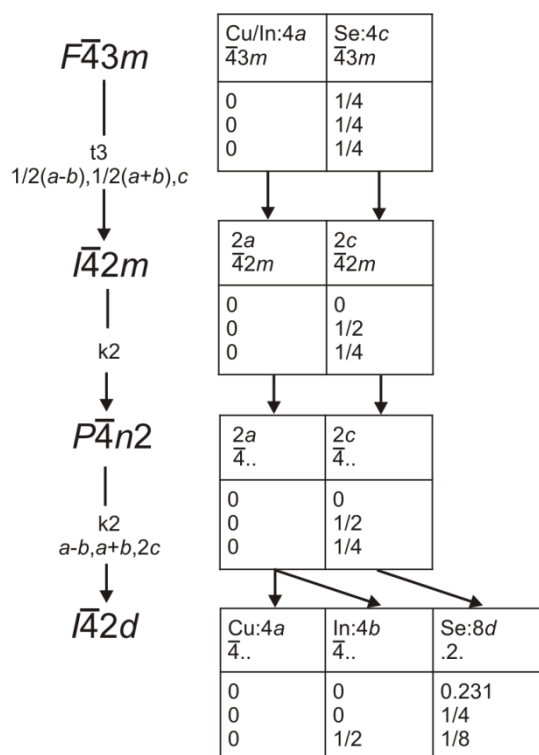
Figure 3.11: Bärnighausen tree of the group-subgroup relation and the atomic positions of the involved phases in the structural phase transition of $CuInSe_2$.

The symmetry mode decomposition of the low symmetry distorted structure into modes of the high symmetry cubic parent was performed with the ISODISTORT software (Campbell *et al.*, 2006) using CIFs of parent and LS structure.

Using ISODISTORT the following picture of the phase transition is obtained. Obviously it agrees with the one derived from the Bärnighausen tree. The LS structure of $CuInSe_2$ can be derived by doubling the cubic parent structure in one direction (denoted as *c*-axis) and a slight tetragonal distortion causing an elongation of the *c*-axis, while accordingly the *a*-axis is compressed. Additionally, the position of the selenium atom changes from a special Wyckoff $(4c, F\bar{4}3m)$ to a more general Wyckoff position $(24g, F\bar{4}3m)$ which is equal to the Wyckoff position $8d$ in space group $I\bar{4}2d$. In the LS phase copper and indium occupy distinct positions (Wyckoff position $4a$ and $4c$ respectively), while in the HS phase they are occupationally disordered at those positions (Figure 3.12) (Müller *et al.*, 2011).

This indicates that three different types of symmetry modes are needed to describe the phase transition. Strain modes, causing the distortion of the lattice, one displacive symmetry mode that influences the position of the selenium atoms and occupancy modes which are responsible for the splitting of the Wyckoff positions in the low symmetry phase.

From ISODISTORT the following modes are obtained:

- one displacive mode named a_1, which changes the x-position of the Se atom:

    a_1 F-43m [1/2,1,0]W1(0,0,0,0,a,a)[Se1:c]T2(a)

- two symmetry adapted strain modes named s_1 and s_2, one (s_1) reflects the thermal expansion, the other (s_2) causes the tetragonal distortion:

    s_1 F-43m [0,0,0]GM1(a)strain(a)

    s_2 F-43m [0,0,0]GM3(a,0)strain(a)

• four occupancy modes, causing an ordering of Cu and In atoms to distinct positions in the LS phase[7]:

   b_1 F-43m[0,0,0]GM1(a)[Cu1:a]order(a)

   b_2 F-43m[1/2,1,0]W1(0,0,a,-a,0,0)[Cu1:a]order(a)

   b_3 F-43m[0,0,0]GM1(a)[In1:a]order(a)

   b_4 F-43m[1/2,1,0]W1(0,0,a,-a,0,0)[In1:a]order(a)
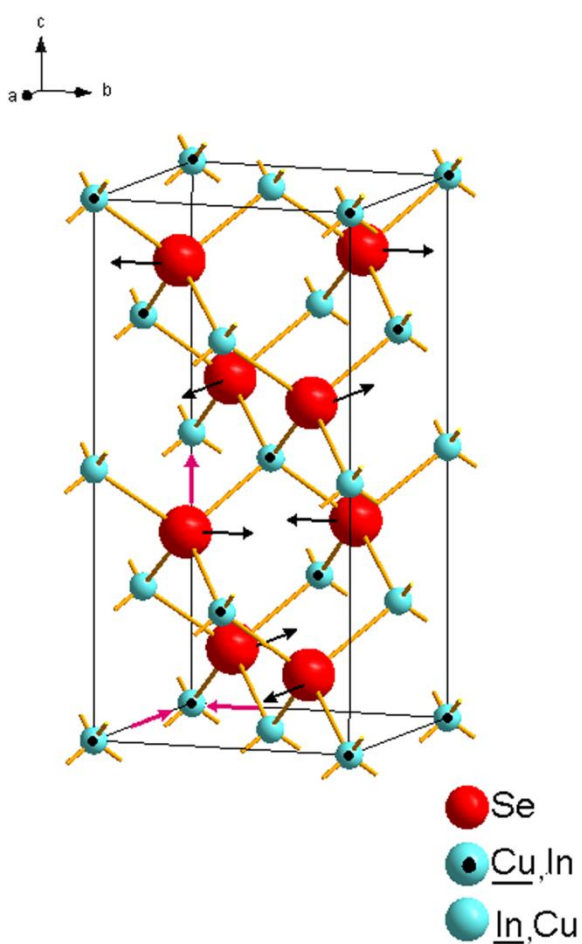
Figure 3.12: Crystal structure of tetragonal $CuInSe_2$. The pink arrows indicate the directions of the tetragonal distortion; the black arrows indicate the movement of the selenium atoms (red). The two different cation positions are given by blue atoms. Cation position 1 (Wyckoff position $4a$; $I\bar{4}2d$) (blue atoms with black dot) is preferred by copper, while cation position 2 (Wyckoff position $4b$; $I\bar{4}2d$) (blue atoms) is preferred by indium in the LS phase.

---

[7] At the time the present analysis was performed, the occupancy modes were not yet included within ISODISTORT. Therefore a different description was used within the analysis.

ISODISTORT (Campbell *et al.*, 2006) offers a graphical applet (Figure 3.13) of the crystal structure and the determined symmetry modes providing a tool to visually study the influences of the individual modes.
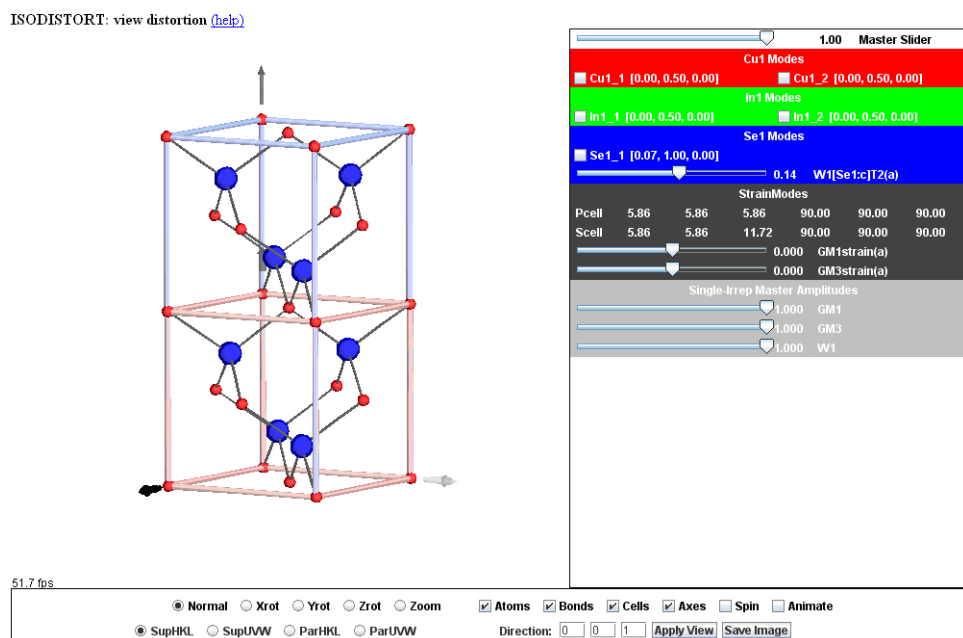
Figure 3.13: Screenshot of the distortion applet obtained from the ISODISTORT software (Campbell *et al.*, 2006). The amplitudes of the individual symmetry modes can be changed by the slider on the right side. The master slider changes all symmetry modes simultaneously.

Furthermore, using ISODISTORT, a text file, which is compatible with TOAPS, can be obtained. It contains several equations, which are used to calculate lattice parameters and atomic coordinates in dependence on the observed modes.

The *x* position of the Se atom *x(Se)* is calculated by the following equation using the displacive mode a_1:

$$x(Se) = 0.25 - 0.08529a_1 , \tag{3.26}$$

and the lattice parameters a and c are calculated by:

$$a = p_0\left[\left(s_1 - 0.5s_2\right) + 1\right] \tag{3.27}$$

and

$$c = p_0\left[\left(s_1 + s_2\right) + 1\right] \tag{3.28}$$

using the two strain modes s_1 and s_2, as well as the cubic lattice parameter p_0 given in the CIF of the parent phase.

Within parametric Rietveld refinement the modes derived from ISODISTORT plus additional parameters were parameterised. The additional parameters within parametric Rietveld refinement are the atomic displacement factors b_{C1}, b_{C2} and b_{Se} as they exhibit power law behaviour, too (Müller *et al.*, 2011), which is not unusual for atomic displacement parameters (Cowley, 1980). The displacement factors b_{C1} and b_{C2} describe the behaviour of cations on Wyckoff site 4*a* and 4*b* in space group $I\bar{4}2d$ respectively, independent from their species.

In order to define the equations for parameterisation of all parameters (a_1, s_1, s_2, occ, b_{C1}, b_{C2} and b_{Se}) the investigated temperature range was subdivided in three regions:

- a low temperature range (tetragonal space group)

- the transition region

- a high temperature range (cubic space group)

For parameterization linear functions, power law functions (equation (3.2)) and refineable or fixed values were used, e.g. the s_1 parameter was described by a single function in the low temperature region and a second linear function at the high temperature region, in the transition region, a power law function was subtracted from the high temperature linear function. In order to find appropriate starting values sequential Rietveld refinements were used first (Müller *et al.*, 2011).

3.3.4   Results

The present phase transition was studied using sequential and parametric Rietveld refinement. Within sequential refinement no constraints or restraints were implemented at all. Within parametric Rietveld refinement a_1, s_1, s_2, occ, b_{C1}, b_{C2} and b_{Se} were described using the previously defined functions. Two plots of the sequential and parametric refinement results are shown in Figure 3.14. The almost flat difference curve (grey) indicates that the fits are satisfactory as well in the sequential as in the parametric Rietveld refinement.
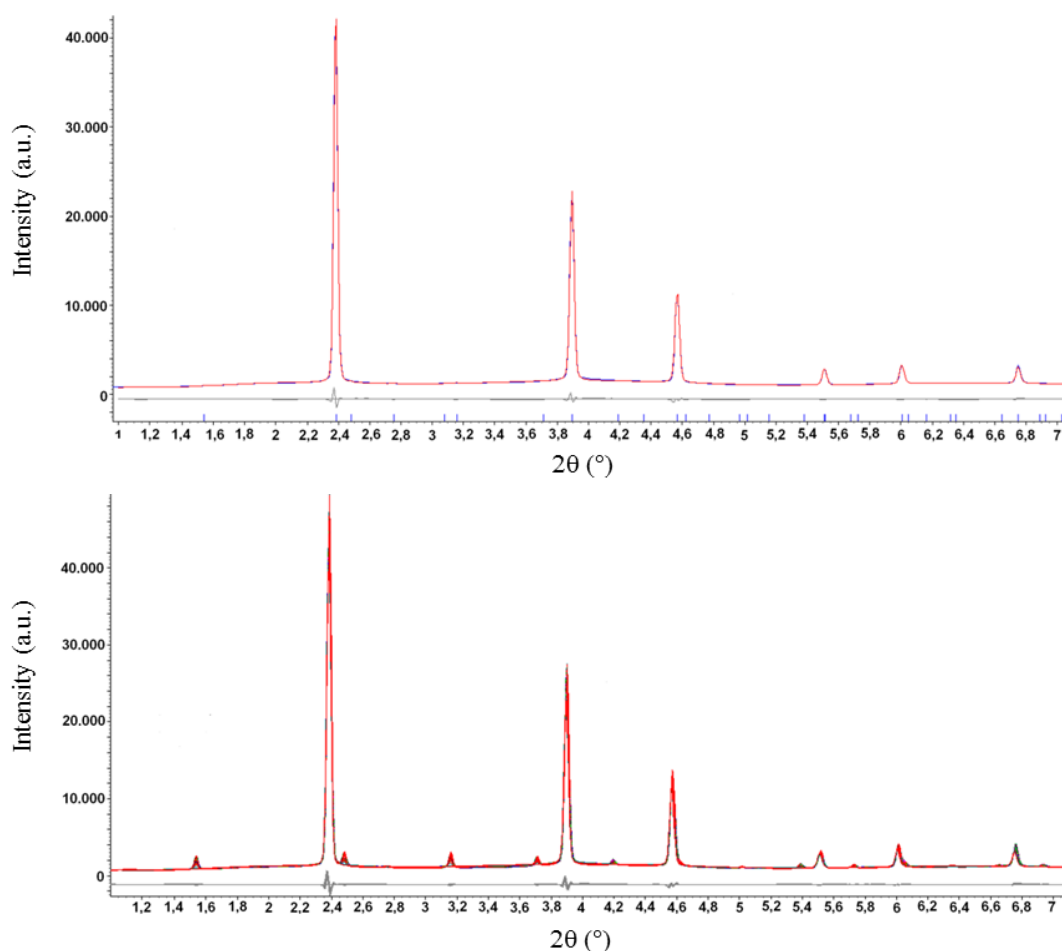
Figure 3.14: Top: Plot of a single symmetry-mode Rietveld refinement of the cubic $CuInSe_2$ phase at 827°C. Bottom: Plot of the parametric Rietveld refinement of the phase transition of $CuInSe_2$ in the temperature range from 786°C to 828°C. Observed and calculated intensities and their differences are plotted for all temperature in steps of 1K on top of each other.

The agreement between sequential and parametric refinement can be judged by comparing the R_{wp} values for both types of refinement (see Figure 3.15). In general, the obtained values should be in the same range. Slightly higher values for parametric refinements are expected; as the sequential refinement was unconstrained allowing some parameters to compensate for additional features of the powder pattern (Müller *et al.*, 2011).
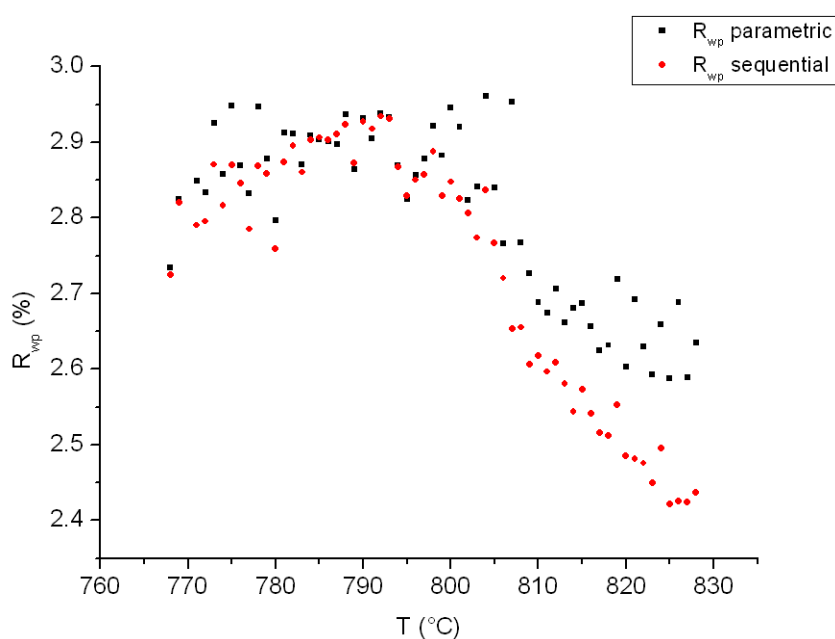
Figure 3.15: R_{wp} values obtained in parametric and sequential Rietveld refinement of CuInSe$_2$ in dependence on temperature.

All parameters used in parametric refinement could be modelled in good agreement with the values obtained for sequential Rietveld refinement. This can be seen in Figure 3.16 to Figure 3.18. For sequential refinement, some of the parameters are showing a deviation from their ideal values within the HS phase, which is caused by the unconstrained fit. The a_1 parameter, which is responsible for the x coordinate of the selenium atoms, shows a slight deviation from the ideal value of zero in the cubic phase. This causes a shift of the x-position of the atom of 0.004. Furthermore the s_2

strain parameter shows large values for the estimated standard deviations (esd) in the cubic phase (Müller *et al.*, 2011).
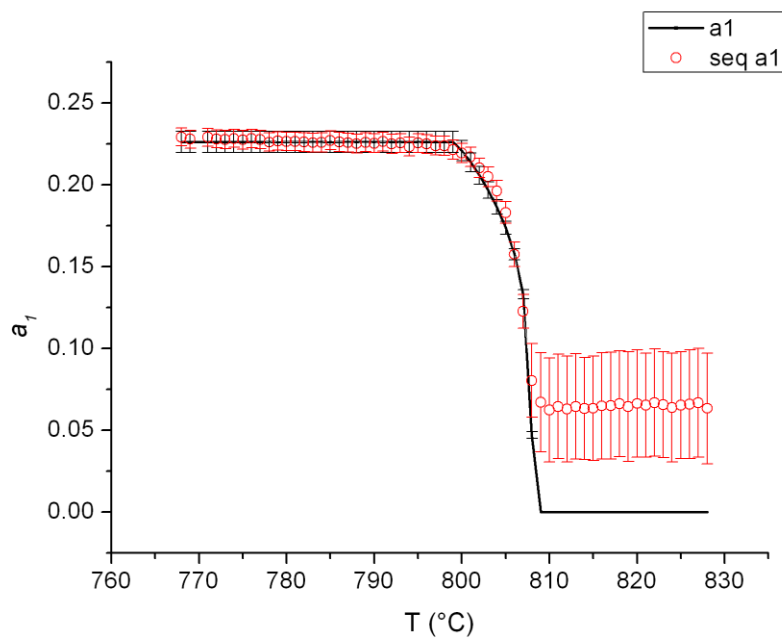
Figure 3.16: Values for the a_1 parameter obtained in sequential and parametric Rietveld refinement of CuInSe$_2$. The values show good agreement in the low temperature and transition region.
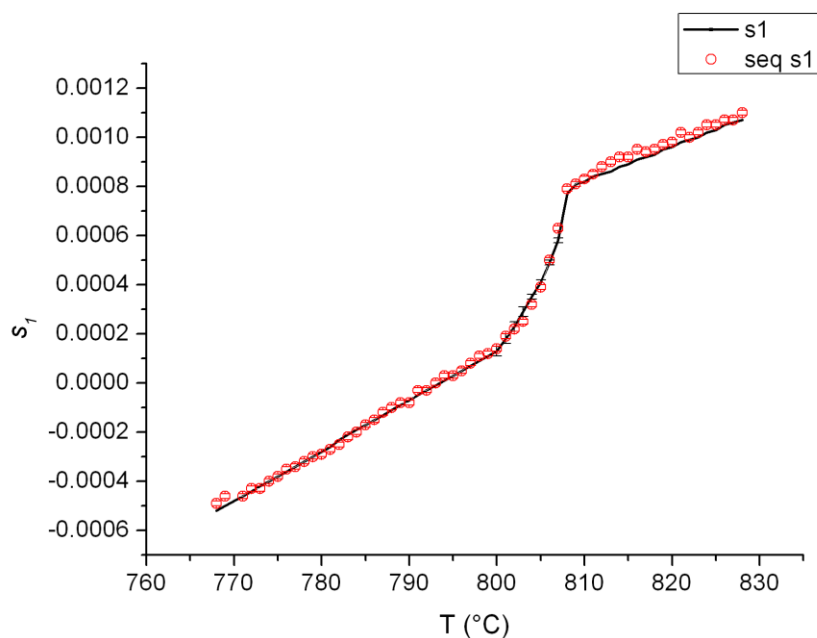
Figure 3.17: Values for the s_1 parameter obtained in sequential and parametric Rietveld refinement of CuInSe$_2$. The values show very good agreement for the whole temperature range.
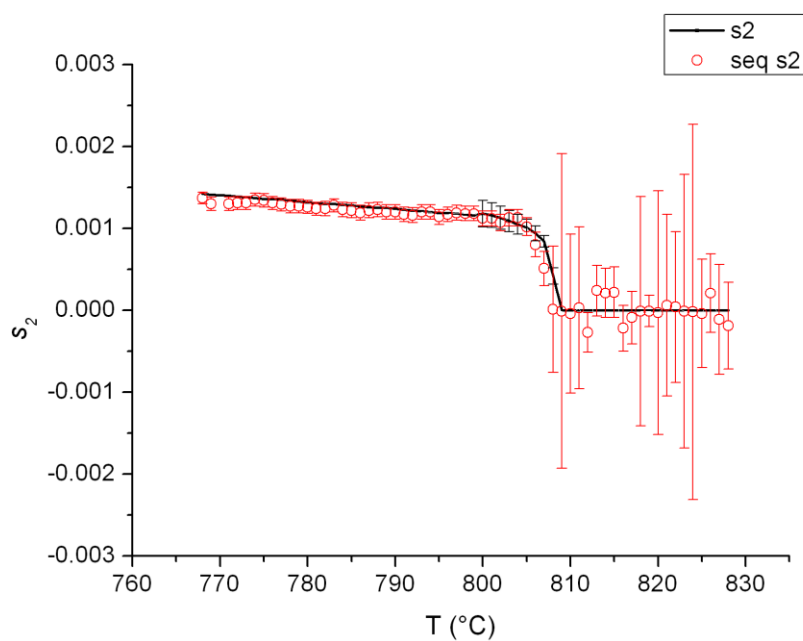
Figure 3.18: Values for the s_2 parameter and respective esd's obtained in sequential and parametric Rietveld refinement of CuInSe$_2$.

In Figure 3.19, the copper occupancy of the cation position 1 (preferred by copper) is shown. From those values it can be concluded, that within the tetragonal phase two distinct positions, one for each cation, can be differentiated. During the structural phase transition this ordering vanishes.

The atomic displacement parameters are given in Figure 3.20. The different parameters refer to different atomic positions: (b_{C1} stands for cation position 1 (Wyckoff position $4a; I\overline{4}2d$), b_{C2} for cation position 2 (Wyckoff position $4b; I\overline{4}2d$) and b_{Se} for selenium. Initially the parameters increase with temperature as expected due to an increase in thermal vibration. In the region of the phase transition b_{C1} and b_{C2}, which are clearly different in the tetragonal phase, approach each other and b_{C1} decreases drastically. In the cubic phase atoms on both cation positions have the same isotropic displacement parameter (Müller *et al.*, 2011).
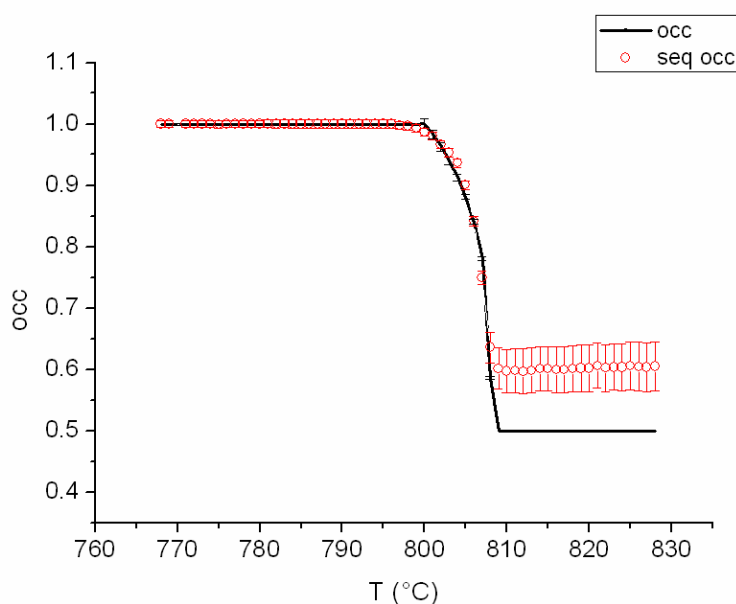
Figure 3.19: Values for the occupancy of Wyckoff position $4a$ ($I\overline{4}2d$) with copper. Results from sequential and parametric Rietveld refinement of CuInSe$_2$ and their esd's are plotted.
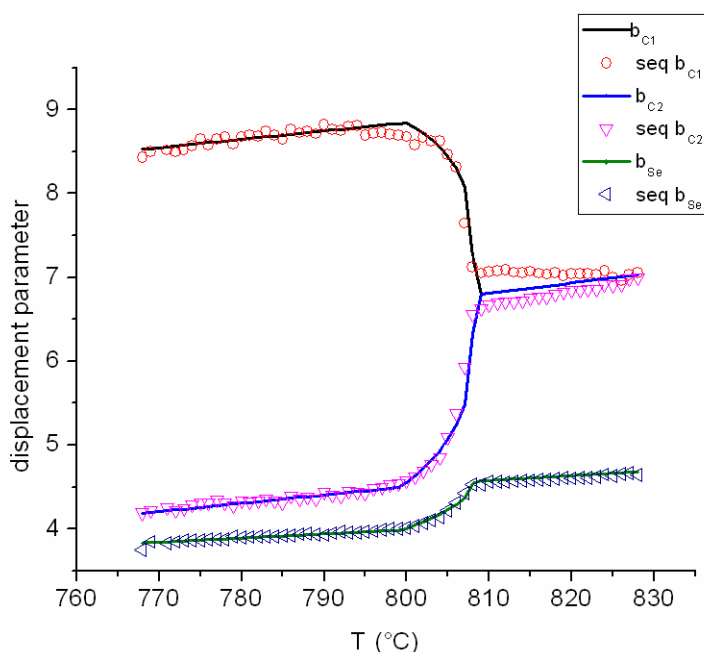
Figure 3.20: Values obtained in sequential and parametric Rietveld refinement of CuInSe$_2$ for the displacement parameter for cation site 1 (b_{C1}), cation site 2 (b_{C2}) and Se (b_{Se}). For better visibility esd's, which are in between 0.5 and 1, are not plotted.

The primary order parameter of this transition is the W1 mode according to ISODISTORT. This mode is not continuous which is also shown in the results obtained from parametric Rietveld refinement. An overview of all obtained values is given in Table 3.5.

The critical exponent β for the modelling of the a_1 parameter shows a value of 0.24(1). This indicates a tricritical displacive phase transition (Salje, 1990). The isothermal strain s_1 is related to the primary order parameter in this manner: $s_1 \sim Q a_1^2$. Such a coupling between strain and order parameters is expected for spontaneous strain which appears in co-elastic phase transitions as the present transition. The critical exponent of the s_1 parameter obtained in parametric Rietveld refinement is 0.49(2) (Müller *et al.*, 2011).

Table 3.5: Power law coefficients and critical exponents obtained from parametric Rietveld refinement of $CuInSe_2$ in dependence on temperature.

mode name	f	β
a_1	0.133(3)	0.24(1)
s_1	0.00020(1)	0.49(2)
s_2	0.00084(7)	0.16(5)
occ	0.279(3)	0.28(1)
b_{C1}	1.28(4)	0.24(1)
b_{C2}	1.28(4)	0.24(1)
b_{Se}	0.18(2)	0.49(2)

These behaviours are also reflected in the isotropic thermal displacement parameter. The displacement parameter of the cations b_{C1} and b_{C2} follow a power law function with the same exponent as the a_1 parameter, while the isotropic displacement parameter of the selenium atom b_{Se} shows a comparable behaviour as s_1 (Müller *et al.*, 2011).

For the two remaining parameters occupancy occ and strain s_2 critical exponents of 0.28(1) and 0.16(5) respectively are observed. These values do not agree with the other observed values which can be explained with a tricritical phase transition. Though, values lower than 0.25 can be obtained for dynamic order-disorder transitions (e.g. Mountstevens *et al.*, 2005; Goodwin *et al.*, 2007) or for first-order transitions, while a critical exponent of about 0.3 indicates a three-dimensional ordering phenomenon according to the Ising model (Als-Nielsen & Dietrich, 1967). So, the present phase transition combines an order-disorder and a displacive transition as stated before by Schorr and Geandier (2006) (Müller *et al.*, 2011).

3.3.5   Conclusion

Parametric Rietveld refinement can offer advantages with respect to traditional sequential Rietveld refinement. Assuming the validity of the underlying model, more detailed understanding of the analysed system can be obtained. The implementation of equations to describe the evolution of parameters, as shown for the symmetry modes in the present work, reduces the estimated standard deviations leading to more reliable results even in case of lower quality diffraction data (Müller *et al.*, 2011).

A comparison of the results obtained in the present study with the results previously obtained by Schorr and Geandier shows that in all cases the power law exponents are in agreement within the esd's. For the displacement of the Se atom a power law exponent of 0.19(7) (here: 0.24(1)), for the tetragonal distortion $\eta = c/2a$ an exponent of 0.20(4) (here: 0.16(5)) and for the occupancy an exponent of 0.35(7) (here: 0.28(1)) are reported (Müller *et al.*, 2011).

3.4 Rigid body rotations during the high temperature phase transition of Mg[H$_2$O]RbBr$_3$

A publication of parts of the work presented in this chapter is submitted: Melanie Müller, Robert E. Dinnebier, Ann-Christin Dippel, Harold T. Stokes and Branton J. Campbell: *A symmetry-mode description of rigid-body-rotations in crystalline solids: a case study of Mg[H$_2$O]$_6$RbBr$_3$*.

The sample was synthesized by Patrick Merz (formerly Max Planck Institute for Solid State Research). The laboratory measurement was performed by Christine Stefani, while the *in-situ* synchrotron data was measured by Frank Adams, Oxana Magdysyuk and Tomče Runčevski (all Max Planck Institute for Solid State Research) with support of Ann-Christin Dippel (Deutsches Elektronen-Synchrotron DESY, Hamburg, Germany). Harold T. Stokes and Branton J. Campbell (Department of Physics & Astronomy, Brigham Young University, Provo, USA) implemented the necessary modifications into ISODISTORT and contributed to the theoretical background.

3.4.1 Introduction

The application of rigid body symmetry modes to quantitative rigid body analysis is demonstrated for octahedral rotations in Mg[H$_2$O]$_6$RbBr$_3$. Rigid body rotations are treated as axial in the context of crystallographic space groups. The room temperature (RT) crystal structure of the Mg[H$_2$O]$_6$RbBr$_3$ double salt is characterized by a corner-sharing network of RbBr$_6$ octahedra containing isolated Mg(OH$_2$)$_6$ octahedra within its voids. Upon heating a phase transition occurs at 138°C, whereupon the Mg(OH$_2$)$_6$ octahedra experience a substantial rigid body rotation. Parametric and sequential refinements of the temperature-dependent structure were performed using four model types: (1) traditional atomic *xyz* coordinates for each atom, (2) traditional rigid body parameters, (3) purely displacive symmetry modes, and (4) rigid body symmetry modes (Müller *et al.*, 2013).

3.4.1.1   The crystal structure of $Mg[H_2O]_6RbBr_3$

The room temperature crystal structure of $Mg[H_2O]_6RbBr_3$ was first described by Dinnebier *et al.* (2008) and found to be isostructural to other magnesium double salts, e.g. $Mg[H_2O]_6RbCl_3$ (Marsh, 1992) or $Mg[H_2O]_6(NH_4)Cl_3$ (Solans *et al.*, 1983). The material is composed of a three-dimensional network of vertex sharing $[RbBr_6]$ octahedra, which contains isolated $[Mg(H_2O)_6]$ octahedra in the voids of the network. The $[Mg(H_2O)_6]$ octahedra are oriented in two different ways (Figure 3.21). The compound crystallizes in the monoclinic space group $C2/c$ with $a = 9.645(3)$ Å, $b = 9.868(3)$ Å, $c = 13.791(5)$ Å and $\beta = 90.07(1)°$, close to orthorhombic symmetry.

At about 138°C, the compound undergoes a reversible phase transition. Using X-ray powder diffraction (XRD), this phase transition of $Mg[H_2O]_6RbBr_3$ and the corresponding structural changes were investigated by Dinnebier *et al.* (2008). In an open system, the phase transition occurs at approximately $T = 85°C$ (Emons *et al.*, 1991; Dinnebier *et al.*, 2008), while in a closed system it is shifted to considerably higher temperature of $T = 135°C$ (Emons *et al.*, 1991). In case of an open system, the phase transition from a monoclinic phase that crystallizes in space group $C2/c$ to a cubic phase ($Pm\bar{3}m$) (Figure 3.22) appears to be first-order (Dinnebier *et al.*, 2008), while in case of a closed system the transition is tricritical.

The cubic structure is closely related to a cubic perovskite structure (Figure 3.23) (Dinnebier *et al.*, 2008). If the central $Mg(OH_2)_6$ octahedron is replaced by its center of gravity X, the formula of $XRbBr_3$ corresponds to $BaTiO_3$ in a 1:1 fashion. Within cubic $Mg[H_2O]_6RbCl_3$, the $[Mg(H_2O)_6]$ octahedra show a four-fold orientational disorder (Dinnebier *et al.*, 2008). This phase is stable in a narrow temperature range of about 12°C, starting from 147°C, a second phase begins to form. Details about this process are given in chapter 3.4.5.
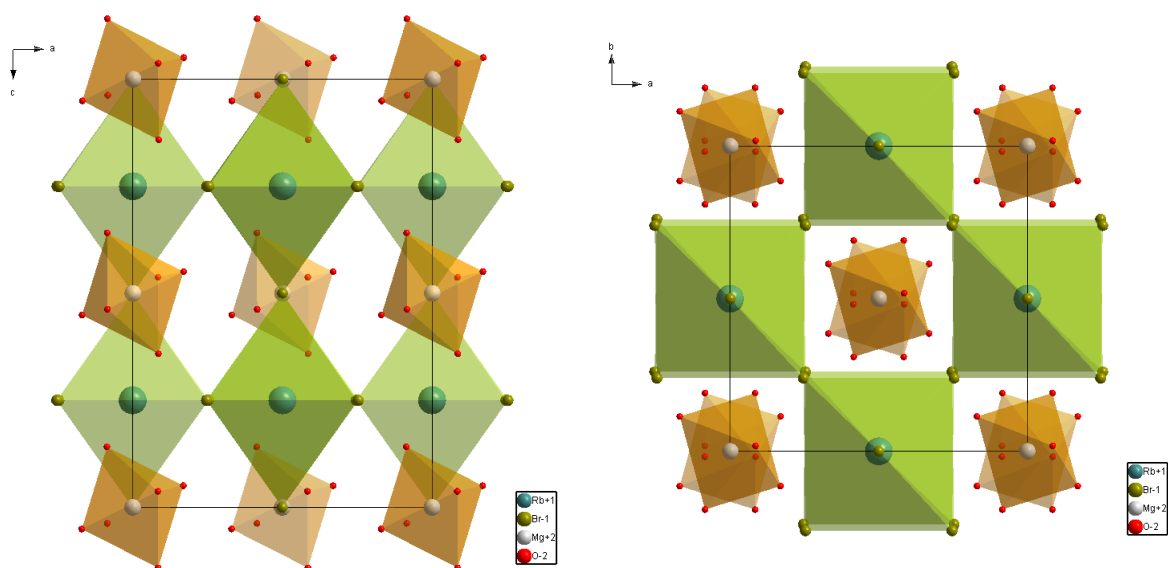
Figure 3.21: Room temperature crystal structure of $Mg[H_2O]_6RbBr_3$: Left: view along the b-axis; Right: view along c-axis.
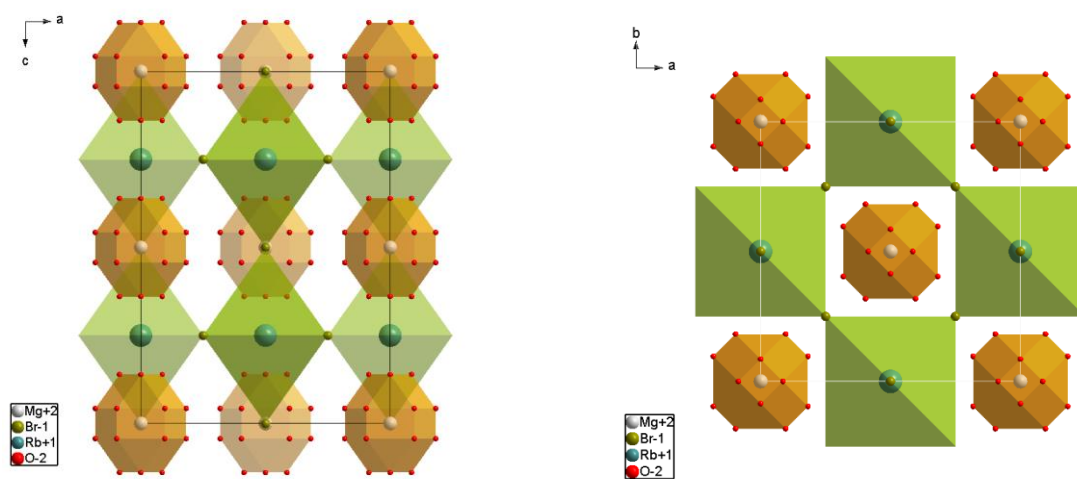
Figure 3.22: High temperature cubic crystal structure of $Mg[H_2O]_6RbBrl_3$ at $T = 139°C$: Left: view along the b-axis; Right: view along c-axis.
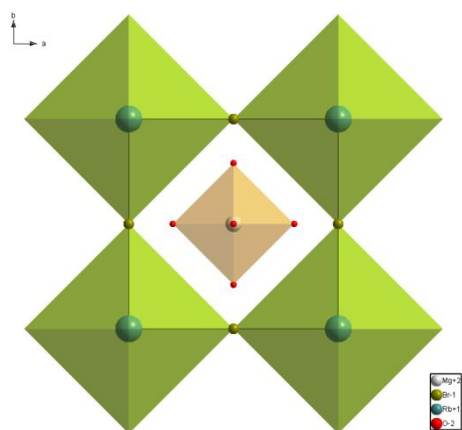
Figure 3.23: Hypothetical parent structure of $Mg[H_2O]_6RbBr_3$.

3.4.2 Sample preparation and measurement

The synthesis of $Mg[H_2O]_6RbBr_3$ was performed as stated in Dinnebier *et al*. (2008). The compound was obtained from slow isothermal crystallization from an aqueous solution containing 82.68 mg RbBr and 92.05 mg $MgBr_2$ at 50°C.

High resolution laboratory X-ray powder diffraction data of $Mg[H_2O]_6RbBr_3$ at ambient conditions were recorded using a Bruker D8 diffractometer in Debye-Scherrer geometry equipped with a Våntec-1 position sensitive detector (6° opening angle) and $CuK_{\alpha 1}$ radiation (1.540596 Å) obtained from a primary Ge(111)-Johansson monochromator. The sample was sealed in a glass capillary and rotated during the measurement in order to improve particle statistics. The instrumental profile was determined from a measurement of the NIST SRM 660a LaB_6 standard.

Temperature dependent *in-situ* powder diffraction data were collected at the high energy powder diffraction beamline P2.01 of the Petra III synchrotron in Hamburg, Germany using a wavelength of 0.20752 Å. The sample was sealed in a glass capillary and measurements were performed in the temperature range of 30°C to 249°C. Therefore the sample was heated with a constant heating rate of 2K per minute. The exposure time was 2 minutes for each measurement.

A two-dimensional simulated Guinier plot of the synchrotron powder diffraction data of $Mg[H_2O]_6RbBr_3$ prepared with the Powder 3D software (Hinrichsen *et al.*, 2006) is shown in Figure 3.24. For this plot, the observed intensity is plotted in dependence on the diffraction angle 2θ and temperature. The monoclinic to cubic phase transition can be recognized as several groups of diffraction peaks approach each other and merge in a single peak in the HS phase at about 138°C. The new phase is stable up to about 147°C. At this temperature, the formation of another phase sets in. It is clearly visible that this is a first-order process, as there is an overlap region of the two phases, and the peaks of the new phase are very different from the previous one. The few peaks that are persistent in both regions belong to a contamination phase of RbBr. At about 201°C a third transition, which is again a first-order one, sets in.
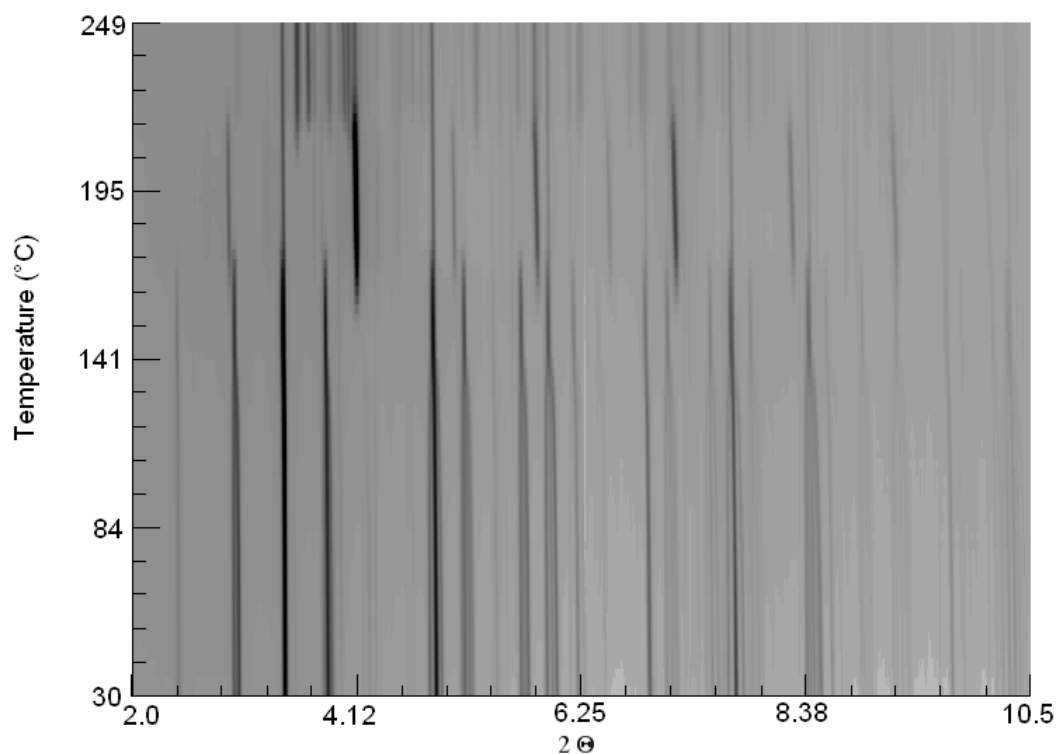
Figure 3.24: Simulated two-dimensional temperature dependent Guinier plot of synchrotron powder diffraction data of $Mg[H_2O]_6RbBr_3$. In total three phase transitions temperature can be seen. The first one at 138°C is characterized by a merging of peaks. Furthermore two first-order phase transitions set in: one at 147°C, the second at 201°C.

3.4.3   Method

Within both, parametric and sequential Rietveld refinement, four different models were used in order to describe the crystal structure of $Mg[H_2O]_6RbBr_3$ in dependence on temperature:

1) The first refinement was performed by refining atomic coordinates of general crystallographic positions (AC) within the crystal structure of $Mg[H_2O]_6RbBr_3$.

2) The crystal structure of $Mg[H_2O]_6RbBr_3$ was described using two rigid bodies (RB) of the $Mg(OH_2)_6$ and $RbBr_6$ octahedra. In case of $Mg(OH_2)_6$, three external degrees of freedom (rotations) need to be refined to obtain the correct orientation the rigid body. In case of $RbBr_6$, the orientation is determined by an internal degree of freedom (angle between Br2 and *a-c* plane). A scheme of the two rigid bodies can be seen in Figure 3.25. The corresponding z-matrices are given in Table 3.6.

3) Traditional symmetry modes were applied (SM). The symmetry mode decomposition was performed using ISODISTORT (Campbell *et al.*, 2006). In the symmetry mode refinements, out of four strain modes and 13 displacive symmetry modes, all strain modes and seven displacive modes were refined. Two of the displacive modes are related to the position of the bromine atom, while the others are related to the positions of oxygen atoms. A list of all symmetry modes can be found in Table 3.7.

4) The fourth refinement was performed using the newly introduced rigid body symmetry modes (RM). The decomposition of the crystal structure in terms of rigid body symmetry modes was also performed using the ISODISTORT software (Campbell *et al.*, 2006). In this case, a comparable number and type of external degrees of freedom as for the RB approach were obtained. Three rigid body symmetry modes (components of the axial vector) concerning the $Mg(OH_2)_6$ octahedron and one rigid body symmetry mode for the Rb-Br_6 octahedron can be refined. Rietveld refinement revealed, that all three rigid body symmetry modes of $Mg(OH_2)_6$ need to be refined, while the one for $RbBr_6$ is equal to zero. Within Rietveld refinement the same rigid bodies as used in method (2), the RB approach, were applied (see Figure 3.25).
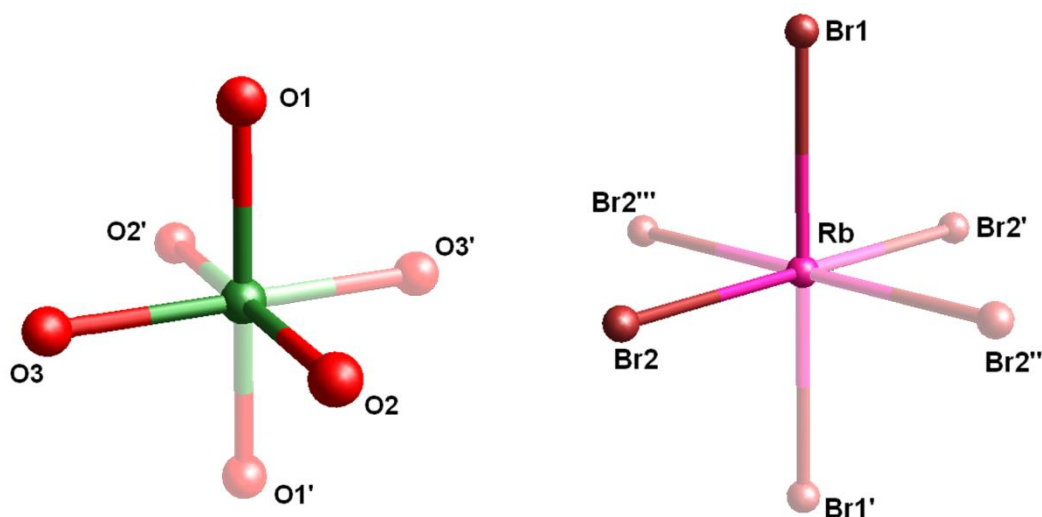
Figure 3.25: Rigid bodies which were used for the refinement of rigid bodies (RB) and rigid body symmetry modes of $Mg[H_2O]_6RbBr_3$ (RM): left: rigid body for the MgO_6 octahedron, solid atoms are implemented into the program, semi-transparent atoms are generated due to space group symmetry; right: rigid body for the $RbBr_6$, solid atoms are implemented, semi-transparent atoms are generated due to space group symmetry.

Table 3.6: Z-matrix description of the crystallographically independent atoms of the MgO_6 (a) and $RbBr_6$ (b) rigid bodies. The internal refinable parameters are displayed in bold. Not displayed atoms are generated due to crystal symmetry. Within the $RbBr_6$ RB interatomic distances are constrained to lattice parameters a, b and c.

a)

atom	distance	angle	torsion angle	related atoms
Mg1				
O1	$\boldsymbol{r_1}$			Mg1
O2	$\boldsymbol{r_2}$	90		Mg1 O1
O3	$\boldsymbol{r_3}$	90	90	Mg1 O1 O2

b)

atom	distance	angle	torsion angle	related atoms
Rb1				
Br1	$c/4$			Rb1
Br2	$\frac{1}{4}\sqrt{a^2+b^2}$	90		Rb1 Br1

Table 3.7: Symmetry modes obtained in the structural decomposition of $Mg[H_2O]_6RbBr_3$. Modes with nonzero amplitudes are displayed in bold.

mode	mode description
a_1	Pm-3m[0,1/2,0]X4-(0,0,a)[Br:d]Eu(a)
a_2	**Pm-3m[0,1/2,0]X5-(0,0,0,0,a,a)[Br:d]A2u(a)**
a_3	**Pm-3m[0,1/2,0]X5-(0,0,0,0,a,a)[Br:d]Eu(a)**
a_4	Pm-3m[0,1/2,0]X5-(0,0,0,0,a,a)[Rb:a]T1u(a)
a_5	**Pm-3m[0,0,0]GM1+(a)[O:f]A1(a)**
a_6	Pm-3m[0,0,0]GM3+(a,0)[O:f]A1(a)
a_7	**Pm-3m[0,0,0]GM4+(a,a,0)[O:f]E(a)**
a_8	Pm-3m[0,0,0]GM5+(a,b,-b)[O:f]E(a)
a_9	Pm-3m[0,0,0]GM5+(a,b,-b)[O:f]E(b)
a_{10}	**Pm-3m[0,1/2,0]X1-(0,0,a)[O:f]E(a)**
a_{11}	Pm-3m[0,1/2,0]X4-(0,0,a)[O:f]A1(a)
a_{12}	**Pm-3m[0,1/2,0]X5-(0,0,0,0,a,a)[O:f]E_1(a)**
a_{13}	**Pm-3m[0,1/2,0]X5-(0,0,0,0,a,a)[O:f]E_2(a)**
s_1	**Pm-3m[0,0,0]GM1+(a)strain(a)**
s_2	**Pm-3m[0,0,0]GM3+(a,0)strain(a)**
s_3	**Pm-3m[0,0,0]GM5+(a,b,-b)strain(a)**
s_4	**Pm-3m[0,0,0]GM5+(a,b,-b)strain(b)**

3.4.4   Results

3.4.4.1   Sequential refinement of the laboratory data

Using all four methods, sequential Rietveld refinements were performed using TOPAS (Bruker AXS, 2009). In each refinement, the background was modeled using a Chebyshev polynomial. The instrumental broadening was implemented by the Fundamental Parameter Approach (Cheary & Coelho, 1992) as available in TOPAS. Additionally to $Mg[H_2O]_6RbBr_3$, a small amount of RbBr (about 3.5wt%) is present in the sample and was therefore included in the refinements as a second phase. An

identical quality of fitting was obtained using all approaches (Figure 3.26). A comparison of lattice parameters and fractional atomic coordinates, which were refined with the four methods, showed that all values lie within two esd′s. This is also evidenced in the corresponding criteria for the quality of fit. In the following all values are given as calculated by TOPAS (Bruker AXS, 2009). For the AC refinement, the expected R value (R_{exp}) was 3.66%, the calculated one (R_P) was 4.14%, so a goodness of fit (*GOF*) of 1.48 was calculated. Using the other approaches, the following values were obtained: RB: R_P = 4.16% *GOF* = 1.49; SM: R_P = 4.24% *GOF* = 1.51 and RM: R_P = 4.17%, *GOF*= 1.49.
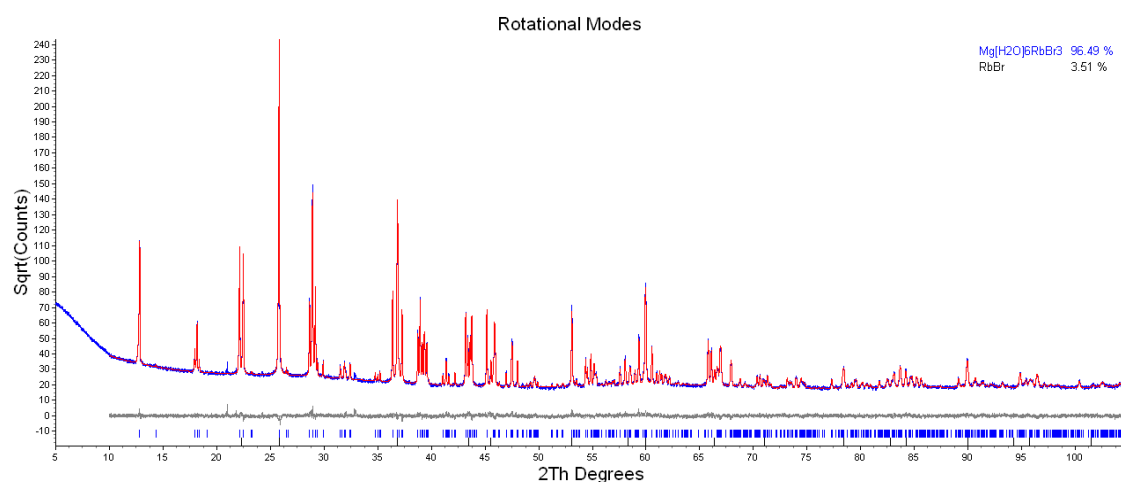
Figure 3.26: Plot of the Rietveld refinement of the RT laboratory powder diffraction pattern of Mg[H$_2$O]$_6$RbBr$_3$ using rigid body symmetry modes. The blue line corresponds to the measured powder diffraction pattern, the red line to the Rietveld fit. The difference between observed and calculated pattern is given by the grey line. Using all four methods identical fits are obtained.

3.4.4.2   Sequential and parametric refinements of the *in-situ* synchrotron data

Sequential and parametric (Stinton & Evans, 2007) Rietveld refinements of the temperature dependent *in-situ* synchrotron powder diffraction data of Mg[H$_2$O]$_6$RbBr$_3$ were performed using all four different descriptions of the structural parameters as they have been shown to refine the crystal structure with comparable quality. For all

methods sequential Rietveld refinements show that the observed structural parameters exhibit a typical power law behavior so that equation (3.2) was used for parameterisation in the LT phase.

Despite showing the power law behavior, some parameters, which are responsible for the position of oxygen atoms, tend to jump between different oxygen positions within the HT structure. This phenomenon is caused by the disorder of oxygen atoms in the HT structure and can be seen for at least one parameter in all refinement series. Apart from that, due to the monoclinic angle β close to $\beta = 90°$, the refinement of β is difficult, especially in the region of the phase transition. Therefore the sequential refinements of the β angle needed to be stabilized by restraining strain parameters within certain limits or fixing the values so that the angle β was fixed to 90° in the HT phase. Furthermore the parameters determining the positions of oxygen atoms in the HT phase were kept constant.

In general, all methods (AC; RB; SM; RM) can be used to model the present phase transition, though some methods lead to more stable results due to the smaller number of refined parameters or the more constrained structural description. The key point in refinement is the determination of the atomic positions of the oxygen atoms. Using RB and RM, the oxygen atoms are constrained by rigid bodies, therefore fewer parameters are subjected to refinement and the refinements results are stabilized. Using SM in total seven parameters are needed to describe the atomic positions of all atoms, in comparison to AC, where 13 positional parameters are refined. The influence of the different methods on the quality of refinement can be evidenced in a comparison of R_{wp} values, which were obtained in sequential and parametric Rietveld refinements (see Figure 3.27). It is visible that using traditional sequential Rietveld refinement independent from the applied method, the quality of the refinements is comparable. Though using a parametric fit, it is evident that methods RB, SM and RM give comparable results, while method AC does not lead to a satisfying fit (Figure 3.27).
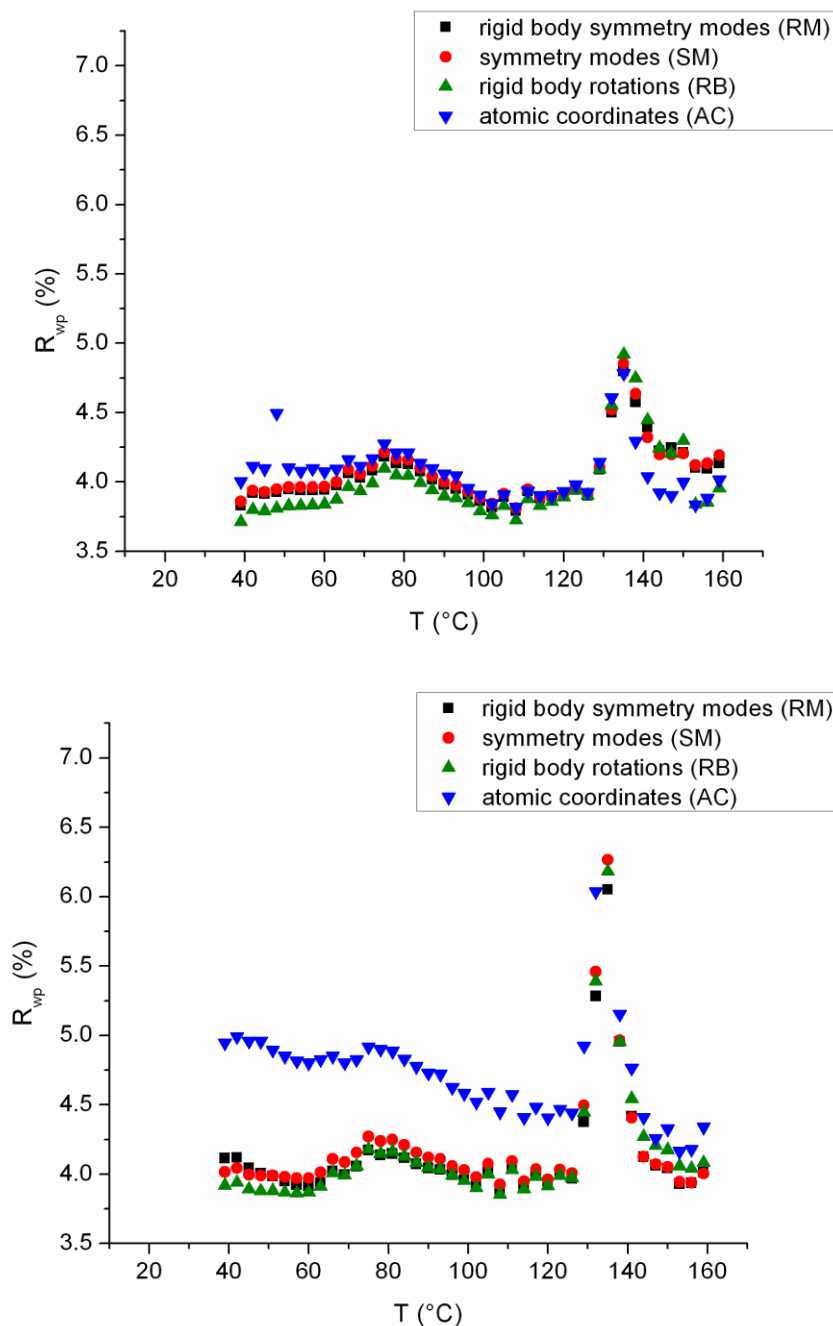
Figure 3.27: R_{wP} values in dependence on temperature as obtained from sequential (top) and parametric (bottom) Rietveld refinement of powder diffraction data of $Mg[H_2O]_6RbBr_3$ in TOPAS (Bruker AXS, 2009) using four different methods to describe the crystal structure.

Using RM in refinement not only the orientations of the RB, but also several internal parameters of the RB (interatomic distances) were refined (see Table 3.6). Figure 3.28 and Figure 3.29 show the values obtained in sequential and parametric refinement for the lattice parameters. Close to the refined transition temperature of T_{crit} = 138.08(2)°C the sequential refinement of the monoclinic angle β turned out to be unreliable due to high correlation and its value close to 90°. In refinement it can be seen, that, out of four different rotational modes, three are active and have therefore been refined. The refined values and the agreement between sequential and parametric values are shown in Figure 3.30. Those values are the components of the vector and used to calculate the orientation of the rigid bodies and the atomic positions.
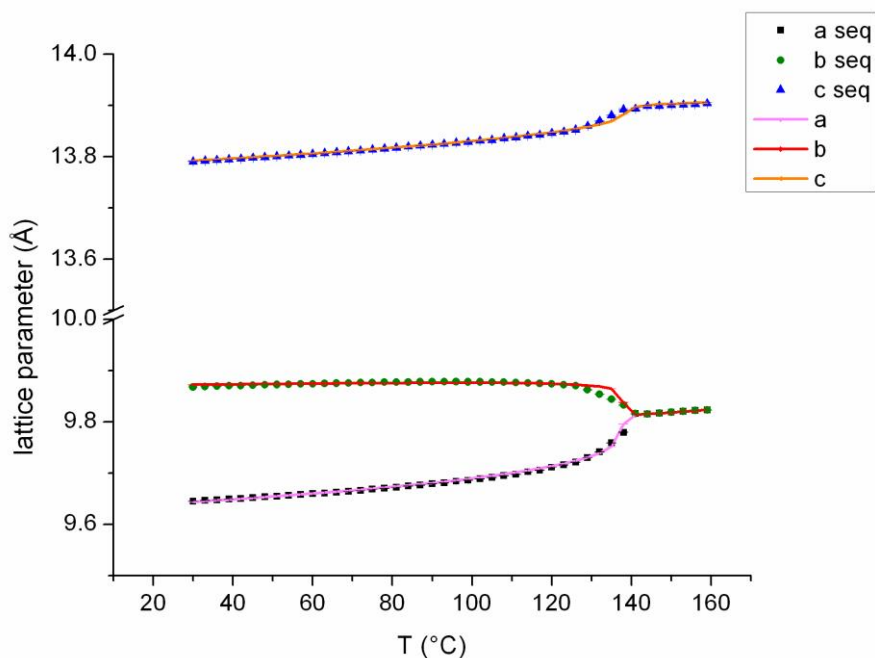
Figure 3.28: Values for lattice parameters a, b and c of $Mg[H_2O]_6RbBr_3$ obtained in sequential and parametric Rietveld refinement of the temperature dependent synchrotron powder diffraction data.
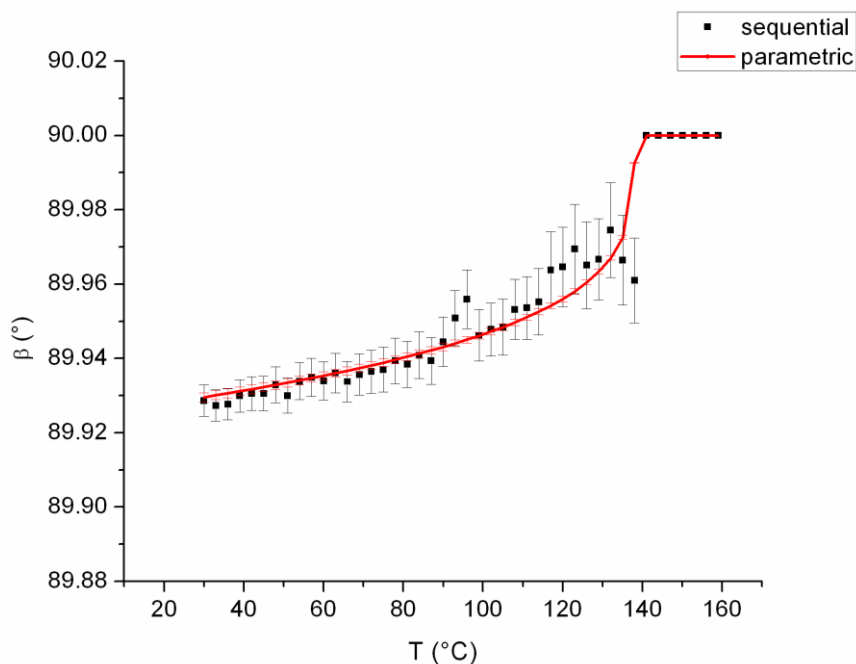
Figure 3.29: Values obtained in sequential and parametric Rietveld refinement of Mg[H$_2$O]$_6$RbBr$_3$ for angle β from synchrotron powder diffraction data. Close to the transition temperature, the values obtained are not reliable due to high correlation.
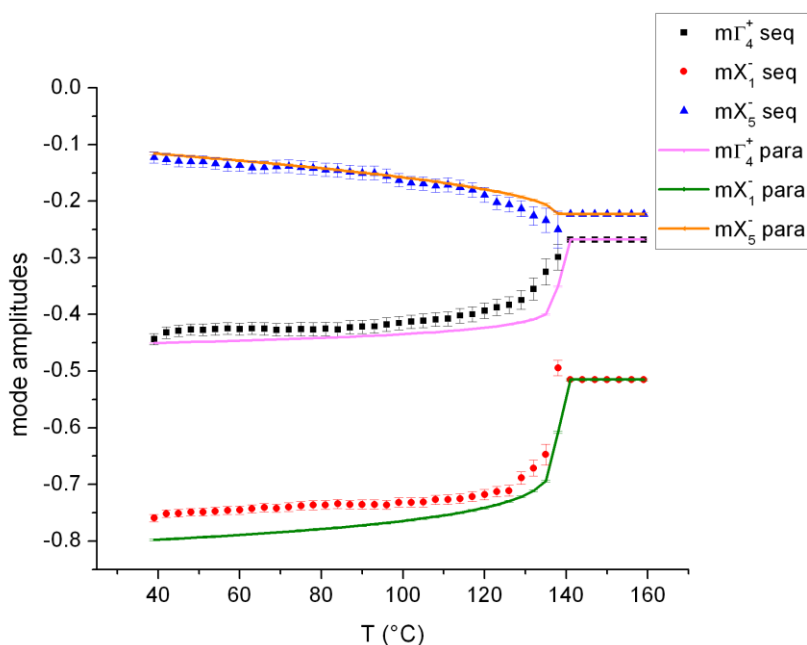
Figure 3.30: Values obtained in sequential and parametric Rietveld refinement of the temperature dependent synchrotron powder diffraction data of Mg[H$_2$O]$_6$RbBr$_3$ for the three refined rotational modes. Those values are used to calculate the orientation of the rigid bodies.

Comparable results are obtained using RB, where the structure is described by traditional rigid body rotations, though the relative esd′s are higher in comparison with those obtained for RM. The results of the sequential and parametric refinement of the rotation angles can be seen in Figure 3.31.
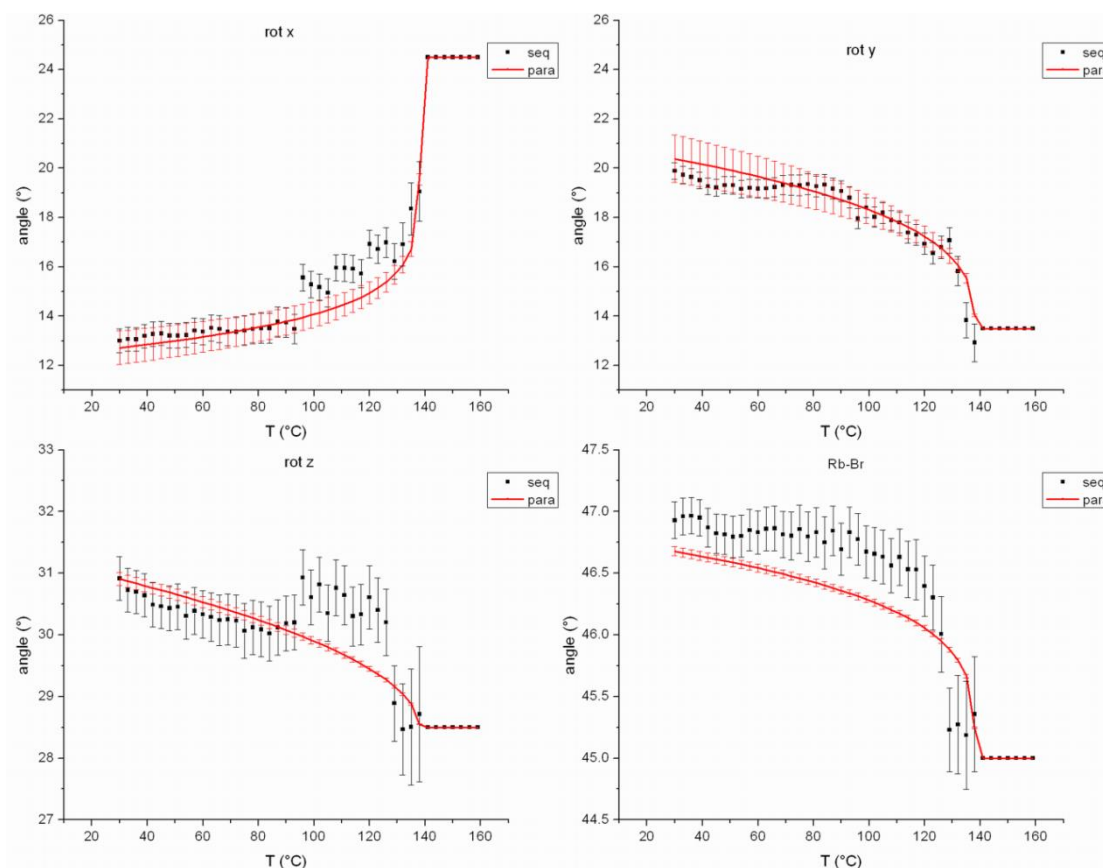
Figure 3.31: Values obtained for rigid body rotation angles in sequential and parametric Rietveld refinement of temperature dependent synchrotron powder diffraction data of Mg[H$_2$O]$_6$RbBr$_3$: Mg(OH$_2$)$_6$ octahedron around x-axis (top left); around y-axis (top right), and z-axis (bottom left) (x-, y-, z- *axes* as defined in TOPAS (Bruker AXS, 2009)) and the internal angle of the RbBr$_6$ octahedron (bottom right).

Using the SM description, the number of parameters needed to describe the crystal structure increased. Out of 13 possible displacive modes, six were found to be inactive so that seven displacive modes were refined. Even though it is possible to get

decent sequential and parametric refinements, one has to be more careful and the esd′s are larger as compared to the results of approaches using rigid bodies.

The sequential refinement applying AC is of sufficient quality, though the trends of the single parameters are not unambiguous as some parameters are highly correlated. In parametric Rietveld refinement, some trends of atomic positions are difficult to model, so the quality of the obtained results is unsatisfying.

In general, the trends obtained for lattice parameters using the four different structural descriptions are in good agreement. The critical exponents β of the four strain modes, are for both, thermal expansion (s_1) as well as for changes of c/a and c/b ratios (s_2), about 0.50(2). The value obtained for strain mode s_3 is about 0.20(1), while the one obtained for strain mode s_4, which is responsible of the monoclinic angle is about 0.25(1).

Considering critical exponents obtained from the four different models for crystal structure description of $Mg[H_2O]_6RbBr_3$ the interpretation is difficult.

Applying RB and RM descriptions, the values which were obtained for the strain modes can also be found in the parameters describing the rotation of the respective rigid body. For RM and RB there is at least one parameter with $\beta = \frac{1}{2}$, $\beta = \frac{1}{4}$ and $\beta = 0.2$ respectively. So it can be concluded that the rotation of the rigid bodies can be directly correlated to the changes in the lattice parameters. In both cases the distortion of the $RbBr_6$ octahedron is described by a power law exponent of about $\frac{1}{2}$.

In case of the description of atomic position and symmetry modes, the previously reported power law exponents of $\frac{1}{2}$, $\frac{1}{4}$, and $\frac{1}{8}$ are found, though there are no exponents of 0.2.

The phase transition of $Mg[H_2O]_6RbBr_3$ can clearly be identified as a tricritical phase transition. For such a type of transition the typical power law exponent/critical exponent would be $\frac{1}{4}$. Values of $\beta = \frac{1}{2}$ are obtained for strain modes in cases of linear-quadratic strain-order parameter coupling (Salje, 1990).

3.4.5   Thermal behavior of $Mg[H_2O]_6RbBr_3$ double salt

The thermal decomposition of double salts of the type $Mg[H_2O]_6XY_3$ ($X = Rb^+$, Cs^+, NH_4^+,…; $Y = Cl^-$, Br^-, I^-) has been subject of thermal analysis for many years, since the process is important for industrial purposes. In magnesium double salts containing water, a wide variety of possible reactions can occur during heating (Shoval *et al*., 1986). The most probable ones are:

1) Dehydration

$$Mg[H_2O]_6XY_3 \rightarrow Mg[H_2O]_{6-x}XY_3 + x\,H_2O\,(g) \hspace{3cm} (3.29)$$
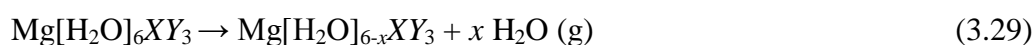
2) Thermal hydrolysis (which typically happens after or in combination with dehydration):

$$Mg[H_2O]_6XY_3 \rightarrow Mg[OH]_{6-x}XY_{3-y} + x\,H_2O\,(g) + y\,HY\,(g) \hspace{1.5cm} (3.30)$$
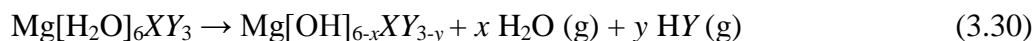
Thermal decomposition of a powder is influenced by materials parameters (e.g. the grain size), crucible geometry, heating rate or the flux of flushing gas. Decomposition reactions that form a gaseous phase are a peculiarity. In this case, the partial pressure that can build up within the sample container has a huge influence to the reaction process (e.g. the reaction temperature) as well as to the formation of new phases (Paulik & Paulik, 1986; Pyldme & Utsal, 1989). Because of this, the actual process of thermal decomposition of double salts strongly depends on the sample environment (Emons *et al*., 1984). In thermal analysis using different sample crucibles, different decomposition gas pressures are achieved and different decomposition processes and products were observed (Emons *et al*., 1987).

The compound $Mg[H_2O]_6RbBr_3$ belongs to the system MBr·MgBr$_2$·6H$_2$O (M = K, NH$_4$, Rb, Cs) and its thermal decomposition previously was investigated by Emons *et al*. (1991). They report that the compound undergoes a phase transition at about 133°C and melts incongruently at about 238.5°C. The first process, which they observed in thermal analysis, is dehydration, whereat the dehydration temperature depends on the chosen sample environment. Using a labyrinth crucible (well closed sample environment), dehydration happened at 220°C, while in a multiplate crucible

(allows diffusion of gasses) it occurs in the temperature range of 100 to 150 °C. In the following, the sample decomposes via further dehydration in combination with thermal hydrolysis at about 255°C (labyrinth crucible) or 150 to 170°C (multiplate crucible).

The newly evolving phase at 147°C within the powder diffraction pattern can be indexed in the cubic system (P23) with a lattice parameter of a = 4.087 Å. The volume of 68.27 Å^3 indicates that most likely the water is no longer within the crystal structure, and dehydration took place. In literature other ternary halides with comparable lattice parameter $a \approx 4.1$ Å, space group $Pm\overline{3}m$ and a composition of ABC$_3$ are reported (e.g. Chakhmouradian et $al.$, 2001), so a structural model according to these phases was assumed. In such a model, one metal cation occupies the origin, while the other is situated in the center of the cubic unit cell. The halide is located on the center of the faces of the cube. For the present material the structure presented in Table 3.8 was tested. In this case, there is no agreement of the intensities of the model with the intensities obtained in the powder diffraction pattern, though all reflections are represented by the model. Therefore a different model was developed: the magnesium and rubidium cations were placed in the origin, while brome situated in the center of the unit cell. So the model reminds on a CsCl type structure. In this case, it is obvious, that some disorder needs to be present within the material. Therefore the occupancies were refined and the possibility of thermal hydrolysis was implemented. From that refinement a disordered structure was obtained. The best fit was obtained for the model given in Table 3.9. The composition of the material in this case is: Mg[OH]$_{0.83}$RbBr$_{2.12}$.

Table 3.8: Initial structural model for the newly evolving phase from Mg[H2O]$_6$RbBr$_3$ at T =147°C with composition RbMgBr$_3$.

atomic species	x	y	z	occ
Rb$^+$	0	0	0	1
Mg^{2+}	½	½	½	1
Br$^-$	½	½	0	1

Table 3.9: Refined structural model for the newly evolving phase from $Mg[H_2O]_6RbBr_3$ at $T = 147°C$ with composition $Mg[OH]_{0.83}RbBr_{2.17}$.

atomic species	x	y	z	occ	Beq
Mg^{2+}	0	0	0	0.5	7.0(2)
Rb^+	0	0	0	0.5	7.0(2)
Br^-	½-0.05454	½-0.05454	½-0.05454	0.14(1)	1.5(6)
O^{2-}	½	0	0	0.14(3)	8(2)

3.4.6   Conclusion

The application of rigid body symmetry modes is demonstrated for octahedral rotations occurring during the temperature dependent phase transition of $Mg[H_2O]_6RbBr_3$. During the phase transition the MgO_6 octahedra experience a substantial rigid-body rotation while the $RbBr_6$ octahedra are distorted but not rotated. The MgO_6 rotation has three orthogonal components associated with the X_5^-, X_1^-, and Γ_4^+ irreducible representations of the parent $Pm\overline{3}m$ space group symmetry, which given the weakly first-order character of the transition, appear to be strongly coupled. Parametric and sequential refinements of the temperature-dependent structure were conducted using four model types: (1) traditional atomic *xyz* coordinates for each atom, (2) traditional rigid-body parameters, (3) purely displacive symmetry modes, and (4) rigid-body symmetry modes. We demonstrate that rigid-body symmetry modes are an especially effective parameter set for the Rietveld characterization of phase transitions involving polyhedral rotations.

At about 147°C dehydration and thermal hydrolysis set it. This process is clearly a first-order process. A structural model for the newly evolving phase is presented.

3.5   Photodimerization kinetics of 9-methylanthracene

The work presented in this chapter was published in: Ahmed F. Mabied, Melanie Müller, Robert E. Dinnebier, Shunsuke Nozawa, Manabu Hoshino, Ayana Tomita, Tokushi Sato and Shin-ichi Adachi: *A Time-Resolved Powder Diffraction Study of In-situ Photodimerization Kinetics of 9-methylanthracene using a CCD Area Detector and Parametric Rietveld Refinement*. Acta Crystallographica Section B (2012) 68(4), 424-430.

The sample purification and synchrotron measurements were performed by Ahmed F. Mabied (Department of Materials Structure Science, The Graduate University for Advanced Studies (Sokendai), Tsukuba, Japan).

3.5.1   Introduction

The kinetics of the $[4\pi + 4\pi]$ photodimerization process of crystalline 9-methylanthracene (9-MA) was investigated using time-resolved *in-situ* X-ray powder diffraction. Quantitative phase analysis was performed using sequential and parametric Rietveld refinement. The results of traditional sequential Rietveld refinement showed that the evolution of the dimerization process can be described using the Johnson-Mehl-Avrami-Kolmogorov (JMAK) model. The parameters of the JMAK equation were obtained successfully by parametric Rietveld refinement and suggest that the reaction follows heterogeneous nucleation and one-dimensional growth with a decreasing nucleation rate (Mabied *et al.*, 2012).

3.5.1.1   Photochemical reactions

Photochemical reactions are induced by the absorption of light by atoms or molecules (Turro, 1991). Therefore such processes are different from other reactions, which are driven e.g. by heat. In case of a photochemical reaction, the absorption of light leads to an electronically exited molecule. In this state the molecule can interact with other

molecules. A precondition for such a reaction is that the energy of the irradiating light matches the difference in energy between ground and excited state of the molecule (Turro, 1991).

One type of photochemical reaction is photodimerization. The reaction is well known and studied in solution and solid state. Photodimerization strongly depends on the distance between the monomers, and therefore on relative position and orientation of molecules. Schmidt developed geometrical criteria for solid state reactions, where the nearest neighbouring double bonds distance should be not more than 4.2 Å (Schmidt, 1971).

The study of such reactions by single crystals is difficult as the process can cause a destruction of the crystal (Zouev *et al.*, 2011). Therefore such processes should be studied by powder diffraction. *In-situ* X-ray powder diffraction studies on reaction kinetics are well established. Even before the development of the Rietveld method, peak intensities were used to follow kinetic reactions (e.g. Pierron *et al.*, 1967). The benefits of parametric Rietveld refinement within a kinetic study of a phase transition by powder diffraction have been previously described (Müller *et al.*, 2009). With the use of area detectors, such as CCDs, several advantages with respect to one-dimensional detectors could be achieved: a reduction of exposure time and the applicability to imperfect powder samples (e.g. with preferred orientation and/or large grain size, etc.). This is especially beneficial for *in-situ* studies (Svensson *et al.*, 1997).

Among the materials undergoing photodimerization are many organic compounds, like anthracene and its derivatives. They show a [4π + 4π] photodimerization across the 9,10-positions of the anthracene rings upon illumination of light with $\lambda > 300$ nm. A revision of the dimerization can be performed thermally or by illumination of light of $\lambda < 300$ nm, which is considered as a unique property of anthracene derivatives (Bouas-Laurent *et al.*, 2000 & Bratschkov *et al.*, 2001) (see Figure 3.32).
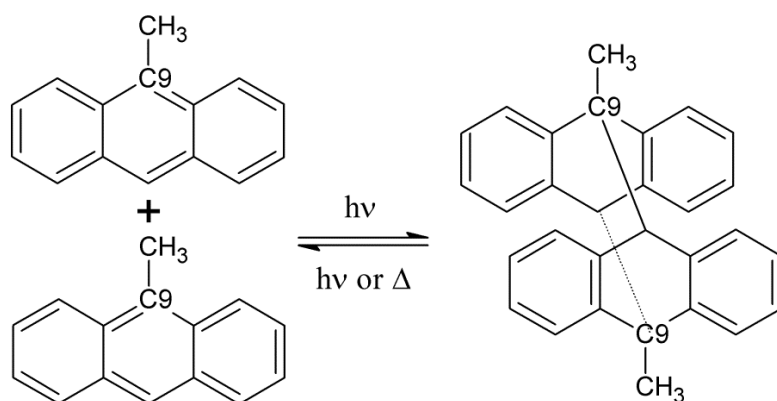
Figure 3.32: Scheme of the photodimerization process of 9-MA. The photo-dimerization can be reversed thermally or by illumination.

This property allows applications in different fields, for example as light-switched chromic devices (Tsudera *et al.*, 1997), photo-switchable receptors (Molard *et al*., 2006) or optical storage memory devices (Dvornikov & Rentzepis, 1996). Further applications such as scintillation counters are well known since the work of Bell (1948).

The $[4\pi + 4\pi]$ photodimerization reaction of 9-MA was previously studied by Turowska-Tyrk & Trzop (2003), who analysed a single crystal. Due to the single crystal disintegration, the reaction was limited at 28 % completion. Takegoshi *et al*. (1998) showed that the reaction takes place at defects of the crystal in the monomer phase. Therefore, comprehensive knowledge of the solid state reaction kinetics is needed. The aim of the present study is to obtain the kinetics parameters of the crystalline 9-MA photodimerization of bulk material at a much higher level of completion.

3.5.2   Experimental

9-methylanthracene powder (98% pure) from Wako Chemical Co. (Japan) was purified by recrystallization from acetone and hexane solvents. After that, the obtained material was ground.

In-situ X-ray powder diffraction measurements were performed at the X-ray time-resolved beam line (NW14A) of the Photon Factory Advanced Ring (PF-AR), KEK, Japan. The source of radiation at this beamline are double undulators with different period lengths; covering an energy range of 5-25 keV of different harmonics. A detailed description of the set-up of the beamline is reported in Nozawa *et al.*, 2007.

For the present experiment the X-ray beam was set to an energy of 18.0 keV (λ = 0.689 Å). About 1-2 mg of sample was filled into borosilicate glass capillaries (Hilgenberg, Germany) with a diameter of 0.4 mm. During measurement the sample was spun to improve counting statistics. The photodimerization reaction was triggered *in-situ* by illumination with a Xenon lamp, equipped with a visible mirror module (385–740 nm) (MAX-301, 300 W; Asahi Spectra). The radiation power was about 24mW/mm^2 at the sample position.

Complete Debye-Scherrer powder rings were collected at room temperature (measurement temperature = 30°C) using a Mar165 CCD detector with 2048×2048 pixels and 80 µm × 80 µm pixel size. The sample-to-detector distance was set to 150 mm.

Data conversion of the obtained powder diffraction rings to the one-dimensional data profile (2θ versus intensity) was performed using Fit2D (Hammersley *et al.*, 1996). Within the integration procedure the beam center shadows were masked and the Fit2D geometrical correction was applied (Hammersley *et al.*, 1996). The sample-to-detector distance was calibrated by a standard Si powder to be 148.9 mm. The obtained data is shown in Figure 3.33 in form of a simulated Guinier plot prepared with Powder3D (Hinrichsen *et al.*, 2006).
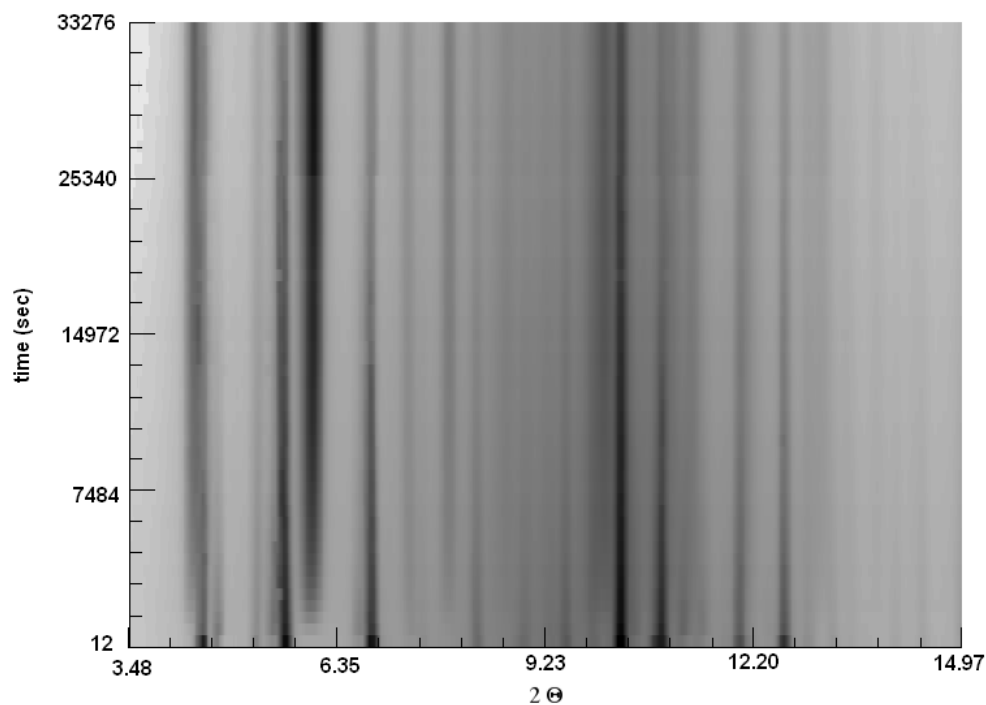
Figure 3.33: Simulated time dependent Guinier plot of the transition from 9-methylanthracene monomer to dimer. The most prominent peak of the dimer phase at $2\theta = 6°$ emerges shortly after the beginning of illumination.

3.5.3   Method

3.5.3.1   Theoretical background

The analysis of the reaction kinetics of a first-order transition can be performed by measuring the converted fraction of a material as a function of an external variable. For photoreaction the external variable is illumination time. Recently, the $[2\pi + 2\pi]$ single-crystal to single-crystal two-photon photodimerization of α-*trans*-cinnamic acid to α-truxillic acid (Benedict & Coppens, 2009) and the photodimerization of crystalline 9-Anthracenecarboxylic acid (Moré *et al.*, 2010) were analysed using the Johnson-Mehl-Avrami-Kolmogorov (JMAK) model (Johnson & Mehl (1939), Avrami (1939) and Kolmogorov (1937)), which is widely used to describe the kinetics of different reactions.

During a first-order phase transition, the progress in reaction can be described by a nucleation and growth process: initially small domains of the product phase are formed within the parent phase (nucleation). Nucleation can be heterogeneous, if it occurs at specific locations in the parent phase, or homogeneous, if its occurrence is simultaneous in the entire volume of the parent phase. The domains of the product phase then grow until all material is transformed, so to understand the nature of the reaction kinetics, information about the behavior of nucleation and growth is needed (Christian, 1965).

The JMAK equation for an isothermal transformation can be written as:

$$x(t) = 1 - \exp(-(kt)^n)$$,   (3.31)

which is equivalent to:

$$\ln(-\ln(1 - x(t))) = n\ln(t) + n\ln(k)$$ (3.32)

where t is time and $x(t)$ is the evolved fraction of the product phase at time t, k is the reaction rate and n is the Avrami exponent, which gives information about the nucleation and growth process.

A plot of equation (3.32) is called Sharp-Hancock plot (Hancock & Sharp, 1972) and yields to a straight line with a slope that is equal to n and an intercept equal to $n\ln(k)$. A comprehensive review of the development and derivation of this equation can be found elsewhere (Christian, 1965).

The Avrami exponent n, the so-called order of the reaction, describes the dimensionality of the growth of the product phase, n in the original model should be an integer number between 1 to 4, where $3 \leq n \leq 4$ for three-dimensional growth, $2 \leq n \leq 3$ for plate-like or two-dimensional growth and $1 \leq n \leq 2$ for one-dimensional growth, like rods or needles. Half integers are obtained for diffusion controlled processes (Christian, 1981). Fractions and half integer have been reported in many cases with successful interpretation (Bertmer et al., 2006; Kim et al., 2005).

In parametric Rietveld refinement the JMAK equation was used to describe the evolution of the scale factor with time as the scales factors within the Rietveld formula (equation (2.9)) determine the phase fractions. Details about this method can be found in Müller *et al*. (2009). The following equation was used:

$$s_M = \frac{-s_D M_D V_D \left[\exp\left(-(kt)^n\right) \right]}{M_M V_M \left[\exp\left(-(kt)^n\right) - 1 \right]}.$$

(3.33)

Here, s_M is the scale factor of the monomer phase, s_D the scale factor of the dimer phase, k and n are the parameters of the JMAK equation (3.31), M_D is mass of the dimer phase and M_M of the monomer phase, V_D and V_M are the volumes of the unit cells of dimer and monomer phase respectively and t is the illumination time.

3.5.3.2 Refinement

In the present case, quantitative Rietveld refinement of the *in-situ* X-ray powder diffraction data was used in order to obtain the fractions of monomer and dimer in dependence on illumination time. For the refinements, the monomer and the dimer molecules were given in form of rigid bodies in z-matrix notation which were generated using Crystallographic Information Files (CIFs) (Turowska-Tyrk & Trzop, 2003). The applied rigid bodies are illustrated in Figure 3.34 and the corresponding crystal structures in Figure 3.35 and Figure 3.36. The orientation of the rigid bodies was determined using patterns with high amount of the particular phase. Lattice parameters and orientation angles of the RB were refined. In case of the monomer phase the crystallite size was refined as well, using the same value for Lorentzian and Gaussian fraction in each pattern. In order to compensate orientational effects within the powder, a spherical harmonics function of order four was used for each phase.

Initially, traditional sequential Rietveld refinements were performed to obtain starting values for the parametric refinement.
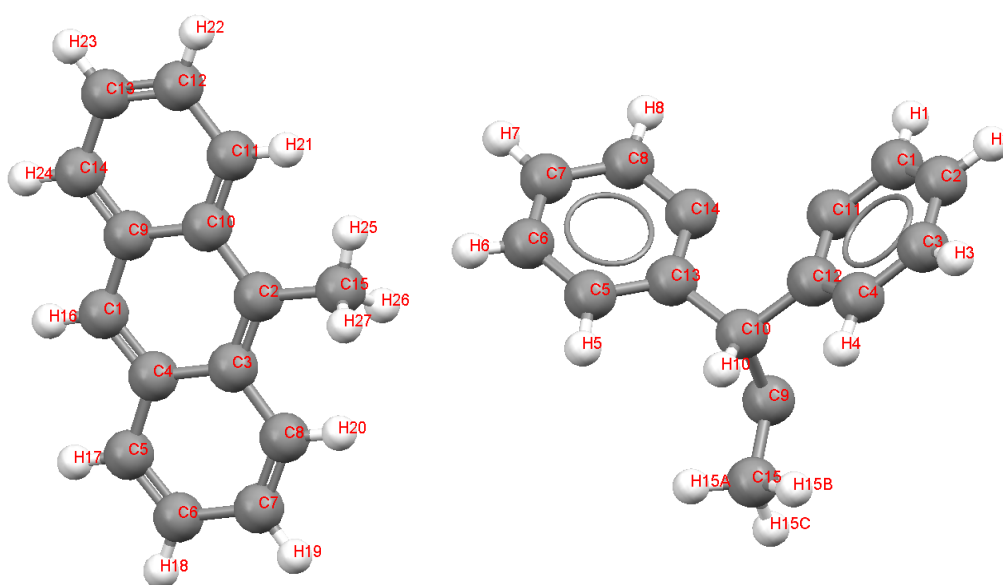
Figure 3.34: Rigid body of the monomer (left) and dimer (right) molecule of 9-methylanthracene. Due to symmetry constraints only one half of the molecule is needed for the rigid body. The remaining part of the molecule is generated by symmetry.
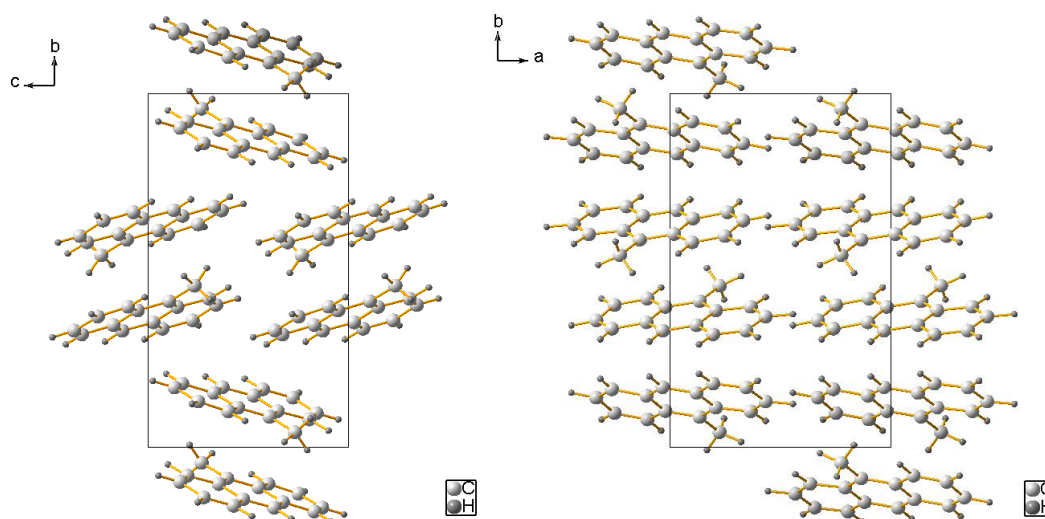
Figure 3.35: Crystal structure of the 9-methylanthracene monomer. The compound crystallises in space group $P2_1/c$. View along a-axis (left), view along c-axis (right).
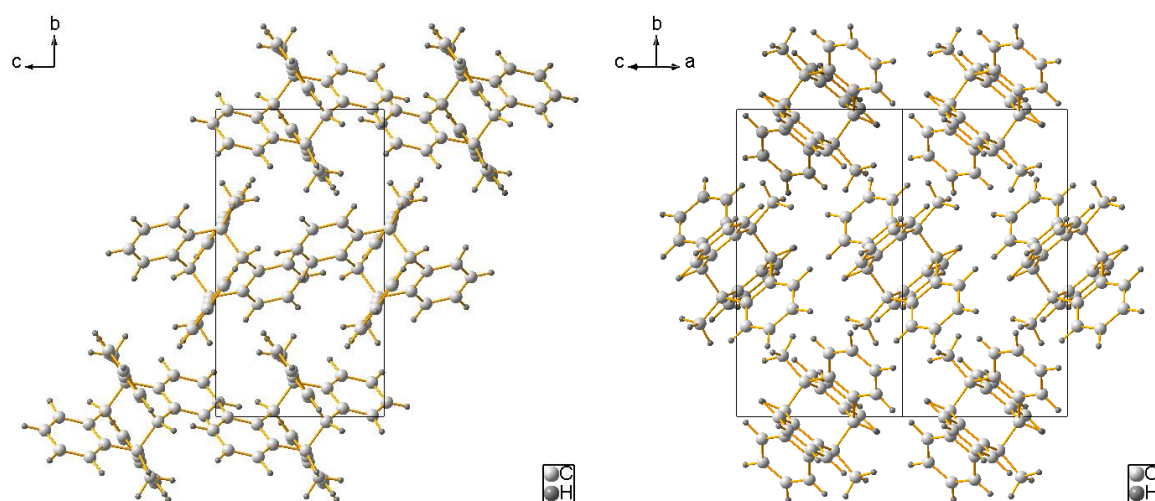
Figure 3.36: Crystal structure of the 9-methylanthracene dimer. The compound crystallises in space group $P2_1/c$. View along a-axis (left), view along [101]-axis (right). The relation between monomer and dimer is clearly visible.

3.5.4 Results

From the plots of the diffraction patterns (Figure 3.33) it can be seen that the typical diffraction peaks of the dimer phase start emerging after about 1800 seconds (about 30 minutes). Starting from that time, the evolution of the weight fractions of the monomer and dimer phases was analysed. An example of a Rietveld refinement is shown in Figure 3.37. The dimer fraction reached 63.12 weight % after 9 hours.
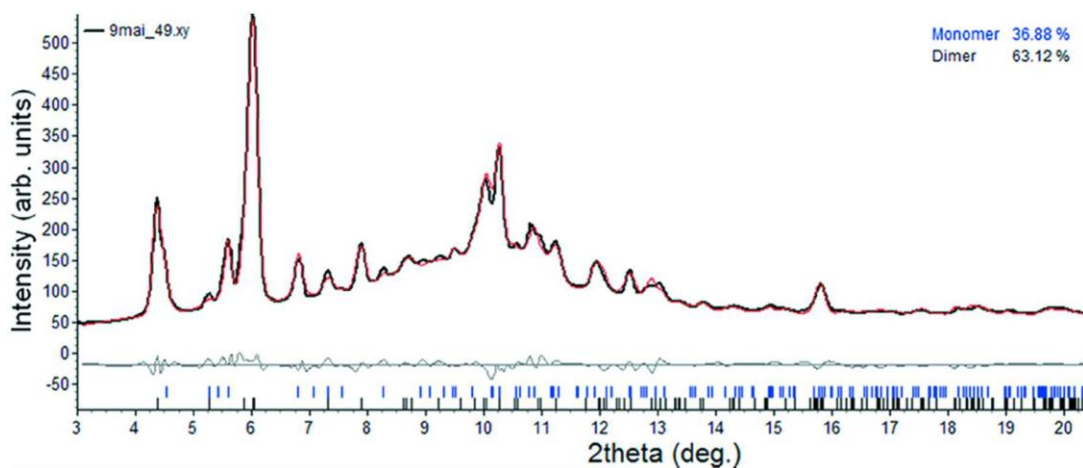
Figure 3.37: Example of the sequential Rietveld refinement of 9-methylanthracene monomer and dimer performed for a measurement after 9 hours of illumination.

A comparison of the evolution of the weight fraction for the monomer and dimer phases in dependence on time obtained from sequential and parametric Rietveld refinement is shown in Figure 3.38. The results of sequential and parametric refinements show good agreement. In Figure 3.39, a comparison of the Sharp-Hancock plot from the values obtained in sequential and parametric Rietveld refinement is shown. The resulting plot is clearly linear, indicating that the JMAK model is applicable.
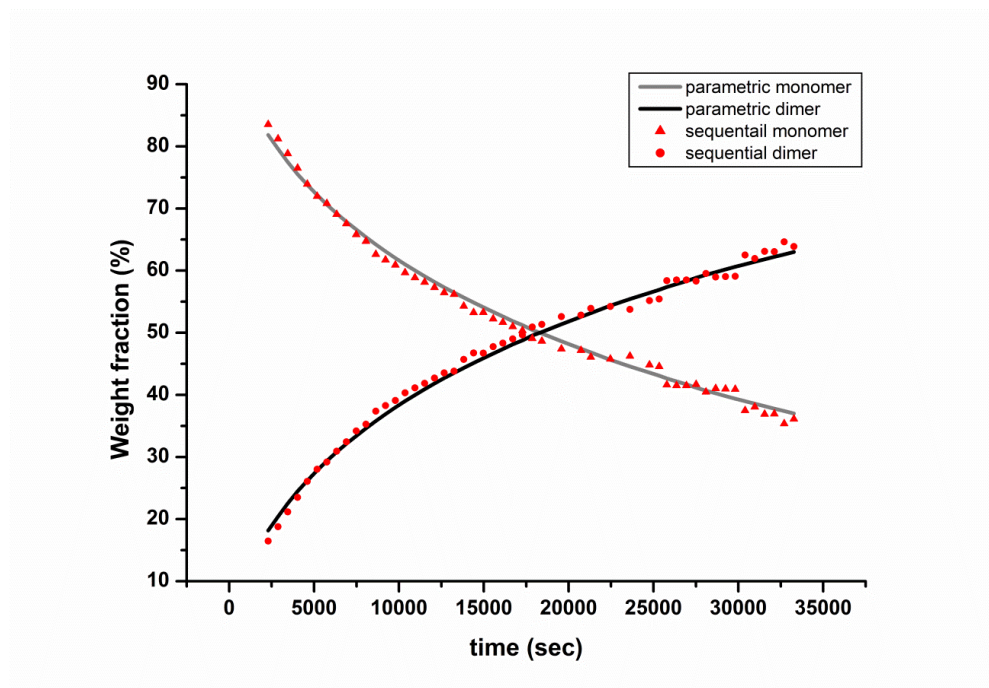
Figure 3.38: Comparison of the weight fraction of monomer and dimer phase of 9-methylanthracene in dependence on illumination time. Sequantially obtained values are given by symbols, while the parametric values are represented by a line.
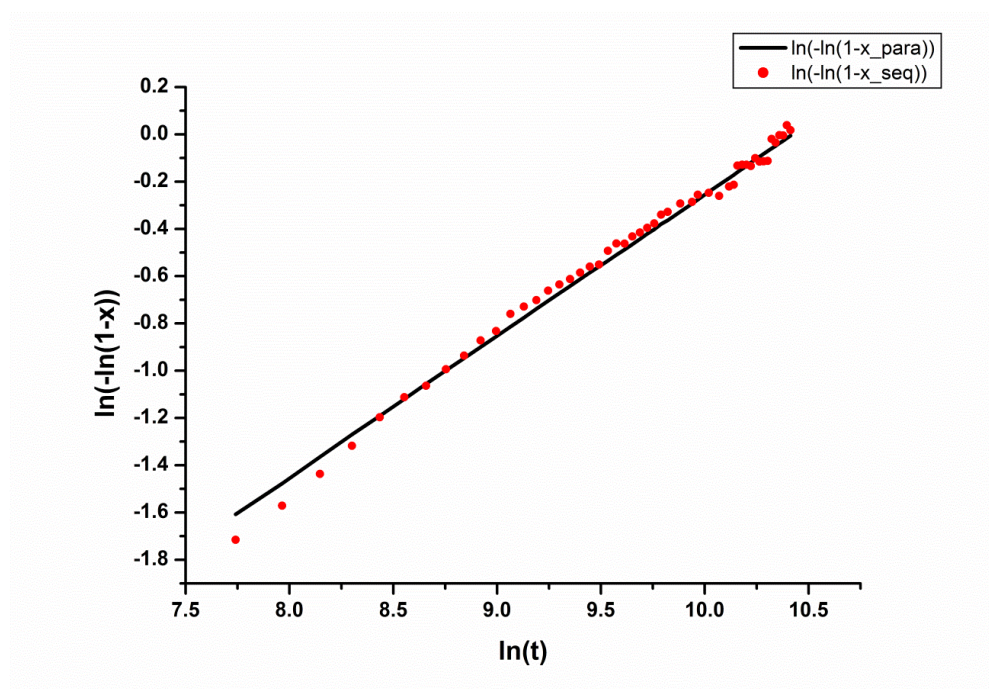
Figure 3.39: Comparison of the Sharp-Hancock plot of the values obtained for 9-methylanthracene dimerization in sequential (red dots) and parametric Rietveld refinement (black line).

Table 3.10 lists a comparison of Avrami constants n and reaction rate k as obtained from the parametric refinement results and using a fit of the Sharp-Hancock plot for the sequential refinement for 9-methylanthracene dimerization. The difference of the n values is within the experimental error.

Table 3.10: Comparison of Avrami constants n and k as obtained directly from the parametric refinement results of 9-methylanthracene dimerization and using a fit of the Sharp-Hancock plot for sequential refinement (Figure 3.39).

	n	k (s^{-1})
Parametric refinement	0.599(4)	$2.97(3) \times 10^{-5}$
Sequential refinement	0.618(7)	$3.02(5) \times 10^{-5}$

Based on the JMAK model the obtained results can be interpreted in the following way: the reaction is characterized by one-dimensional diffusion controlled growth with decreasing nucleation rate and heterogeneous nucleation. An Avrami parameter n smaller than one might indicate the nucleation rate is decreasing with the reaction time, which was reported in similar cases, for instance for photodimerization of α-trans-cinnamic acid (Bertmer *et al.*, 2006). In the case of one-dimensional diffusion-controlled reactions the Avrami exponent n can vary between 0.5 and 2.5, n is close to 0.5 for instantaneous nucleation and close to 2.5 if the nucleation rate is increasing (Christian, 1965).

Photodimerization often has a heterogeneous character of nucleation (Moré *et al.*, 2010). It was mentioned (Sperling, 1992) that the rather low values of n refer to heterogeneous nucleation, which can be explained as a result of nucleation at crystal defects. In addition, Wernick *et al.* (1988) & Takegoshi *et al.* (1998) showed that the dimerization of 9-substituted anthracene initiates at crystal defects sites and is not a homogenous process.

Based on that, the kinetics of 9-MA photodimerization reaction can be summarized as follows. The reaction starts by the absorption of light in the parent phase (monomer)

to initiate nucleation of the dimer phase. The required free energy for the nucleation process varies with different crystal locations and the ones possessing the least energy are the preferential sites. Once nuclei of the product phase are formed, the progress of the growth takes place, controlled by the rate at which the atoms diffuse into the parent phase. With ongoing illumination the nuclei of the dimer phase grow and consequently the fraction of the dimer phase increases while the fraction of the untransformed phase decreases.

3.5.5   Conclusion

A time resolved X-ray powder diffraction study on 9-methylanthracene was performed during $[4\pi + 4\pi]$ photodimerization, which is a typical example for a solid state photodimerization reaction, and was studied using single crystals before (Turowska-Tyrk & Trzop, 2003). The study overcomes the drawbacks of single crystals by the application of powder diffraction taking advantage of fast full quantitative parametric Rietveld refinement of bulk material using CCD area detectors and synchrotron light.

The JMAK model can give valuable information about phase transformations kinetics, which can be extracted directly from parametric Rietveld refinement with high accuracy.

The suggested kinetic model for 9-MA photodimerization comprises a heterogeneous decreasing nucleation which is followed by diffusion controlled growth (Mabied *et al.*, 2012).

4   X-ray diffraction analysis of nanocrystalline materials

Nanomaterials are characterised by their domain size, which is between 1 and 100 nm in at least one dimension (Rao *et al.*, 2004). The interesting feature of small nanoparticles is that their properties are different to the ones observed within bulk materials. Among these properties are electronic, optical, magnetic, and chemical characteristics (Rao *et al.*, 2004). The peculiarity of nanomaterials is that a large volume fraction of such a material is characterised by interfaces (e.g. grain boundaries).

The application of nanomaterials covers a wide range of which some examples are given in the following. In energy storage, their high surface area makes them a promising class of materials e.g. for hydrogen storage (Niemann *et al*., 2008). In construction industry, nanomaterials are used to create self-cleaning surfaces or enhance the structural strength of materials (Aegerter *et al.,* 2008; Lee *et al.*, 2010). Even in biology and medicine, nanomaterials are widely used, e.g. in tissue engineering where nanostructured features on top of joint prosthesis are used to enhance their biocompatibility (Salata, 2004).

Nanomaterials can be synthesized using two completely different approaches:

1) the top-down methods: by deconstructing bulk materials with the use of physical or chemical processes,

2) the bottom-up methods: by constructing nanomaterials from basic building units like atoms or molecules.

In order to characterise nanomaterials X-ray diffraction is particularly suited as it allows measuring a relatively large number of nanocrystals in short time. Other methods as e.g. electron microscopy are tedious and time consuming (Ungár & Gubicza, 2007).

Within the course of this work, the second method of synthesis, the bottom-up approach, was applied. Sol-gel methods were used to synthesise at least partially

crystalline nanoparticles. The influence of preparation conditions on the obtained material as well as on the nanocrystalline growth was studied.

In the following, some basic information about sol-gel synthesis and nanocrystalline growth kinetics are given. Furthermore the materials which were investigated are described.

4.1   Methodological background

4.1.1   Sol-gel preparation

Sol-gel processing is an important method in the synthesis of nanostructured materials and belongs to the bottom-up approaches (Schubert & Hüsing, 2012). The method is cheap and suited to synthesise a wide variety of materials, especially silicate materials and oxides, though other materials classes, e.g. sulphides, can be synthesised as well. Within the course of this work oxide and sulphide materials were prepared.

A sol is characterised by a stable suspension of colloidal solid particles within a liquid. In a gel a porous solid network of these particles is formed which is supported by the liquid phase. If the liquid is removed, a xerogel or an aerogel forms. Within a xerogel porosity is removed, causing shrinkage in volume, while in an aerogel the porous structure is kept (Schubert & Hüsing, 2012).

The sol-gel approach is characterised by a series of reactions which follow each other. In order to start the sol-gel process, hydrolysis of the reactants in the solvent is necessary. After that, condensation sets in. Condensation reactions either produce an alcohol or water (Schubert & Hüsing, 2012). After condensation took place, the sol-gel transition happens by aggregation of the sol particles. If the viscosity of the gel increases drastically, the process is called aging. The complete evaporation of the solvent is called drying and leads to the formation of an aerogel or a xerogel (Schubert & Hüsing, 2012).

In order to synthesise oxides materials using the sol-gel method inorganic (metal salts) or metal organic (alcoxide) precursors are used (Schubert & Hüsing, 2012). Throughout the course of this work CeO_2 was synthesised from Ce(IV)isopropoxide. The influence of preparation conditions on the properties of the obtained material were investigated using CeO_2 in form of a xerogel.

For sulphide preparation, in general, there are four different methods (Almeida & Xu, 2005):

1) sol-gel deposition from a solution of sulphides: the first attempts to use such an approach were already made by Chern & Lauks (1982), who report the deposition of amorphous chalcogenide thin films by spin-coating on glass and silicon wafers substrates,

2) sol-gel synthesis from organometallic precursors,

3) colloidal sol-gel synthesis from inorganic precursors,

4) preparation via the vulcanisation of oxide gels.

In the present thesis, the first method was used to synthesise Cu_2ZnSnS_4 powders and thin films. The investigated thin films were produced by dip-coating using glass and molybdenum coated glass as substrates.

4.1.2   Growth kinetics of nanocrystalline materials

The growth of nanocrystalline materials is a frequently studied phenomenon, as the properties of nanocrystalline materials are directly related to their size. Grain growth happens in order to minimise the energy within the system by reducing the total grain boundary energy (Malow & Koch, 1997).

Both isothermal and non-isothermal studies can be performed in order to study the growth kinetics of nanomaterials. Depending on the material properties, different growth behaviour is reported. Therefore a huge variety of models to describe the growth process can be found in literature.

4.1.2.1 Isothermal grain growth kinetics

The simplest model for isothermal growth kinetics is given by the model of Ostwald ripening (Ostwald, 1897). In this case, comparatively large grains grow at the expense of small grains, which are dissolved. The initial model for Ostwald ripening gives the average particle diameter D in dependence on the initial diameter D_0 and time t and can be written as follows:

$$D^3 - D_0{}^3 = kt .$$
(4.1)

Using a more generalised version of the equation (4.1), the average particle diameter D in dependence on time t can be calculated using the following equation:

$$D = kt^{\frac{1}{n}} + D_0$$
(4.2)

(with k: reaction rate ; t: time; n: exponent; D_0: average particle diameter at $t = 0$).

Depending on the exponent n different mechanism of growth are proposed. Different exponents n and their interpretation is given in Table 4.1.

Table 4.1: Values of n and related growth processes (Huang *et al.*, 2003):

n	process
2	growth controlled by diffusion along particle matrix boundary
3	growth controlled by volume diffusion
4	growth controlled by dissolution kinetics at particle matrix interface

Another process for nanocrystalline growth was proposed by Penn and Banfield (1998). They describe the attachment and therefore growth of crystals by a spontaneous self-organisation: two neighbouring crystals attach in a way that they share a common crystallographic orientation (Penn & Banfield, 1998). They called this process oriented attachment.

The process can be described mathematically using the following equation (Zhang *et al.*, 2010):

$$D = \frac{D_0(\sqrt[3]{2k_1 t} + 1)}{(k_1 t + 1)}.$$

(4.3)

Furthermore a combination of oriented attachment and Ostwald ripening can cause grain growth. In this case, a model using equations (4.2) and (4.3) would describe the evolution of the average domain size with time (Zhang *et al.*, 2007):

$$D = \frac{D_0(\sqrt[3]{2k_1 t} + 1)}{(k_1 t + 1)} + k_2 t^{\frac{1}{n}}.$$

(4.4)

Two different reaction rates k_1 and k_2 for both processes are necessary to describe the evolution of *D*. In order to give an impression of these different growth models and their evolution with time a comparison is plotted in Figure 4.1.
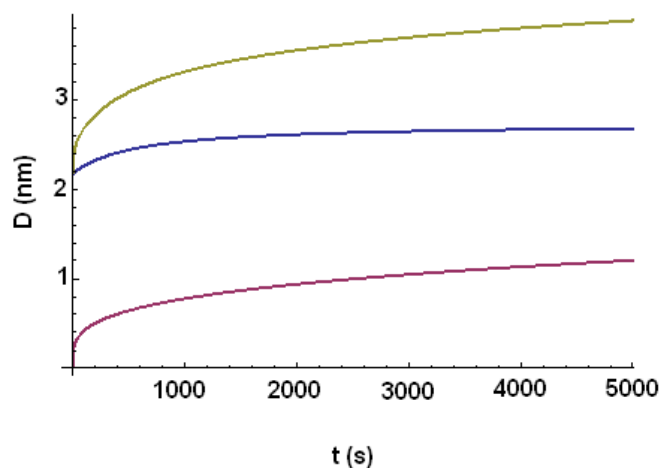
Figure 4.1: Grain growth (green line) modelled using a combination of Oriented Attachment (blue) and Ostwald ripening (red). Parameters used in modelling are: $D_0 = 2.167$ nm, $k_1 = 0.00182$, $k_2 = 0.11838$ and $n = 3.67$. Those values were obtained by modelling a real dataset.

In addition to the previously described models, uncommon growth behaviours can be observed e.g. linear growth (Krill *et al.*, 2001).

Furthermore growth kinetics can also be described using the JMAK equation (see chapter 3.5.3.1) (Nichtová *et al.*, 2009), though the equation is not applicable in all cases (Zhang & Banfield, 2002). Nevertheless, this method was applied to results obtained from Whole Powder Pattern Modelling throughout the course of this work after applicability was proven. Powder diffraction data was modelled using a lognormal distribution *g(D)* with lognormal mean *μ* and standard deviation *σ* of spherical crystalline domains. The spherical particle shape was chosen because in no case any indication of a preferred particle shape (cube, octahedron,…) was given, so that a sphere might be a good approximation for such particles. In this case, the distribution of domains is given by the following equation:

$$g(D) = \frac{1}{D\sigma\sqrt{2\pi}} \exp\left[-\frac{1}{2}\left(\frac{\ln D - \mu}{\sigma} \right)^2 \right].$$
(4.5)

The changes of the mean *μ* and the standard deviation *σ* with time were investigated throughout an isothermal measurement series. The mean volume *<V>* of the domains can be calculated from the third order moment of the size distribution using *μ* and *σ* as given:

$$\langle V \rangle = \frac{\pi}{6} \exp\left[3\mu + \frac{9}{2}\sigma^2 \right].$$
(4.6)

The kinetics of the domain growth reaction is investigated using a JMAK type equation for the change in average volume (denoted as volume growth rate *a(vol)*) (Scardi *et al.*, 2010). In addition to the mean volume *<V(t)>* at time *t*, the initial mean volume *<V(0)>* and the final mean volume *<V(∞)>* need to be known:

$$\frac{\langle V(t) \rangle - \langle V(0) \rangle}{\langle V(\infty) \rangle - \langle V(0) \rangle} = a(vol) = 1 - \exp(-(kt)^n).$$
(4.7)

Using an Avrami type equation relative changes of the domain size are considered while using the previous equations the actual size is considered.

For all growth models the activation energy of growth processes can be derived from measurement series performed at different temperatures using the Arrhenius equation.

$$k = Ae^{-\frac{E}{RT}} \qquad \text{Arrhenius equation.} \qquad (4.8)$$

In this equation E is the activation energy, R is the ideal gas constant, T is the temperature, k is the rate constant and A is a frequency factor.

4.1.2.2 Non-isothermal growth

The JMAK equation can also be applied to non-isothermal measurements if the measurements are performed with constant heating rate ψ (isochronal). In this case, the following equation is obtained (Matusita *et al*., 1984):

$$\ln(-\ln(1-x)) = -n\ln\psi - 1.052\frac{nE}{RT} + const. \qquad (4.9)$$

Within this equation x denotes the relative change of the mean domain size, n the Avrami parameter, E the activation energy, R is the ideal gas constant, and T is the temperature.

Šatava (Šatava, 1971) described a method to extract data from isochronal thermogravimetric data. Using the equation derived by Matusita *et al.* and Šatava's assumptions for data with constant heating rate ψ, the following equation is valid:

$$\left.\frac{d\ln(-\ln(1-x))}{dT^{-1}}\right|_{\psi} = -1.052\frac{nE}{R} . \qquad (4.10)$$

With this equation it is possible to analyse a single set of measurement by plotting $\ln(-\ln(1-x))$ versus T^{-1}. The slope of the resulting straight line is equal to $-1.052 n E/R$.

If data of different sets of measurements with different heating rates are available, a relation which was originally derived by Ozawa (1970) can be used:

$$\left. \frac{d\left(\ln(-\ln(1-x))\right)}{d\ln(\psi)} \right|_{T} = -n \, . \tag{4.11}$$

By plotting $\ln(-\ln(1-x))$ versus $\ln(\psi)$ for a specific temperature T, a straight line with slope $-n$ is obtained.

4.2   Investigated materials

4.2.1   CeO$_2$

Nanostructured cerium(IV)oxide CeO_2 (ceria) is widely investigated due to its properties. Of special interest are the catalytic properties which are given by nanosized ceria. Among the applications of nanocrystalline ceria are solid oxide fuel cells, oxygen sensors, oxygen permeation membranes and due to its biocompatibility, even biomedical application (Sun *et al.*, 2012).

4.2.1.1   The crystal structure of CeO$_2$

Ceria crystallises in the fluorite structure type in space group $Fm\overline{3}m$. There is no phase transition reported up to temperatures of 1497°C, which corresponds to the melting temperature of the compound (Yashima *et al.*, 2006). Nevertheless structural disorder of the oxygen position at temperatures above 700°C was reported (Yashima *et al.*, 2006).

The structure of ceria is characterised by a cubic close packing of cerium with oxygen occupying the tetrahedral voids. In Figure 4.2 the crystal structure is shown. Within the structure each cerium atom is coordinated by four oxygen atoms, which are placed at equal distances.
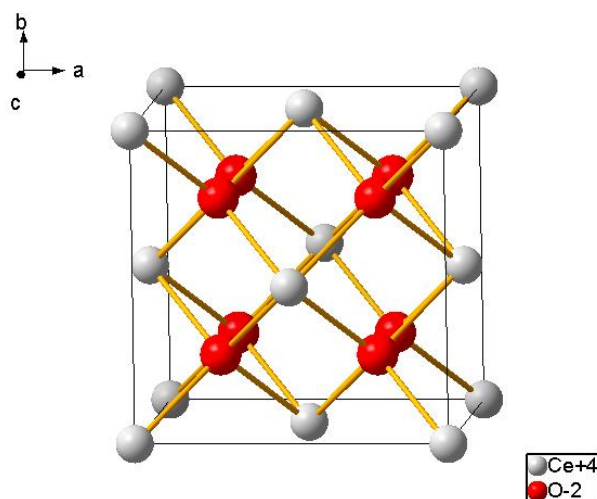
Figure 4.2: Crystal structure of CeO_2.

Ceria is an n-type semiconductor and characterised by its oxygen deficiency, which leads to an excess of metal. In order to preserve the neutral character, the two additional electrons caused by each oxygen vacancy need to be accommodated within the structure. The simplest solution is given by reducing Ce^{4+} to Ce^{3+}. Therefore ceria frequently does not possess the composition CeO_2 and the actual chemical composition changes to CeO_{2-x} (Han, 2012).

Within nanocrystalline CeO_2, a remarkable increase of the lattice parameters with decreasing domain size is reported (Tsunekawa *et al.*, 1999). This increase of the lattice parameter is also attributed to the change of the valence state of cerium (Tsunekawa *et al.*, 1999) which also indicates that the defect density within smaller nanoparticles is higher than in larger ones (Zhou & Huebner, 2001).

4.2.2 Cu_2ZnSnS_4 (CZTS)

Cu_2ZnSnS_4 (CZTS) is a semiconductor and currently investigated as a possible absorber layer within thin film solar cells. One reason for that is that CZTS is abundant and nontoxic and, even more important, its properties are excellent for application. CZTS has a direct band gap of about 1.5 eV, which is close to the ideal value of 1.34 eV according to the Shockley-Queisser limit (Shockley & Queisser, 1961), which relates the band gap energy to the theoretical maximum of the efficiency ($\approx$ 33%) of a solar cell. Furthermore CZTS possesses an absorption coefficient $\alpha >$ $10^4 cm^{-1}$.

4.2.2.1   The crystal structure of CZTS

The structure of CZTS is closely related to the structure of other sulphides like ZnS. A common feature of many of these structures is that the atoms are coordinated in tetrahedral configuration. Those structures can be related to the diamond structure and are therefore called "adamantine" structures. For CZTS different crystal structures have been proposed in literature, which vary in the positions of the cations (Cu, Zn, Sn) (Chen *et al*., 2009). So far, the kesterite and the stannite structure have been reported for CZTS. These structures both can be described as a cubic closed packing of S^- anions with one half of the tetrahedral voids occupied with cations. Depending on cation positions, the space group changes (Chen *et al*., 2009). Both, the kesterite and the stannite structures, can be derived from the cubic sphalerite structure (α-ZnS) by doubling the volume of the unit cell to a tetragonal structure (Vaughan & Tossell, 1980). A comparison of the structures is given in Figure 4.3. In the kesterite structure a partial or complete disorder of Cu and Zn atoms in the (001) layer might occur (Schorr *et al.*, 2007). The completely disordered kersterite shows also $I\bar{4}2m$ crystal symmetry. In this case, Cu^{2+} and Zn^+ occupy the Wyckoff position $4d$ (0,½,¼) randomly (Schorr *et al.*, 2007). Given the fact, that Cu^{2+} and Zn^+ have the same number of electrons and therefore an equal atomic form factor, they cannot be distinguished by conventional X-ray diffraction; a confusion of the stannite structure with the disordered kesterite structure cannot be excluded.
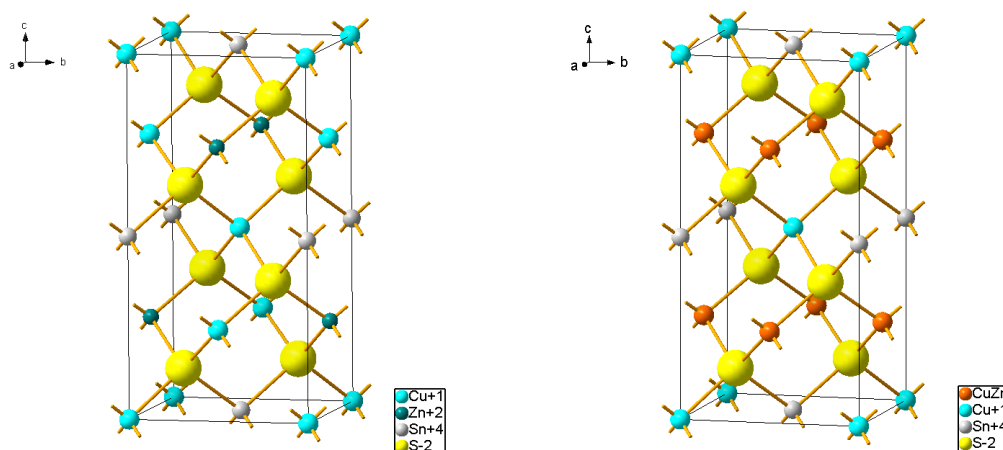
Figure 4.3: Comparison of the kesterite (space group $I\bar{4}$) (left) and stannite (space group $I\bar{4}2m$) (right) crystal structure proposed for CZTS.

Between temperatures of 866°C to 883°C the tetragonal kesterite undergoes a first-order phase transition to a cubic sphalerite structure with S at (¼,¼,¼) and the cations at (0,0,0) (occupancy: 0.5 Cu + 0.25 Zn + 0.25 Sn) (Schorr & Gonzales-Aviles, 2009).

4.2.2.2   Preparation of CZTS

In general, there are two different ways to produce CZTS thin films: using physical vapour deposition methods or chemical preparation.

For physical vapour deposition a gaseous phase of the materials which should be deposited is produced. This gaseous phase is directed through vacuum, a low pressure gas phase or a plasma to the substrate where it condensates. The thickness of a thin film deposited using physical vapour deposition methods varies from a few to thousands of nanometres (Mattox, 1998). Depending on the source of the gaseous phase different methods are distinguished. CZTS can be prepared from metallic phases (Cu, Zn, Sn) or from sulphides (CuS, ZnS, SnS). After deposition of those

layers a heat treatment in combination with a sulfurization in sulphur or H_2S atmosphere is applied to form CZTS (Delbos, 2012).

For chemical preparations, there are two different approaches: deposition of a thin film containing sulphur or sulfurization of the thin film during an annealing step. The first chemical preparation of CZTS was performed in 1996 by Nakayama and Ito using spray pyrolysis. For spray pyrolysis, metal containing solutions are sprayed onto a hot substrate and react there to the final product. Additionally, the reaction can be improved by means of thermal treatment. Temperature and duration of the thermal treatment vary from 290°C (Kishore Kumar *et al.*, 2009) to 550°C (Nakayama & Ito, 1996) and from 0.5 h (Kamoun *et al.*, 2007) to 2h (Nakayama & Ito, 1996).

Another method to obtain a CZTS thin film chemically is using a sol-gel based approach. Possible sources for metal cations are chlorides, iodides or acetates. The obtained sol can be applied to the substrate in different ways, e. g using spin or dip coating. The first preparation is reported by Tanaka *et al*. (2007). They spin coated a metal containing sol onto a substrate for subsequent sulfurization at high temperatures. Later approaches (Yeh *et al.*, 2009; Fischereder *et al.*, 2010) included sulphur in form of thiourea or thioacetamide in the sol. A further solution based preparation method is photo-chemical deposition (Moriya *et al.,* 2006). Here the sulphur source is $Na_2S_2O_3$. An illumination with ultraviolet (UV) light causes a dissociation of $S_2O_3^{2-}$ and a release of electrons, which react with metal cations to sulphides. After deposition the films are annealed at temperatures between 300 and 500°C (Moriya *et al.*, 2006).

A recent preparation method of a CZTS absorber layers is the production of nanocrystalline CZTS, which can be deposited on a suitable substrate. The CZTS layer itself is obtained by the CZTS nanoparticles plus a binder, which immobilises the particles. This is done using various chemical approaches (Todorov *et al*., 2009; Chory *et al*., 2010; Kameyama *et al.*, 2010).

4.3 Influence of preparation conditions on CeO₂ xerogels defect density

The work presented in this chapter was published in: Melanie Müller, Matteo Leoni, Rosa Di Maggio and Paolo Scardi: *Defects in nanocrystalline ceria xerogel*. Zeitschrift für Kristallographie Proceedings (2011) 1, 81-86.

Rosa Di Maggio helped with sample synthesis and the interpretation of the reaction occurring during sample synthesis. Mirco D'Incau, Ken Beyerlein and Luca Gelisio helped in data collection and Matteo Leoni with data analysis.

4.3.1 Introduction

Most properties of nanocrystalline systems are related to the shape and size distribution of the domains. Those, in turn, are strongly dependent on the preparation method and on kinetic conditions of the growth process (Müller *et al.*, 2011b).

Nanocrystalline ceria was produced via a sol-gel approach from Ce alkoxides with and without the addition of water and a chelating agent (acetylacetone). Microstructure analysis of the resulting powder was performed using laboratory and synchrotron X-ray powder diffraction. The data was analysed using WPPM. It is shown that the synthesis with water leads to smaller and more defective particles and that aggregation of the crystalline domains occurs at temperatures as low as 80°C. The route to the formation of the ceria nanograins is explained in terms of balance of competing condensation reactions (Müller *et al.*, 2011b).

4.3.2 Experimental

4.3.2.1 Sample preparation

In addition to a previously known preparation using the chelating agent acetylacetone in isopropyl alcohol (Leoni *et al.*, 2004 ; Scardi *et al.*, 2010) a new approach for sol-gel synthesis using isopropyl alcohol with eventual adding of water was utilised.

In general, the preparation starts from a solution of 5 g of Ce(IV)isopropoxide (Gelest ABCR, 80 % cerium isopropoxide, 20 % isopropyl alcohol) in 20 ml of isopropyl alcohol (2-propanol Carlo Erba RPH 99.5 %, $H_2O \leq 0.5\%$):

1) a first specimen (named CE) was produced from the pure solution,

2) the second by adding 2.41 ml of distilled water to the solution (specimen CEW),

3) and the third by addition of 0.67 ml of acetylacetone (2,4-pentanedione, Carlo Erba RPE 99 %, $H_2O \approx 0.2\%$) (specimen CEacac) to the solution.

All solutions were boiled under reflux for 24 h. In order to produce a xerogel powder, the specimens were left in a rotary evaporator at 40°C for 2 h to extract the solvent and subsequently dried in air at 80°C for 16 h.

The properties of the newly synthesised samples were compared to properties obtained from a sample which was synthesised previously (CeOLD) (Scardi & Leoni, 2006). In this case, the same preparation was performed as for CEacac.

4.3.2.2   Measurements

X-ray powder diffraction data were collected on a laboratory Rigaku PMG-VH horizontal diffractometer with CuK_α radiation. The setup of the machine includes primary and secondary Soller slits with an angular aperture of 2° and analyser to guarantee a narrow and symmetrical instrumental profile down to ca. 15° 2θ. Patterns were collected in the 18 - 100° 2θ range with a step of 0.05° and a counting time of 30 seconds per point.

Synchrotron radiation powder diffraction data were recorded on the MCX beamline at the ELETTRA synchrotron (Trieste, Italy) using a wavelength of 0.9991 Å calibrated with the NIST SRM 640a silicon standard. A flat-plate setup and an analyser were employed. Data were collected in the 8 - 82° 2θ range with a step of 0.05° and a total counting time of 20 seconds per point.

The instrumental contribution to the recorded powder diffraction pattern was determined from measurements of a lanthanum hexaboride standard (NIST SRM 660a; LaB_6) for both instruments.

4.3.3   Results and discussion

The recorded powder diffraction data were analysed by WPPM (Scardi & Leoni, 2002) using the PM2K software (Leoni *et al.*, 2006). For modelling, particles were assumed to be spherical, with a lognormal distribution of diameters. Additionally lattice distortions were effectively considered in the form of dislocations on the primary $\frac{1}{2}\{111\}<1\bar{1}0>$ slip system of ceria. The dislocation contrast factor was calculated using the procedure proposed by Martinez-Garcia *et al.* (2009). For each specimen, the same set of parameters was simultaneously refined using both laboratory and synchrotron powder diffraction patterns (Müller *et al.*, 2011b).

The results of the modelling are shown in Figure 4.4 to Figure 4.6. In all plots the measured data are compared with the result from the modelling. Furthermore, the difference curves are shown, indicating that the quality of the modelling is decent for all specimens, as already observed in ceria (Leoni *et al.*, 2004; Scardi *et al.*, 2010).
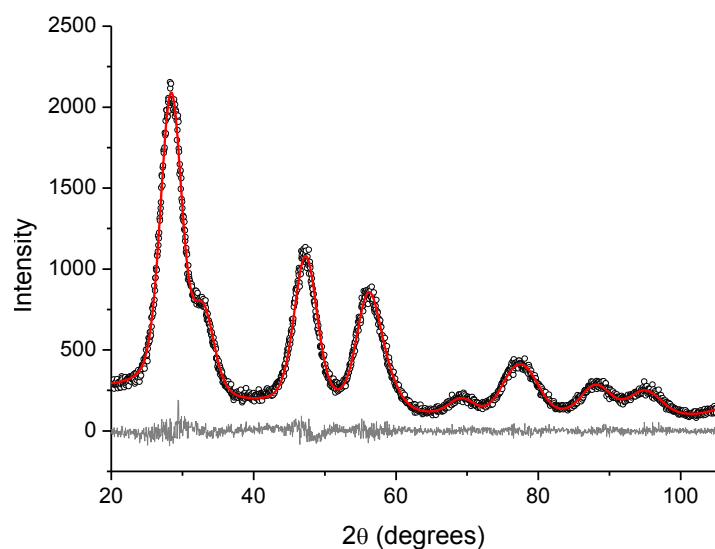
Figure 4.4: WPPM of laboratory ($\lambda = 1.5406$ Å) powder diffraction patterns obtained for specimen CEacac of CeO_2. Measured data (points), modelled pattern (red line) and difference curve (grey line) are shown.
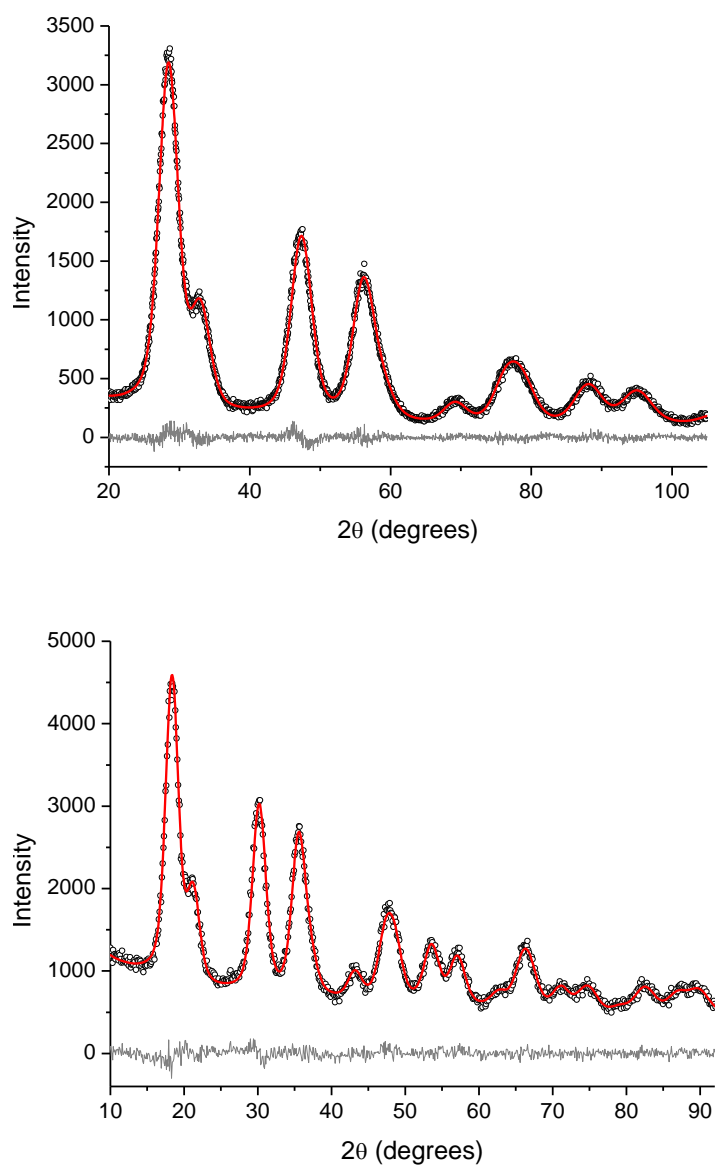
Figure 4.5: WPPM modelling of laboratory ($\lambda = 1.5406$ Å) (top) and synchrotron ($\lambda = 0.9991$ Å) (bottom) powder diffraction patterns obtained for specimen CE of CeO_2. Measured data (points), modelled pattern (red line) and difference curve (grey line) are shown.
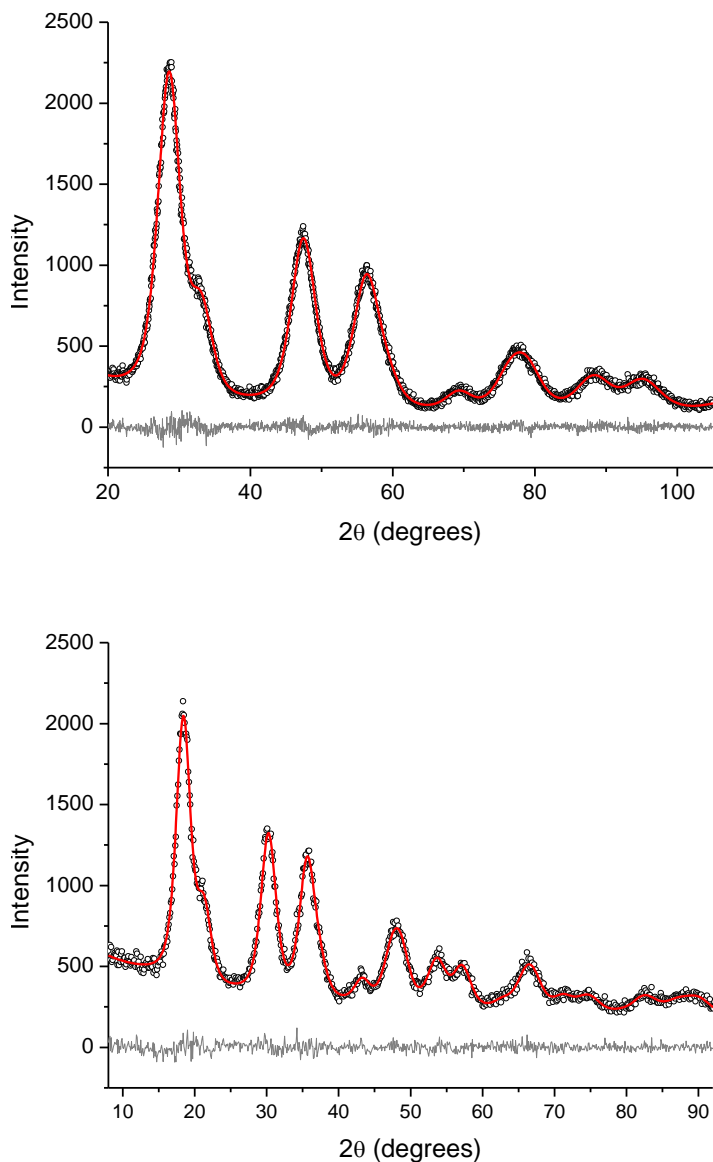
Figure 4.6: WPPM modelling of laboratory ($\lambda = 1.5406$ Å) (top) and synchrotron ($\lambda = 0.9991$ Å) (bottom) powder diffraction patterns obtained for specimen CEW of CeO_2. Measured data (points), modelled pattern (red line) and difference curve (grey line) are shown.

The key parameters which were obtained in modelling are reported in Table 4.2. A slight variation of lattice parameters is observed. Moreover, the dislocation density and average domain size depend on the preparation conditions. A more detailed view

on the domain size distribution is given in Figure 4.7, showing the distributions obtained for all samples in comparison with the one previously obtained for ceria (CEOLD), which was published by Scardi & Leoni, 2006.

Table 4.2: Results of WPPM on ceria samples: lattice parameter a_0, mean domain size $<D>$, variance of the lognormal distribution, dislocation density ρ, effective outer cut-off radius R_e. Additionally a comparison with literature data (CEOLD) (taken from Scardi & Leoni, 2006) is proposed.

Specimen		CEOLD	CEacac	CE	CEW
a_0	(nm)	0.543809(8)	0.543296(8)	0.543313(7)	0.54296(9)
$<D>$	(nm)	2.28(2)	2.19(3)	2.34(2)	1.78(3)
Variance	(nm)	0.22(1)	0.33(1)	0.43(1)	0.40(2)
ρ	(10^{16} m^{-2})	0.1(1)	1.6(5)	1.4(2)	3.0(6)
R_e	(nm)	4.3(6)	2.5(4)	2.5(5)	2.7(4)
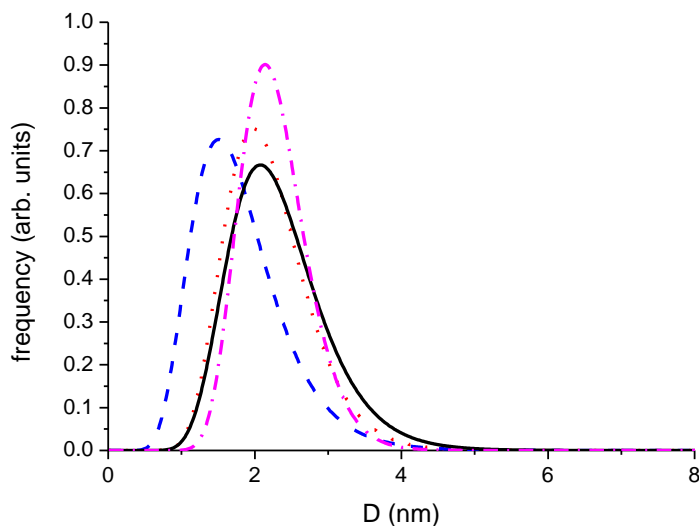
Figure 4.7: Comparison of the domain size distributions obtained from modelling using PM2K for specimens CE (black line), CEW (blue dash), CEacac (red dot) and CEOLD (pink dash-dot).

Independently of the preparation, all distributions obtained from newly prepared samples are wider than the one of CEOLD. One difference in preparation is that CEOLD was just heat treated in the vacuum evaporator and did not undergo the subsequent heat treatment at 80°C. This indicates that even the bland treatment at 80°C applied to the ceria powders analysed here is thus sufficient to start aggregation of the domains and widen the distribution (Müller *et al.*, 2011b).

A further confirmation of the beginning of particle agglomeration is also given by the defect content which is observed within the powders. The observed dislocation density is higher in comparison with the one obtained from CeOLD. A higher dislocation density can be explained by particle agglomeration. As pointed out by Scardi *et al.* (2010) aggregations of domains in a xerogel may occur by small movements of the domains, without any diffusion. Local steps on the surface therefore may be trapped in the larger grain in the form of an edge dislocation (Scardi *et al*., 2010) which leads to a higher defect density.

The quantity of dislocations in the CEacac specimen is compatible with the literature data on heat treated xerogels as published by Leoni *et al.* in 2004. A plot (Figure 4.8) containing the new values in addition to the previously published data (Leoni *et al*., 2004) shows a good agreement between the results. The dislocation density observed for the CEacac specimen follows a trend line of a set of analogous specimens heat treated at higher temperatures (Leoni *et al*., 2004) as well as the variance of the domain size distribution, which correlates well with the one reported in literature data at increasing temperature (see Figure 4.8) (Leoni *et al*., 2004).
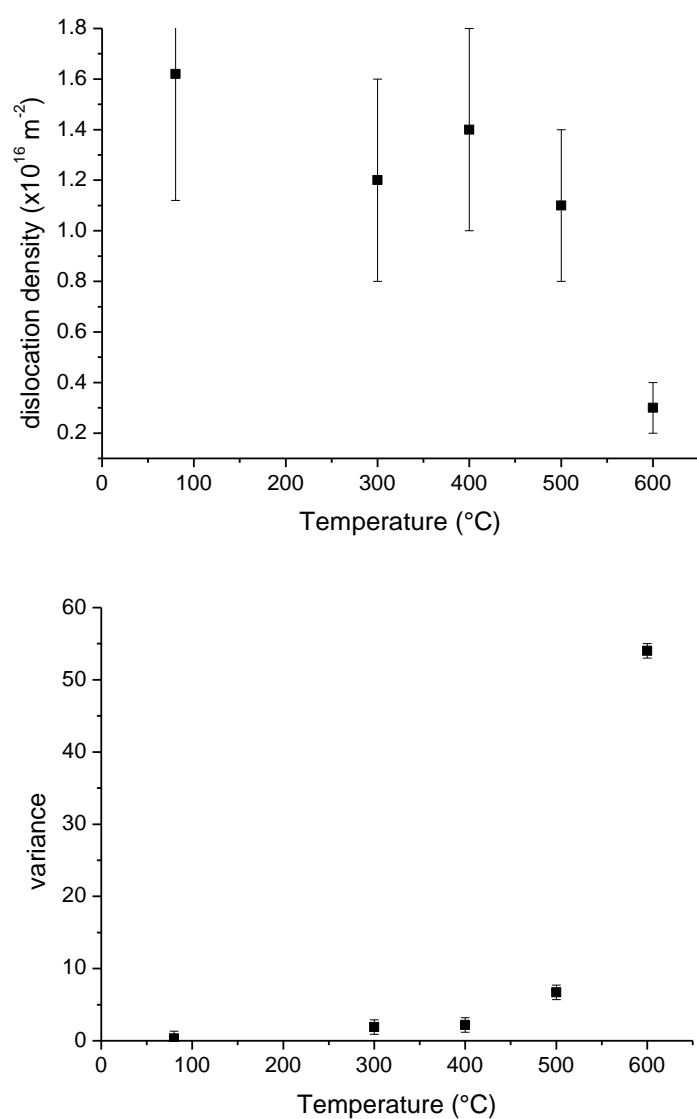
Figure 4.8: Trend of dislocation density (top) and variance of the distribution (bottom) for CEacac samples versus the temperature of heat treatment. All data at 80°C are from the present work; while the data at increasing temperature is taken from a previous preparation and was published before by Leoni *et al.* (2004).

As stated previously, the lattice parameter of nanocrystalline ceria is influenced by the chemical composition. Depending on the oxygen species (peroxide O_2^{2-} or superoxid O_2^{-}) formed on the surface of a particle, different models have been proposed to describe the relation of lattice parameter, domain size and oxygen content

(Tsunekawa *et al.*, 1999). A comparison of these models and values obtained for the present samples is shown in Figure 4.9.
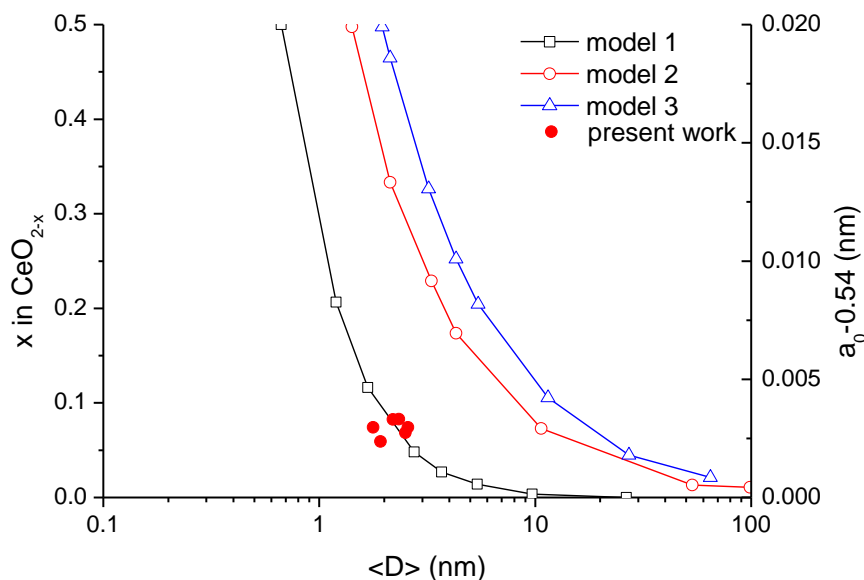
Figure 4.9: Stoichiometry of CeO_2 and variation in lattice constant with respect to 0.54 nm. The different models are taken from Tsunekawa *et al.* (1999).

In Figure 4.9, it can be seen that the present synthesis is best described using model 1 from Tsunekawa *et al.* (1999), suggesting that peroxide $2 O_2^{2-}$ species are present on the surface of the nanoparticles. This assumption is surely fulfilled as the work was performed in low acidity conditions and resonant oxygen bonds are expected on the surface of the particles (coming either from coupled acac oxygens or vicinal hydroxyls). The resulting estimated stoichiometry of the powder is $CeO_{1.92}$, not far from the ideal 1:2 ratio (Müller *et al.*, 2011b).

Another remarkable aspect is given by the fact that the domains size distribution and the mean domain size of sample CEW are clearly shifted to smaller values with respect to the values obtained from other preparations (see Figure 4.7).

It is known, that Ce(IV)isopropoxide ($Ce(OPr^i)_4$) in isopropyl alcohol forms mainly ($Ce_2(OPr^i)_8 \cdot 2HOPr^i$) dimers (Ribot *et al.*, 1991), with trimers and monomers also being possible. In general, hydrolysis goes to almost completion when a sufficient amount of water is added, though it is partial when only moisture of air is present. The structure and the size of condensed products depend on the relative rates of the three reactions which occur during condensation:

M–OR + M–OH → M–O–M + R–OH   Alcolation   (4.12)

M–OH + M–OH → M–O–M + H–OH   Oxolation   (4.13)

M–OX + M–(OH$_2$) → M–O(X)–M + H$_2$O   Olation   (4.14)
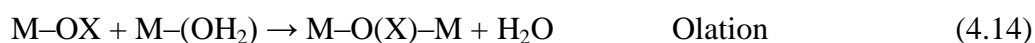
When hydrolysis is promoted (e.g. by the addition of water), oxolation is competitive with alcolation and highly condensed products are favoured: oxo-hydroxides form by aggregation of much smaller oligomeric building blocks, wrapped in OH groups, which act as spacers. Further condensation can take place when materials are treated thermally at higher temperature.

When hydrolysis is carefully reduced (e.g. only moisture of air present), the most likely condensation reaction between partially hydrolysed and coordinatively saturated ceria precursors seems to be alcolation, which releases isopropanol and results in oxo-alkoxide products. Cerium acquires its maximum coordination number also via olation, which is even favoured because of its size. The oxo-alkoxide products are still able to condense again, resulting in more extended and less branched polymers (Müller *et al.*, 2011b).

Therefore the water content of the solution is crucial for the formation of ceria and influenced the domain size. Smaller domains are expected if a large quantity of water is present.

4.3.4   Conclusions

A set of ceria specimens was produced using a sol-gel approach from cerium isopropoxide with and without the addition of water and of acetylacetone as chelating agent. X-ray line profile analysis evidenced the nanocrystalline nature of the obtained material. A rather large quantity of defects can be attributed to a heat treatment applied to the present specimens to guarantee the removal of all solvent. That treatment was sufficient to start agglomeration and thus incorporation of defects in the growing domains. The addition of water instead of the chelant acetylacetone favours the formation of smaller domains.

4.4 Kinetic study of isothermal CeO$_2$ growth

Parts of the work presented in this chapter were published in: Paolo Scardi, Matteo Leoni, Melanie Müller and Rosa Di Maggio: *In-situ size-strain analysis of nanocrystalline ceria growth*. Materials Science and Engineering: A (2010) 528(1), 77-82.

Sample synthesis and synchrotron measurements were performed by Rosa Di Maggio, Matteo Leoni and Paulo Scardi.

4.4.1   Introduction

The growth kinetics of sol-gel prepared nanocrystalline ceria was studied using X-ray line profile analysis. Therefore isothermal temperature dependent *in-situ* powder diffraction data were measured at the European Synchrotron Research Facility (ESRF). Data were modelled using a lognormal distribution of domain sizes with spherical shape. The results of modelling indicated that the growth of ceria can be treated using an Avrami type equation, therefore an interpretation of the growth process using that approach was performed. Other models of nanocrystalline growth were tested as well.

4.4.2   Experimental

The investigated sample was synthesised using the previously described approach from cerium isopropoxide in isopropanol with addition of the chelating agent acetylacetone (see chapter 4.3.2.1).

For powder diffraction measurements the obtained xerogel was ground and sealed into borosilicate glass capillaries (0.3 mm in diameter). The measurements were performed at the beamline ID31 of the ESRF using Debye-Scherrer geometry and radiation of a wavelength of 0.6325 Å. A hot air blower was used to heat the sample. Isothermal studies were performed at temperatures of 300°C, 350°C and 400°C. In

order to reach the desired temperature, a fast ramping with a rate of 40 K/min was performed at the beginning of the heating process.

4.4.3   Results

The X-ray powder diffraction patterns obtained for ceria at ambient condition show that the materials is at least partially crystalline. With increasing time at high temperature peaks are getting sharper indicating domain growth within the sample (Scardi *et al*., 2010). For data analysis WPPM (Scardi and Leoni, 2002) was applied using the PM2K software (Leoni *et al*., 2006). Modelling of the powder diffraction patterns included a lognormal distribution of spherical domains and lattice distortions in form of dislocations (Scardi *et al*., 2010).

Initially the growth kinetic of ceria was analysed using the Avrami equation as given in equation (4.7) (Scardi *et al.*, 2010). Therefore the mean domain volume was determined and the obtained volume growth rate *a(vol)* was fitted. Within this analysis an Avrami parameter *n* of 0.5 was obtained. Such a value can suggest an instantaneous nucleation (Kim, 2005) or the presence of a finite number of nucleation sites (Grundy *et al*., 1987). In this case, the most plausible explanation is the decomposition of the acetylacetonato chelating groups (Di Maggio *et al.*, 1998), leaving OH groups on the surfaces that could weld by condensation. According to this description, the JMAK exponent of about 0.5 may suggest that a finite number of reaction points is active, as expected owing to the finite number of acetylacetonato chelants on the outer surface of the domains (Scardi *et al*., 2010).

This explanation can also be taken into account if one considers the mechanism of oriented attachment. Therefore the data was reinvestigated using the previously introduced models of nanocrystalline grain growth. One of the main differences in data analysis using these models is that the actual average domain size and not the mean volume are taken into account.

In the following all three measurement series are modelled using the different growth models presented in chapter 4.1.2.1. Therefore the average domain size $<D>$ was fitted using the different models: generalised Ostwald ripening, oriented attachment and their combination. In addition, the Avrami equation (4.7) for the volume growth rate $a(vol)$ was used. An overview of the results of all measurement series is given in Table 4.3. The corresponding fits are shown in Figure 4.10.

Table 4.3: Results obtained by fitting of isothermal ceria data using four different models.

model	parameter	300°C	350°C	400°C
Ostwald ripening	D_0 (nm)	2.18	2.18	2.18
	k (s^{-1})	0.027(1)	0.11(2)	0.16(4)
	n	2.9(3)	3.9(3)	3.6(4)
Oriented attachment	D_0 (nm)	2.28(6)	2.72(7)	2.97(14)
	k (h^{-1})	2.1(13)	1.3(8)	4(5)
Combined	D_0 (nm)	2.04(9)	2.05(9)	2.2(1)
	k_1 (s^{-1})	0.001(1)	0.002(1)	0.002(6)
	n	3(2)	3.3(7)	4(3)
	k_2 (s^{-1})	0.02(6)	0.05(4)	0.1(3)
Avrami	n	0.68(6)	0.67(4)	0.75(6)
	k (s^{-1})	0.0002(1)	0.0004(1)	0.0009(1)

From the plots (see Figure 4.10), it is clearly seen that not all different models are suited to model the data, e.g. oriented attachment cannot satisfactorily model the dataset measured at 400°C. This is also seen in the obtained parameters (see Table 4.3). Especially parameters obtained from fitting data using oriented attachment or the combined model exhibit rather large esd's.
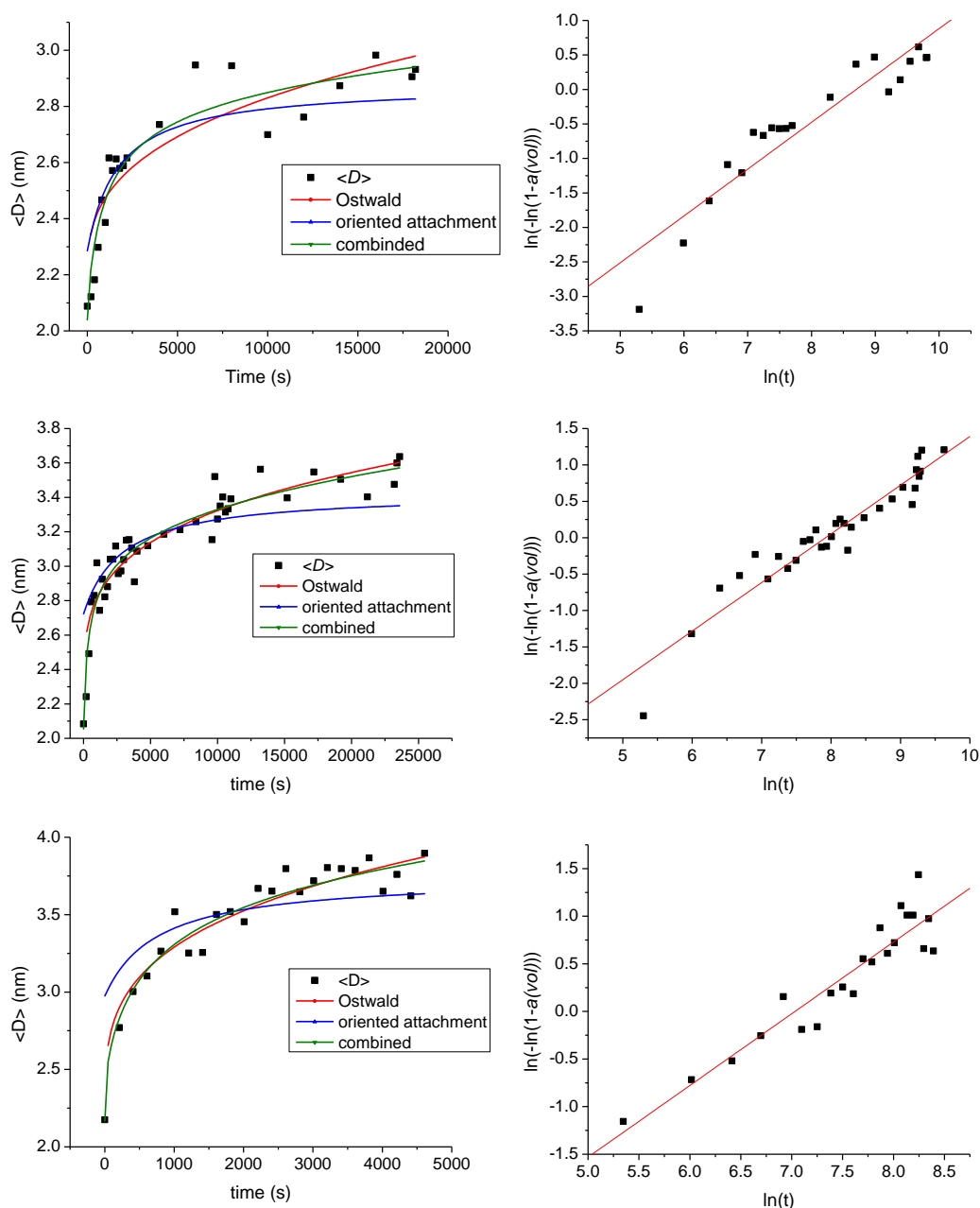
Figure 4.10: Left: Evolution of the average domain size *<D>* of ceria in dependence on time for an isothermal measurement. The data were fitted using three different models: Ostwald ripening (red), oriented attachment (blue) and the combined model (green). The corresponding fitting lines are plotted. Right: Sharp-Hancock plot of the same data series using the volume growth rate *a(vol)*. Measurements were performed at 300°C (top), 350°C (middle) and 400°C (bottom).

The values obtained for the growth exponent n in case of Ostwald ripening are between 3 and 4. Such values are generally interpreted as growth controlled by volume diffusion ($n = 3$) or growth controlled by dissolution at the particle matrix interface ($n = 4$). The latter can be correlated to the explanation obtained using an Avrami exponent $n \approx 0.5$, where the growth process is explained by decomposition of the acetylacetonato chelating groups to OH groups which cause condensation.

The activation energy for the growth process using the different models was determined by the Arrhenius equation. The Arrhenius plots of the different models are given in Figure 4.11. The calculated activation energies are reported in Table 4.4.

Table 4.4: Activation energies of ceria growth derived from the Arrhenius plots using the reaction rates determined using the four different models (oriented attachment (OA); Ostwald ripening (OW)).

model	slope	E (kJmol^{-1})
Ostwald ripening	-9(1)	74(9)
oriented attachment	-3(2)	24(24)
combined: OA	-4(2)	29(12)
combined: OW	-7.8(1)	65(1)
Avrami	-6.7(6)	56(5)
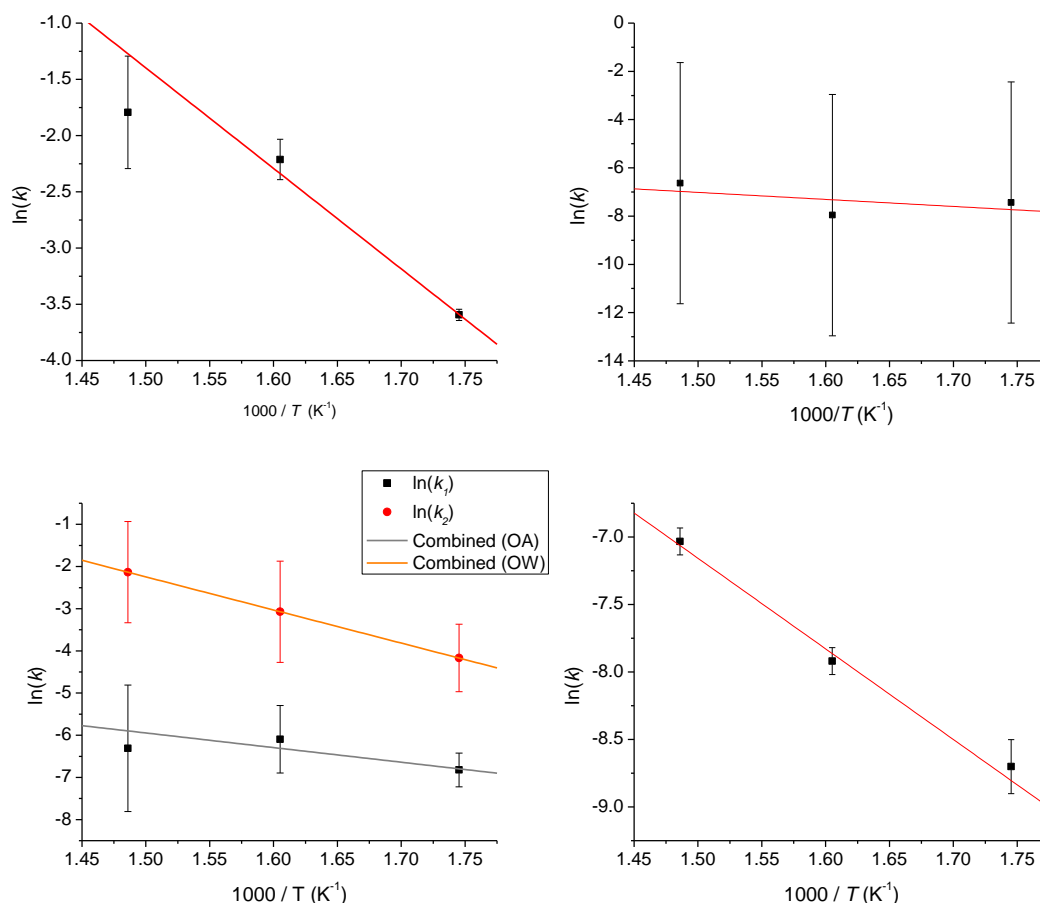
Figure 4.11: Arrhenius plots obtained for ceria growth using the reaction rates determined using the four different models: Ostwald ripening (top left), oriented attachment (top right), combined model (bottom left; black: oriented attachment (OA); red: Ostwald ripening (OW)) and Avrami (bottom right).

Determination of the activation energy is also strongly influenced by the applied model. The different qualities of fitting are represented within the results. In general the activation energies obtained for Ostwald ripening and Avrami growth are equal within three esd's. This is also true for the energy obtained for Ostwald ripening in the combined model.

The activation energies determined for oriented attachment are smaller. Additionally they exhibit very large esd's. This is also visible in the Arrhenius plots. All graphs

using reaction rates obtained with the model of oriented attachment do in general not show clear trends. Additionally the errors of the reaction rates are rather large.

The activation energy which was previously obtained using the same dataset was 52(4) kJ/mol, which is in good agreement to the values obtained for Ostwald ripening and Avrami growth in the present study. A comparable energy (2.2 eV $\approx$ 50 kJ/mol) is reported for crystallization of CeO_2 from an amorphous precursor as obtained via spray pyrolysis (Rupp *et al.*, 2010) or the activation energy (49(1) kJ/mol) of growth of ceria nanoparticles prepared using a solution-mediated approach (Allen *et al.*, 2008).

4.4.4   Conclusion

In general, the growth of nanocrystalline materials can be studied using a variety of different models. Depending on the observed system, some might not be suitable for one case even though they are in another.

For the isothermal growth of ceria, which was reinvestigated, several models can be applied which lead to comparable results of the activation energy of about 50 kJ/mol. Furthermore even the mechanism of growth can be explained using the same process.

4.5 Isothermal and isochronal growth of sol-gel prepared Cu₂ZnSnS₄

Parts of this work presented in this chapter were published in: Melanie Müller, Cristy Leonor Azanza Ricardo, Rosa Di Maggio and Paola Scardi: *Growth kinetics of Cu₂ZnSnS₄ thin films and powders*. Powder Diffraction (2013) S2, S228-S241.

Rosa Di Maggio helped with sample preparation. Cristy Leonor Azanza Ricardo assisted in synchrotron measurements. Mahmoud Abdellatief (Sincrotrone Trieste) helped with handling of the furnace for synchrotron measurements and the obtained data and Matteo Leoni (University of Trento) during data analysis with PM2K.

4.5.1 Introduction

A key parameter in the performance of thin film solar cells is the microstructure of the absorber layer (Wang *et al.*, 2011). Therefore the evolution of the microstructure needs to be understood in order to prepare high performing solar cells. In case of sol-gel prepared absorber layers, especially the growth process of the absorber layer needs to be investigated so that a suitable microstructure is obtained and the best possible junction between the different parts of a solar cell is produced.

Thus, the growth kinetics of a thin film of CZTS prepared by a sol-gel route was studied by *in-situ* Synchrotron Radiation X-ray Diffraction (SRXRD) using isothermal and isochronal measurements. The main focus is the evolution of the size distribution of the crystalline domains, which is followed by a study of the diffraction line profiles, showing fine details in the thin film growth process.

4.5.2 Experimental

4.5.2.1 Sample preparation

The precursor sol for the preparation of the CZTS thin film and powders was made from cupric chloride (Cu(II)Cl₂·2H₂O), zinc chloride (Zn(II)Cl₂), tin tetrachloride

Sn(IV)Cl$_4$ and, as sulphur source, thiourea (SC(NH$_2$)$_2$). The elemental ratios Cu:Zn, Cu:Sn and Cu:S are equal to 2, 2 and 0.25, respectively.

In order to prepare sols three different solvents were investigated:

        I)   ethanol (sol I),

        II)   ethanol with 5 % glycerin (sol II),

        III)   ethanol with 10 % ethylene glycol (sol III).

Glycerin and ethylene glycol act as stabilizers of the metal ions within the obtained sol.

In 40 ml of the respective solvent 3.41g of Cu(II)Cl$_2$·2H$_2$O, 1.37 g of Zn(II)Cl$_2$ and 1.17 ml of Sn(IV)Cl$_4$ were dissolved under stirring. After adding 6.09 g of SC(NH$_2$)$_2$ a yellow sol and a white precipitate formed. Further details on the precipitate are given in chapter 4.6.3.1.

Glass capillaries or glass slides were dipped into the sol and thermally treated at 320°C for 20 minutes in nitrogen atmosphere. After the thermal treatment, a nanocrystalline CZTS thin film formed on the surface of the glasses. The coated capillaries were used as prepared and the glass slides were used to prepare CZTS powder, scratching the thin film from the glass slides and grinding it. Furthermore powder can be prepared by treating a sufficient quantity of the sol within a vessel. Residuals from preparation (e.g. chloride) are still present within the samples, independent from the solvent and substrate.

4.5.2.2   Measurements

Two different types of *in-situ* SRXRD measurements were performed at the MCX beamlime of the synchrotron Elettra (Trieste, Italy) using a wavelength λ of 0.82667Å.

Isothermal data of samples prepared with sol I were collected in Debye-Scherrer geometry using a special goniometer head developed at MCX, which allows measuring a sample in inert atmosphere to avoid oxidation. For measurement, the tip of the sample capillary is removed and the whole thin film coated capillary is covered with an additional, larger capillary. The special geometry of the goniometer head allows for an inert gas (argon in the present case) to be fluxed through and along the sample capillary (see Figure 4.12).
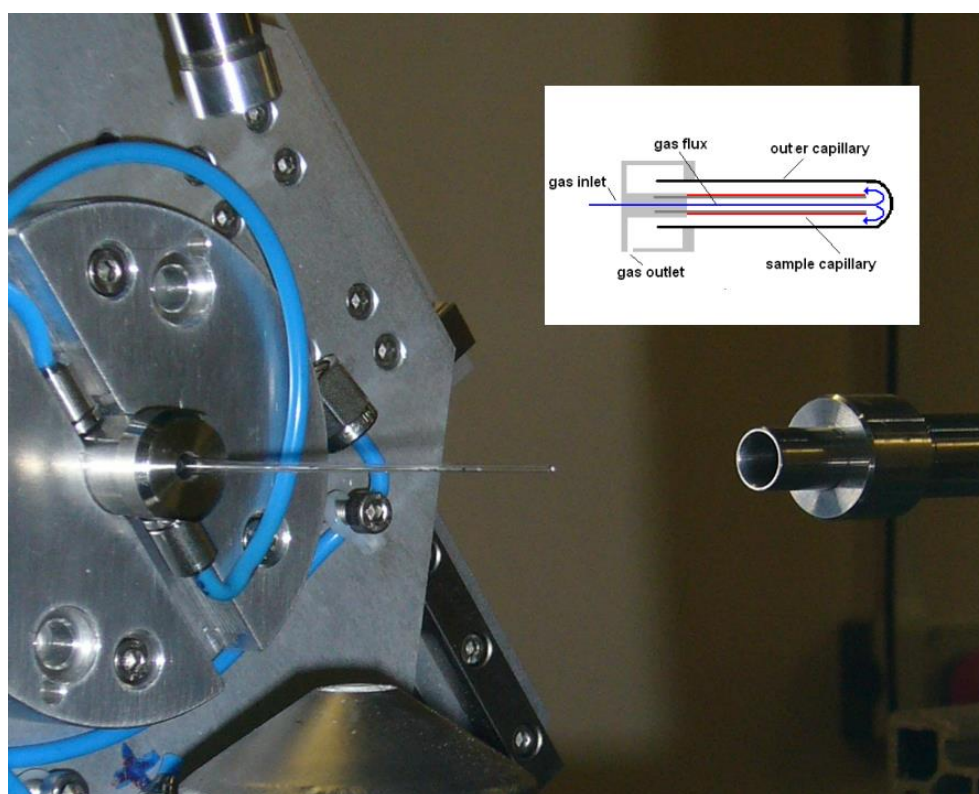
Figure 4.12: Measurements setup of the isothermal measurements at the MCX beamline of Elettra (Trieste, Italy). Capillaries, hot air blower, beamline and detector are shown. The detailed capillary setup with gas flux is shown in the drawing.

The X-ray beam was focused on the sample capillary in order to reduce the contribution of the glass signal from the covering capillary. A hot air blower was used to heat up the whole system. The measurements were performed at constant

temperature; therefore the sample was moved into the hot air stream after the desired temperature was reached. A single measurement took three minutes; the time delay between two measurements was 38 seconds. For this preliminary study, measurements could be performed at two temperatures, 500°C and 575°C, with a total measurement time of 344 minutes and 40 minutes, respectively.

Moreover isochronal measurements were performed using a high temperature induction furnace with a translating image plate in Debye-Scherrer geometry. For those measurements, the CZTS powders prepared using the three different solvents were sealed in capillaries so that the atmosphere remained unchanged. While heating with constant rate, the image plate was moved with a constant speed, so that the measurement was performed in a continuous way. Generally, the measurements were performed between 300°C and 600°C, data integration was performed in strips that reflect a 3K range, so each series corresponds to 100 measurements. At temperatures below 300°C, no grain growth was observed. Samples were measured with heating rates of 2 K/min, 4K/min and 6 K/min.

4.5.3   Results

4.5.3.1   Isothermal measurements

The recorded isothermal data were analysed by Whole Powder Pattern Modelling (Scardi and Leoni, 2002) using the PM2K software (Leoni *et al.*, 2006).

Within modelling, besides the instrumental profile component which was previously determined by analysing the lanthanum hexaboride standard from NIST (NIST SRM 660a), the main feature considered in the analysis was the particle size distribution. In the present case a lognormal distribution of spherical particles was chosen. A fourth order Chebyshev polynomial was used to describe the background contribution within the modelling. After some time at elevated temperature a contamination phase of SnO_2 begins to form, which was also included in modelling. The reason for formation of this phase is a not perfectly sealed sample setup. One example of the modelling of that data is given in Figure 4.13.

It can be seen from powder diffraction data that the starting material is poorly crystallised, exhibiting the typical broad peaks of nanomaterials in powder diffraction patterns. This is a typical result for materials prepared using a sol-gel approach. The average domain size as determined by PM2K is 2.1 nm. The variance of the size distribution is 0.8 nm. The presence of a non-crystalline fraction of the material that contributes to the amorphous glass peak cannot be excluded (Müller *et al.*, 2013b).
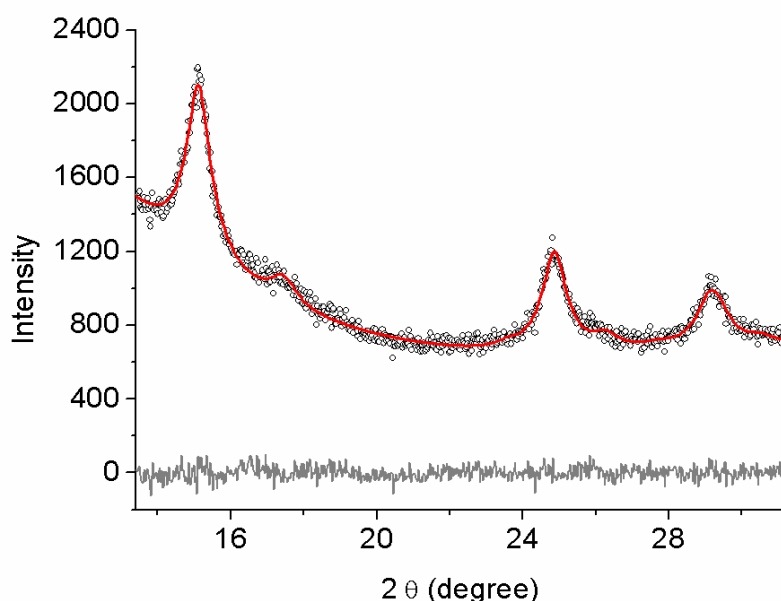
Figure 4.13: Powder diffraction data (black dots) of a CZTS thin film measured at RT ($\lambda = 0.82667$ Å). The modeled pattern (red) line and the difference curve (grey line) are shown.

At elevated temperatures the powder diffraction peaks become sharper with time as the domain size increases. Obviously the process is much faster for the measurement at 575°C in comparison to the measurement at 500°C.

The obtained results from modelling in PM2K were analysed using the previously described approach of the volume dependent JMAK equation (4.7). In order to

determine the domain volume the mean μ and variance of the size distribution σ were refined. The evolution of the size distribution in dependence on time is shown in Figure 4.14. From that plot, the growth process is clearly visible. Initially the distribution is very narrow, which indicates that the domains are small (a few nm) and little dispersed. At the beginning of the growth process the distribution changes drastically, which is given by a broadening of the distribution and a shift to larger domain values. Later the process is slower.
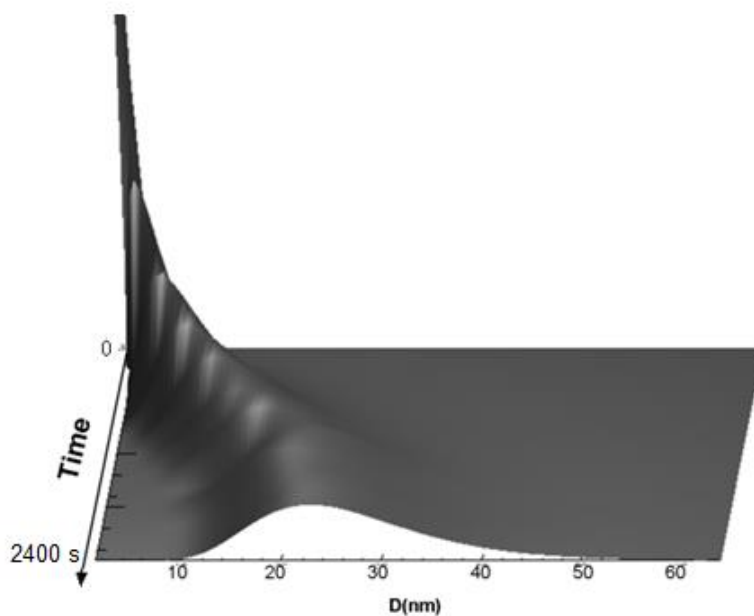
Figure 4.14: Evolution of the size distribution with time for an isothermal measurement series at 575°C on a time interval of 2400 seconds (picture prepared using Powder3D (Hinrichsen *et al.*, 2006)).

The evolution of the domain size distribution is given by the changes of μ and σ. Therefore the values obtained for those parameters in dependence on time for the two measurement series are shown in Figure 4.15. For both measurements the expected behaviour of the parameters is observed. The value of μ is increasing, while the value of σ is decreasing and both parameters in each measurement reach an asymptotic value.
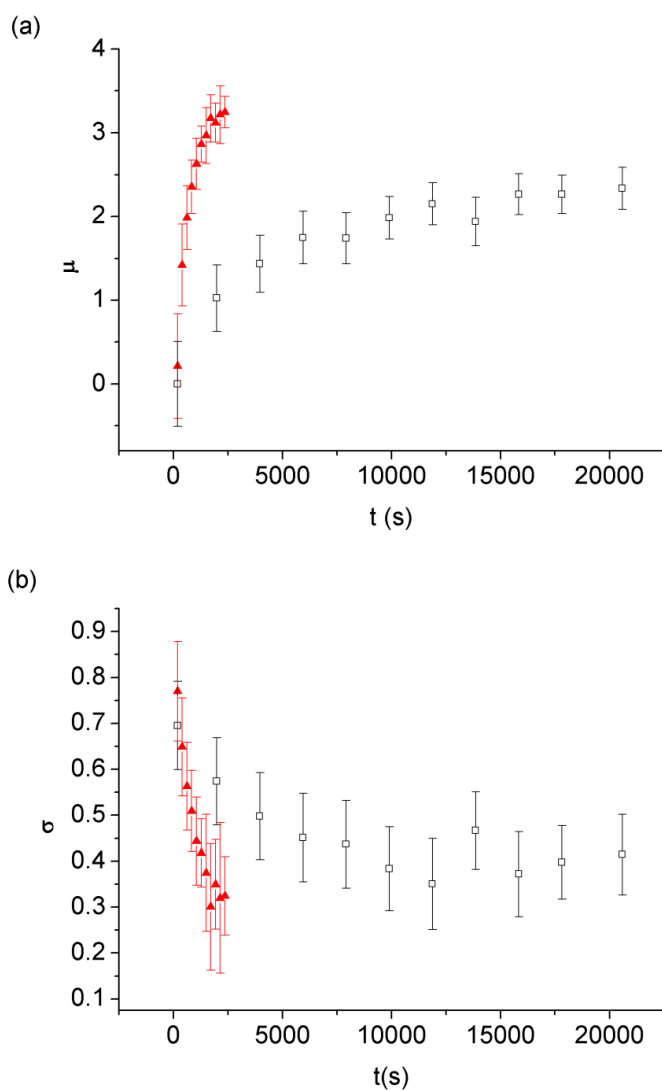
Figure 4.15: Evolution of μ (a) and σ (b) in dependence on time for the measurement series of CZTS thin films prepared from sol I performed at 500°C (open black squares) and 575°C (solid red triangles).

The evolution of the volume growth rate *a(vol)* (see equation (4.7)) with temperature is plotted in Figure 4.16. In order to calculate these values, the initial volume *<V(0)>* and the final volume *<V(∞)>* needed to be determined. The average initial volume *<V(0)>* was determined using a measurement at room temperature (Figure 4.13) while the final volume *<V(∞)>* for both temperatures was determined using best fits of μ and σ. Fitting of the evolution of these values is necessary as the growth process

is not yet completed at the end of the measurements. This can be seen, as the typical curve shape obtained in such processes is cut (Müller *et al.*, 2013b).

The Sharp-Hancock plot (see Figure 4.17) shows linear trends for both measurement series. From these plots the kinetic constant k and the Avrami exponent n were determined. In a linear fit, n is equal to the slope, while the intercept is equal to $n \ln k$. The first data point was not taken into account as the volume growth rate is less than 0.01 and therefore errors are large. Parameters obtained in fitting are given in Table 4.5.

The obtained Avrami exponents of 1.5 and 2.5 respectively can be explained by diffusion controlled growth of spherical particles. In case of a JMAK exponent of $n = 2.5$ it is assumed that the nucleation rate is constant, while for an exponent $n = 1.5$ a nucleation rate of zero is assumed (Christian, 1965; Spassov *et al.*, 2004; Rodríguez *et al.*, 2012). Thus at 575°C, there is the possibility that new nuclei form, while at 500°C only previously formed domains continue growing without formation of new ones. The temperature of the measurement, which was used in the analysis, will allow for diffusion, as it equals 0.61 - 0.67 T_{melt} (Olekseyuk *et al.*, 2004).
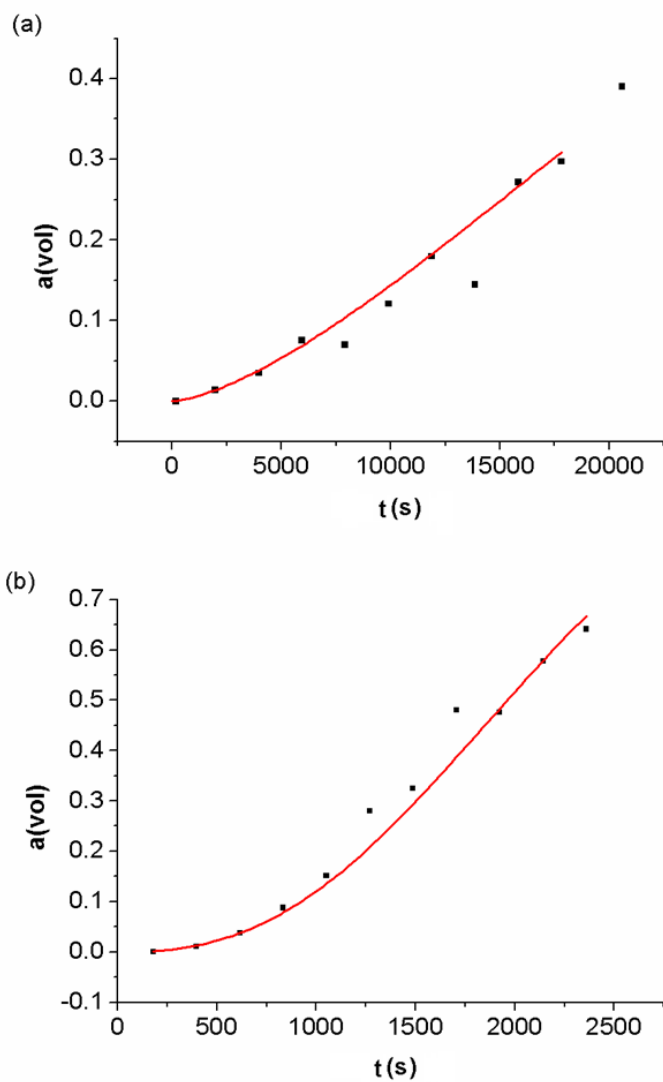
Figure 4.16: Evolution of the volume growth rate *a(vol)* (see equation (4.7)) in dependence on time for the measurement of CZTS thin films prepared from sol I at (a) 500°C and (b) 575°C and the corresponding fit (red line) using the JMAK equation.
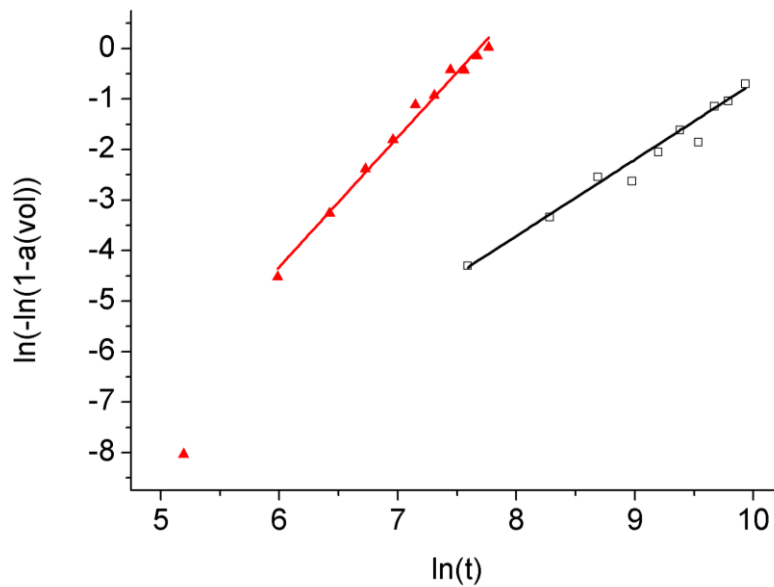
Figure 4.17: Sharp-Hancock plot (plot of ln(t) versus ln(-ln(1-$a(vol)$))) for CZTS thin film growth at 500°C (open black squares) and at 575°C (solid red triangles).

Table 4.5: Results for k and n obtained in fitting for measurements at 500°C and 575°C.

measurement temperature	500°C	575°C
Avrami exponent n	1.5(1)	2.5(1)
kinetic constant k (s^{-1})	2.9(3)E-5	4.4(1)E-4

The activation energy of the growth process can be estimated using the Arrhenius equation (4.8). Though this value can only be considered as an estimate as only two measurement series are available for analysis. In order to determine the activation energy 1000/T is plotted versus $R \ln k$. For the present study a value of about 210 kJ/mol is obtained. This result is higher than the value of 105(39) found by Weber *et al.* (2009).

4.5.3.2   Isochronal measurements

Isochronal measurement were performed using powdered samples either obtained from scratching CZTS thin films from glass slides or from thermal treatment of the bulk sol. The CZTS thin films were used in case of sol I. In this case powder obtained from a bulk treatment is not stable and undergoes a change that results in a slowdown of the domain growth with increasing sample age. Measurements showed for powders scratched from glass slides that even a time delay between sample preparation and the beginning of measurement causes a change in reaction. Samples measured directly after preparation are denoted as "fresh", samples with time delay are called "aged". From sols II and III stable powder were obtained.

Measurements were performed with heating rates of 2K/min, 4K/min and 6K/min for each sample. Given the different measurement setup for the non-isothermal measurements, WPPM could not be applied due to insufficient data quality. Therefore the data was analysed using the inverse of the integral breadth of the peaks as obtained from Rietveld refinement with TOPAS (Bruker AXS, 2009). The evolution of the normalized change of that parameter (denoted as x) was studied as this value is directly related to the size of the scattering domains. Although the approach using the integral breadth is not entirely rigorous, this approach is appropriate to the studied case, and compatible with the limited data quality. In the following the results obtained for the different samples are shown.

Sample from sol I (ethanol):

A plot of the relative inverse of the integral breadth x in dependence on temperature is shown in Figure 4.18. Due to the peculiarities of the sample stability, two different sets of measurements were performed, one series of samples measured directly after capillary preparation and another with a time delay in between. Clear differences in the growth behaviour can be seen. Additionally, independent from the set, it can be seen that the growth regime changes at a certain point as the rate of relative change of the integral breadth decreases drastically.
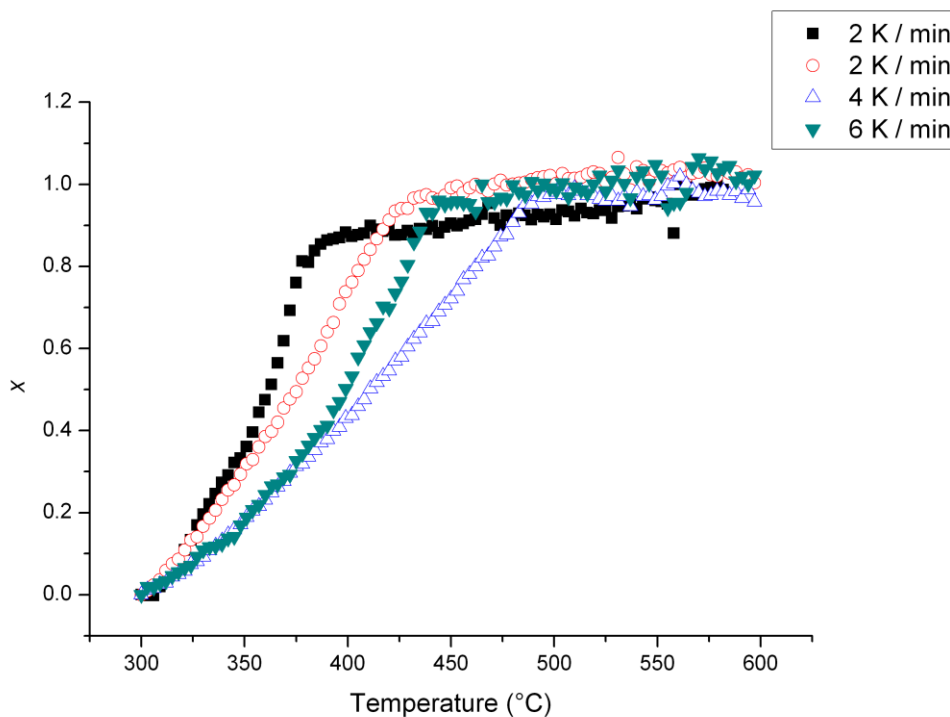
Figure 4.18: Samples from sol I: Relative change of the inverse of the integral breadth (*x*) in dependence on temperature for the measurements of fresh samples (solid symbols) and aged sample (open symbols).

From an Ozawa plot for both sets of measurements, the Avrami exponent *n* was determined. The plots are shown in Figure 4.19. As the main growth process happens in the initial growth regime, for the Ozawa plot a temperature of 366°C was chosen. For both sample sets a comparable Avrami exponent was derived, therefore the mean value was chosen for further analysis. The obtained Avrami parameter of $n = 0.85$ corresponds to a growth process characterized by bulk nucleation with constant number of nuclei. The shapes of the growing domains seem to be plates and needles (Lee & Choi, 1997).

Laboratory XRD measurements of similar samples showed variations of peak intensities, which can be related to an oriented growth of needles within the thin films. Therefore this hypothesis seems to be reasonable.
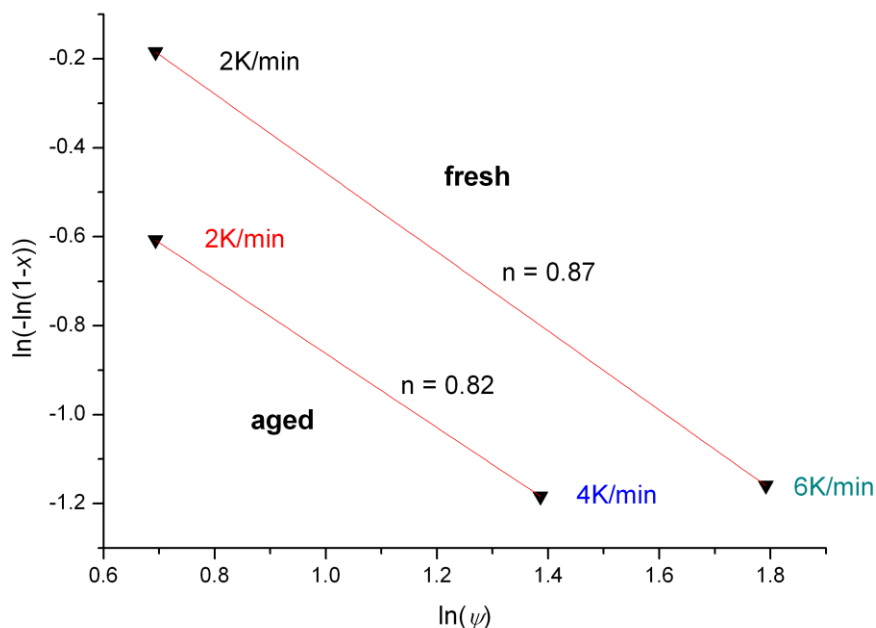
Figure 4.19: Ozawa plot for the two different sample series (fresh and aged) prepared form sol I. The selected temperature was 366°C.

The activation energy of the growth processes was determined using Šatava plots (see Figure 4.20). The fitting was performed for the initial growth process as it is significant. For calculation of the activation energy E, the previously obtained Avrami parameter of $n = 0.85$ was used. The activation energies (see Table 4.6) are in good agreement with the one (105(39) kJ/mol) reported by Weber *et al.* (2009).

Table 4.6: Results obtained in fitting of the Šatava plot for measurements performed using samples prepared from sol I and calculated activation energy.

sample	fresh		aged	
heating rate (K/min)	2	6	2	4
slope of the linear fit	-15.6(5)	-12.0(2)	-11.9(1)	-9.2(1)
activation energy (kJ/mol)	145(5)	112(2)	111(2)	85(2)
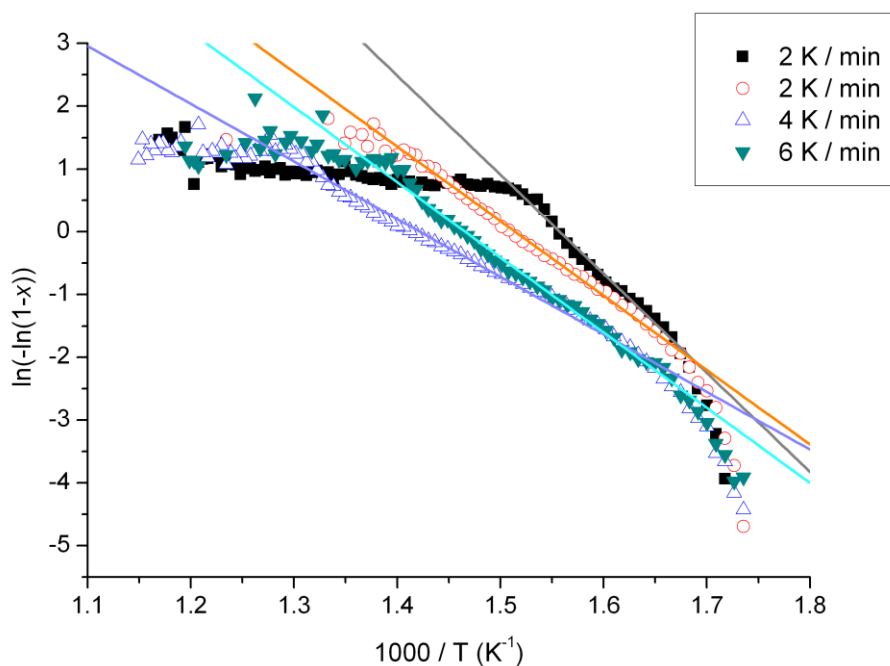
Figure 4.20: Šatava plot for the measurements performed with sol I: fresh (solid symbols) and aged (open symbols) and corresponding linear fits.

Sample from sol II (ethanol + 5% glycerine):

Samples prepared with sol II were measured using the same heating rates which were used for samples from sol I. The plots of the relative change of the integral breadth are shown in Figure 4.21.

For the present case, the sample measured at a rate of 6K per minute shows an unexpected behaviour. One would assume that the reaction is delayed in temperature with respect to the other heating rates, though growth happens at lower temperatures. One reason might be, that the capillary, which was used for the measurement at 6 K/min was not perfectly sealed, so that evolving gases could exhale from the sample, changing the reaction conditions. Therefore this measurement was not considered for determination of the Avrami exponent from the Ozawa plot, which was performed for the samples measured with heating rates of 2 K/min and 4 K/min using two different temperatures. The Ozawa plot is shown in Figure 4.22.
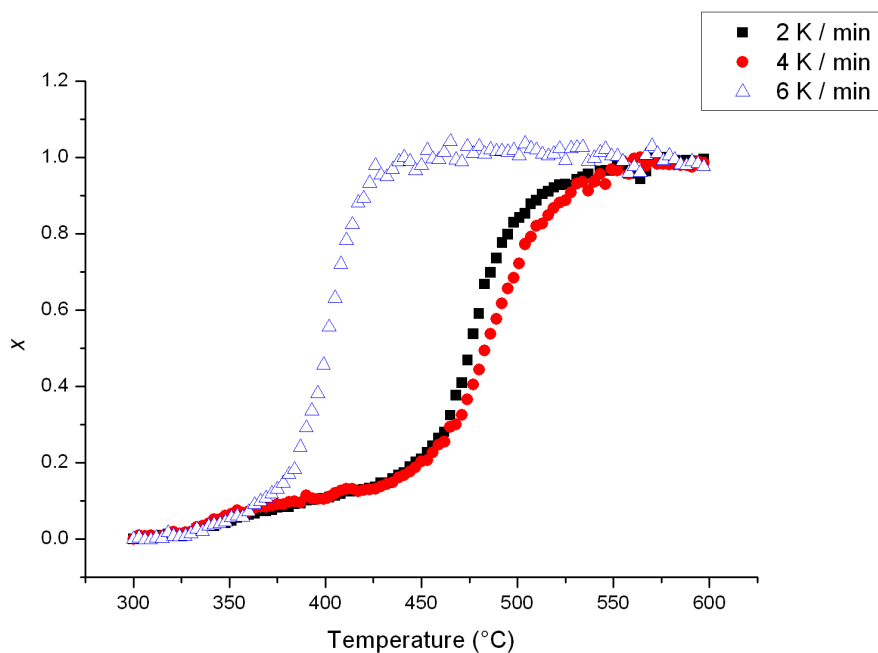
Figure 4.21: Samples from sol 2: Relative change of the inverse of the integral breadth (*x*) in dependence on temperature. The sample measured at a rate of 6K/min (open symbols) shows an unexpected behaviour. One would assume that the reaction is delayed in temperature with respect to the other heating rates.
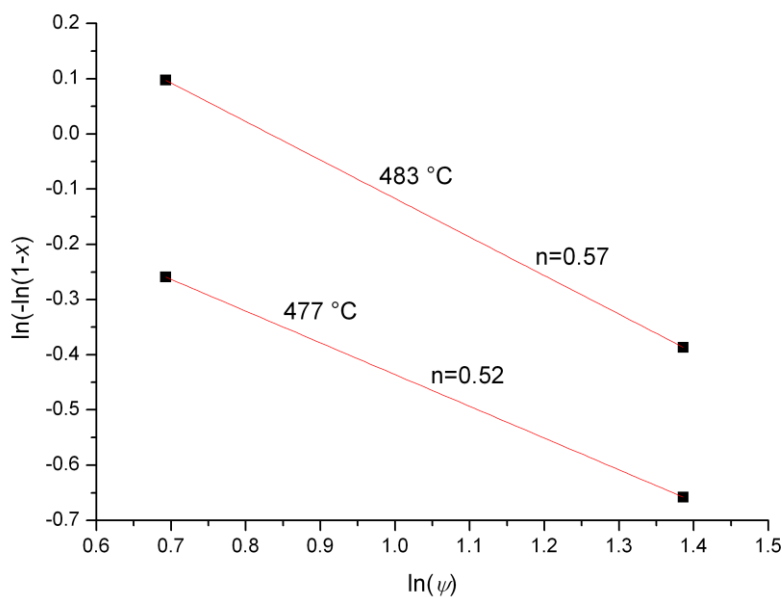
Figure 4.22: Ozawa plot for the samples form sol II. Measurements performed with 2 K/min and 4 K/min heating rates were taken into account. Two temperatures were selected for analysis.

From the Ozawa plot an Avrami parameter *n* of about 0.5 could be determined. Such a parameter is obtained for diffusion controlled processes, which is happening at a limited number of reaction sites (Grundy *et al.*, 1987). One reason for that might be the addition of glycerine, which seems to cause a modification of the surface of the crystalline domains. During thermal treatment that "protective layer" gets removed so that the domains can grow together using these spots.

The activation energy was again determined using Šatava plots. In this case all three measurements were taken into account assuming an Avrami exponent *n* = 0.5 in all cases. The plots are shown in Figure 4.23. The corresponding results are reported in Table 4.7.
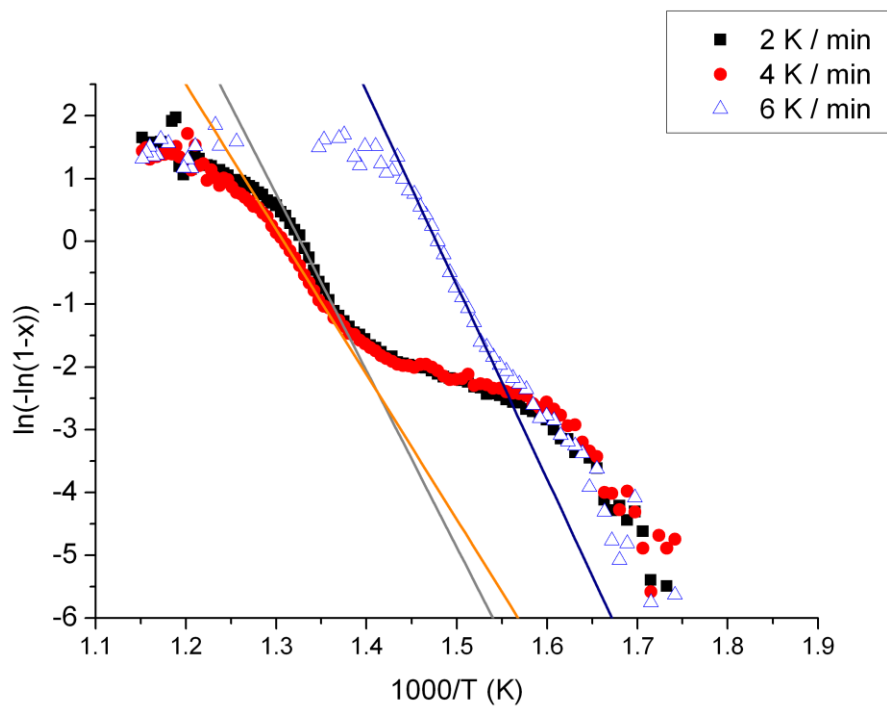
Figure 4.23: Šatava plot for the measurements performed with sol II and corresponding linear fits.

Table 4.7: Results obtained in fitting of the Šatava plot for measurements performed using samples prepared from sol II and calculated activation energy.

heating rate (K/min)	2	4	6
slope of the linear fit	-27.2(7)	-21.2(4)	-30.0(8)
activation energy (kJ/mol)	430(10)	335(6)	474(10)

The activation energy of the nanocrystalline growth of samples prepared from sol II is much higher than the one obtained for samples from sol I. This is also evidenced in laboratory XRD measurements. XRD pattern taken for samples prepared from sol I exhibit much sharper peaks than pattern from sol II after undergoing the same thermal treatment.

Sample from sol III (ethanol + 10% ethylene glycol):

Due to problems during measurements some measurement series of sol III cannot be used in data analysis. Only the samples measured using heating rates of 2K/min and 6K/min are suitable. The plots of the relative change of the integral breadth for these two are shown in Figure 4.24. The growth process is clearly split in three different regimes. The initial growth is characterised by a fast increase of x. After that, follows a regime which is characterised by a much slower growth that seems to be approximately linear. Another regime with linear growth, though higher growth rate, sets in at higher temperatures, before finally the growth stops. For the present case, it is difficult to obtain an Ozawa plot as it has to be performed at a specific temperature T. In Figure 4.24 it can be seen that the temperature range in which both samples exhibit the fast growth process is narrow. An Ozawa plot at $T = 330°C$ is reported in Figure 4.25. The obtained Avrami parameter is $n = 2.3$. This corresponds to a diffusion controlled three dimensional growth with constant nucleation rate (Christian, 1965). The activation energy again is obtained for the corresponding Šatava plots, which are shown in Figure 4.26. Results are reported in Table 4.8. These

results can only be seen as indicative values due to the problems in measurement and data analysis.
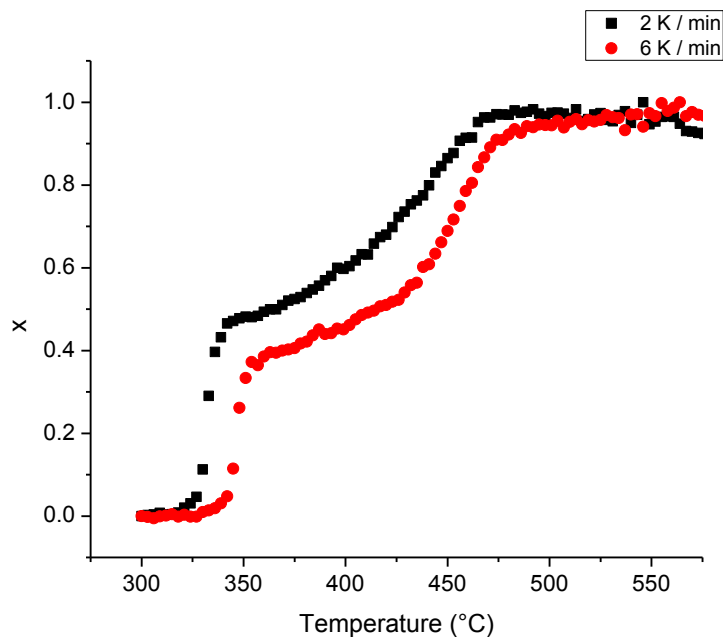
Figure 4.24: Samples from sol III: Relative change of the inverse of the integral breadth (x) in dependence on temperature for measurements performed with heating rates of 2 K/min and 6 K/min.
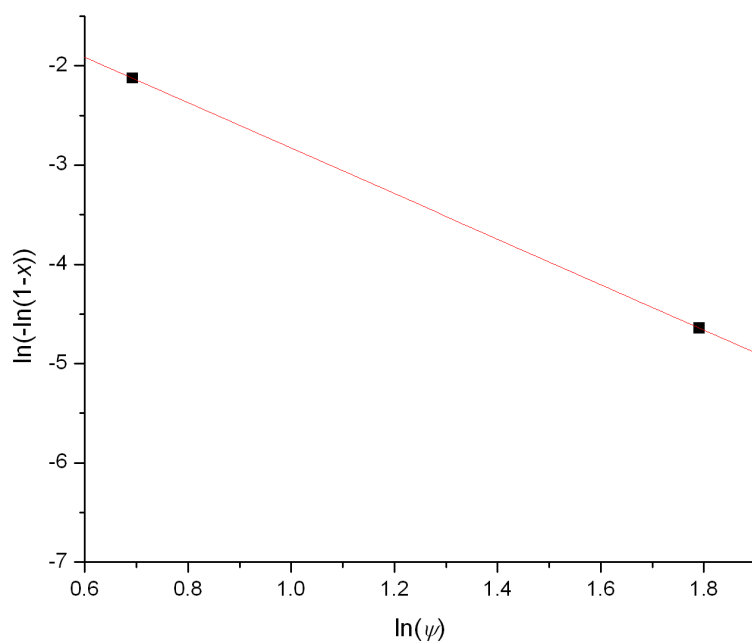
Figure 4.25: Ozawa plot for the samples from sol III at $T = 330°C$.
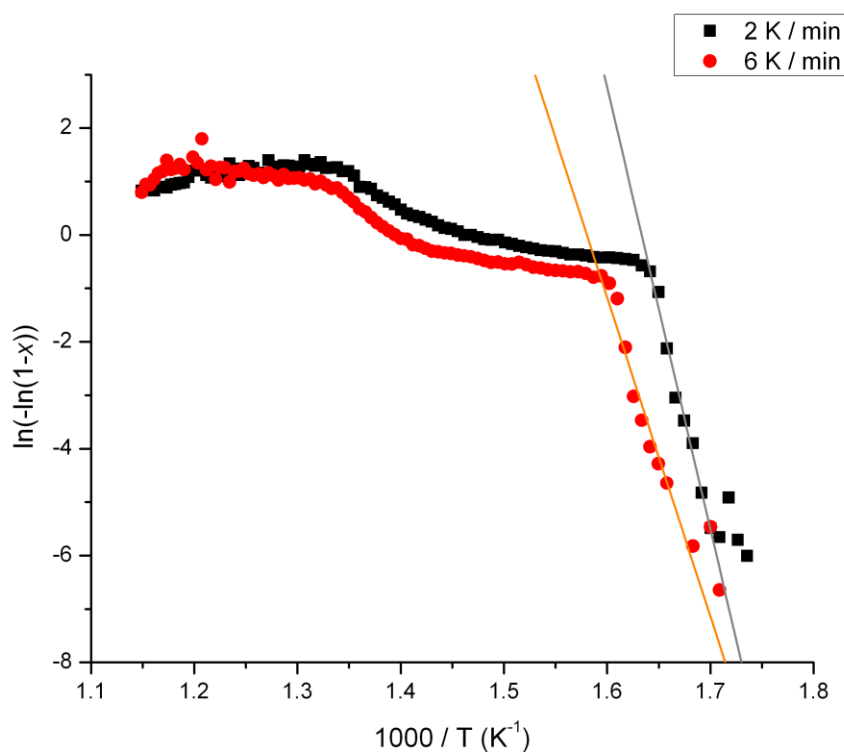
Figure 4.26: Šatava plot for the measurements performed with sol III and corresponding linear fits.

Table 4.8: Results obtained in fitting of the Šatava plot for measurements performed using samples prepared from sol III and calculated activation energy.

heating rate (K/min)	2	6
slope of the linear fit	-82(4)	-60(4)
activation energy (kJ/mol)	229(14)	206(14)

4.5.4 Conclusion

The present work shows that diffraction line profile analysis of powder diffraction data collected *in-situ* can be a valuable tool to perform thermal analysis studies and in particular to follow growth kinetics in nanocrystalline materials. The domain growth of CZTS thin films and powders was investigated by high temperature synchrotron X-

ray diffraction, using isothermal and isochronal measurements. The isothermal data were investigated by WPPM, following the domain size distribution in dependence on time. The changes in the domain volume were investigated using a JMAK type equation. The growth was found to be diffusion controlled from small dimensions, while the nucleation rate is temperature dependent, so the nucleation rate is either zero (at 500°C) or constant (at 575°C). The activation energy of this process can be estimated to a value of about 210 kJ/mol.

The isochronal data of three differently prepared samples were analyzed using the normalized inverse of the integral breadth of the peaks, as this value is approximately proportional to the size of the scattering domains. From Ozawa plots, Avrami parameters indicating the growth process were derived. The activation energy of growth was calculated from fits of Šatava plots.

Samples from sol I exhibit a lower activation energy for powder growth in comparison to the one obtained in the thin film, although the value obtained from just two isothermal measurements is not as reliable as that given by the isochronal data. A lower energy for the growth from the powder sample is nevertheless realistic: owing to the higher specific surface of a powder, residual material from the preparation (e.g. chloride) can evolve more easily, and additional nuclei may form at the surface. The samples prepared from sol II and sol III both exhibit a higher activation energy in comparison with samples from sol I. In these cases additives to the solvent were used, indicating that they influence the resulting sol. This can be seen in both, the growth mechanism and the activation energy.

4.6 Properties of sol-gel prepared CZTS and its application in photovoltaic devices

The publication of the work presented in this chapter is in preparation: Melanie Müller, Cristy Leonor Azanza Ricardo, Claudia Malerba, Francesco Biccari, Alberto Mittiga, Simona Maggini, Rosa Di Maggio and Paolo Scardi: *Influence of different solvents on the properties of CZTS thin films prepared by sol-gel*.

Cristy Leonor Azanza Ricardo assisted in synchrotron measurements and took care of the sputtering process in the solar cell preparation. Claudia Malerba, Francesco Biccari and Alberto Mittiga are responsible for the characterisation of the prepared thin film solar cell. Simona Maggini and Rosa Di Maggio helped with sample synthesis.

4.6.1 Introduction

Cu_2ZnSnS_4 (CZTS) is a suitable material for photovoltaic absorber layers. In the present work, CZTS thin films were prepared using a sol-gel approach. For sol preparation different solvents were tested. The samples were analysed using X-ray powder diffraction (XRD), scanning electron microscopy (SEM), energy dispersive X-ray spectroscopy (EDX) and spectrophotometry.

It was found that a thermal treatment at 500°C improves the properties of the final CZTS film. The stoichiometry of the obtained CZTS thin film strongly depends on the solvent used for preparation, as the solvent influences the sol stability. CZTS thin films deposited on molybdenum were used to prepare solar cells with the structure glass/Mo/CZTS/CdS/ZnO:Al in order to prove the applicability of the prepared films in a device.

4.6.2   Experimental

CZTS thin films were prepared using a sol-gel approach. The sol was prepared as stated in the previous chapter (see chapter 4.5.2.1). The same three solvents were used for preparation:

I)   ethanol,

II)   ethanol with 5 % glycerin,

III)   ethanol with 10 % ethylene glycol.

The formation of the yellow sol is accompanied with the formation of a white precipitate; therefore all sols were filtered before use.

CZTS thin films were obtained by dip coating. Soda lime glass (SLG) and Mo-coated SLG were used as substrates. They were dipped into the sol, withdrawn at 0.5mm/sec and finally treated at 320°C in argon flux for 20 minutes. This was repeated on average 4 times so that a suitable thickness (about 1 μm) of the CZTS layer was obtained.

The final CZTS thin films underwent a further thermal treatment at 500°C for one hour in order to improve the crystallinity. Samples that were treated this way are labelled TT.

The films on SLG were analysed by X-ray powder diffraction (XRD), using a Rigaku IIID Max diffractometer with CuK_{α} radiation and then modelled with the software TOPAS (Bruker AXS, 2009). The chemical composition of the thin films was analysed by scanning electron microscopy (SEM), using a Philips XL30 ESEM for energy dispersive X-ray spectroscopy (EDX). The optical properties of the different CZTS films were studied by spectrophotometric measurements, performed using a Perkin Elmer Lambda 9, equipped with an integrating sphere.

The CZTS films deposited on molybdenum were used to prepare photovoltaic devices, in order to test their properties as absorber layers. After the thermal treatment at 500°C, cadmium sulphide (CdS) was deposited as buffer layer by chemical bath

deposition, following the procedure proposed by Mann *et al.* (2010). In order to complete the device, ZnO:Al was sputtered on the sample. The resulting device had the following set-up: SLG/Mo/CZTS/CdS/ZnO:Al.

4.6.3   Results

4.6.3.1   Thin film characterisation

The initial formation of the CZTS thin film was controlled by XRD and SEM. The as prepared films (before thermal treatment at 500°C) exhibit poor crystallinity, which is typical for sol-gel materials. The XRD powder patterns exhibit broad peaks (see Figure 4.27). In order to compare the domain sizes, the volume weighted mean size as derived from the integral breadth (LVol-IB), was considered. Analysis was performed using TOPAS (Bruker AXS, 2009). Accordingly, the LVol-IB could be determined as about 3-3.5 nm for all the samples before the thermal treatment.

The effect of the thermal treatment at 500°C can also be seen in XRD patterns and depends on the solvent which was used for sample preparation: samples prepared using ethanol with 5 % glycerin (II) showed less significant grain growth with respect to the other two. After thermal treatment the LVol-IB is 7 nm for sol II and about 20 nm for sols I and III. Those values are in agreement with SEM observations. The presence of additional zinc or copper phases could not be observed from XRD at any condition. Tin oxides, namely SnO_2, though may result from the high temperature treatment at 500°C in the case of a not perfectly sealed furnace. The addition of a small amount of sulphur (about 0.1 g) during thermal treatment can avoid oxidation.
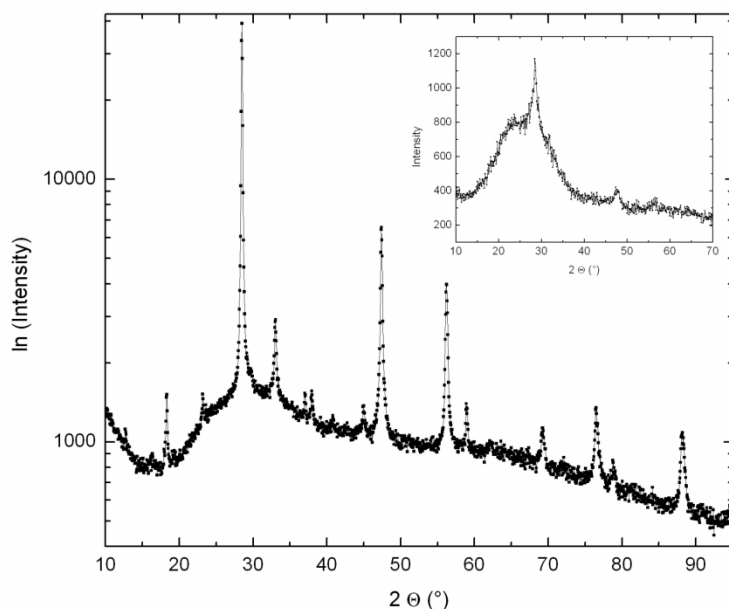
Figure 4.27: X-ray diffraction pattern obtained after the high temperature thermal treatment at 500°C for a sample prepared from sol I. The intensity is plotted on logarithmic scale. All peaks belong to CZTS. The small inset shows results obtained for a sample before high temperature treatment.

The actual chemical composition of the thin films was analysed by EDX. The amount of thiourea which is used for the preparation of the sols is twice the stoichiometric one. Additionally a white precipitate is formed. The amount of the precipitates strongly depends on the solvent. Using solvent I the formation is remarkable, while it is almost negligible for sol II and III. XRD pattern of the precipitate indicated that it is mainly composed of a crystalline copper thiourea chloride complex. Therefore, the sols used for coating after the filtration changed their composition towards a Cu-poor stoichiometry. It was found that samples prepared from sol I have a metal ratio $Cu/(Sn+Zn) = 0.7$-0.8. Copper poor and zinc rich samples were reported to behave better (Chen et al., 2010) and Kobayashi et al. (2005) found the best performances with ratios in the range $Cu/(Sn+Zn) = 0.8$-0.9. As the addition of glycerin and ethylene glycol to ethanol reduced the formation of precipitates drastically, the composition of films prepared with sol II and sol III is nearly stoichiometric. Another effect of the thermal treatment at 500°C is that remaining chloride within the samples, which is present in all the films as residue of the precursor salts, is removed

completely, without modifying further the elemental ratios of Cu, Zn, Sn and S. The composition of the films is reported in Table 4.9.

In order to determine the optical properties of the different CZTS thin films spectrophotometric measurements were performed. The transmittance spectra are shown in Figure 4.28. Using these spectra the band gap energy (E_g) was calculated. In the present work E_{04} was used, which correspond to that energy at which α is equal to 10^4 cm^{-1}. More details on this procedure are given in Malerba *et al.* (2013).

The obtained values of E_{04} are between 1.47 eV and 1.49 eV (see Table 4.9), which is in accordance with literature E_g values (e.g. Katagiri *et al.*, 2001). So the final high temperature thermal treatment does not strongly influence the optical properties of the films, leaving the E_{04} parameter almost unchanged (1.48 eV in comparison to 1.49 eV). The traditional $(\alpha E)^2$ versus E plot of the measurements can be seen in Figure 4.29.

Table 4.9: Sample composition and E_{04} values obtained from the optical characterisation of the CZTS thin films. Photovoltaic parameters (open circuit voltage (V_{OC}); short-circuit current (J_{SC}); fill factor (*FF*), efficiency (η)), measured on respective solar cells under AM1.5G light conditions are also reported.

sample	composition	E_{04} (eV)	V_{OC} (mV)	J_{SC} (mA/cm^2)	*FF* (%)	η (%)
sol I	$Cu_{1.52}Zn_{0.99}Sn_{1.28}S_4$	1.49	253	0.33	27.5	0.02
sol I, TT	$Cu_{1.47}Zn_{1.09}Sn_{1.24}S_4$	1.48	168	8.70	33.5	0.50
sol II, TT	$Cu_{1.97}Zn_{0.99}Sn_{1.10}S_4$	1.47	130	2.00	25.0	0.07
sol III, TT	$Cu_{2.02}Zn_{1.01}Sn_{1.00}S_4$	1.45	93	0.68	25.7	0.02
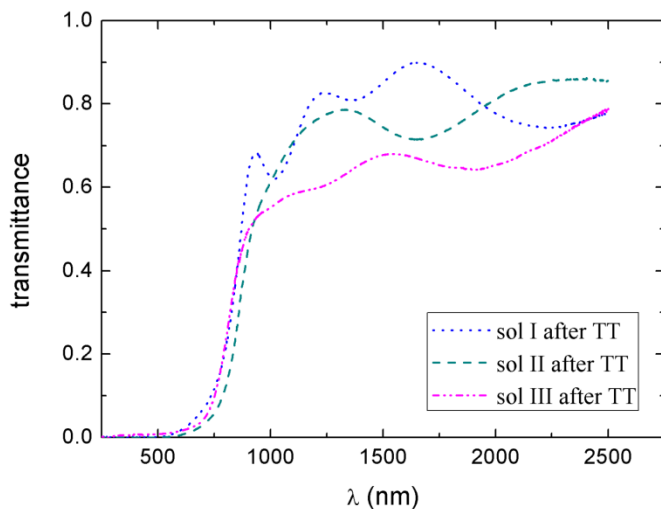
Figure 4.28: Transmittance spectra for CZTS thin films obtained from different solvents after high temperature thermal treatment.
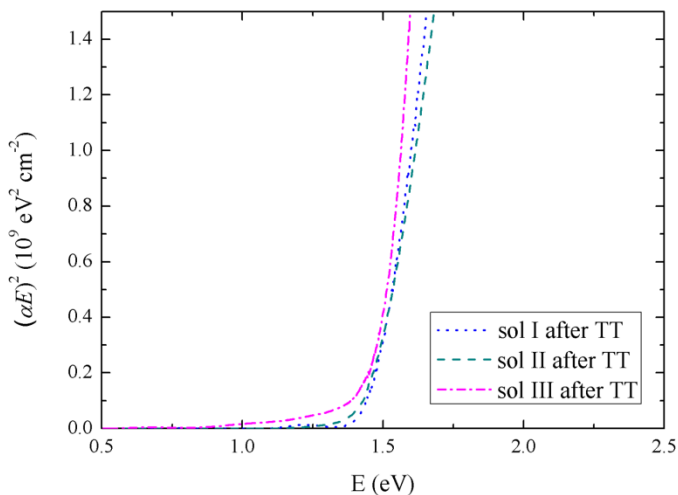
Figure 4.29: Plot of $(\alpha E)^2$ versus photon energy E for CZTS samples which were prepared with different solvents after high temperature thermal treatment.

4.6.3.2   Characterisation of CZTS solar cells

CZTS thin film solar cells were prepared using three different sols (see Table 4.9). All these solar cells have to be considered as test devices. They were produced to get a first characterization of the different materials as absorber layers. Nevertheless, a photovoltaic effect has been observed for each sol.

The best performance could be obtained for a photovoltaic cell from sol I with high temperature treatment at 500°C, a SEM cross-section of that cell is shown in Figure 4.30. This cell exhibits an efficiency of 0.5%, with an open circuit voltage (V_{oc}) of 168 mV, a short-circuit current (J_{sc}) of 8.7 mA/cm^2, a fill factor (FF) of 33.5%. The J-V characteristic of this cell under AM1.5G light conditions is shown in Figure 4.31.
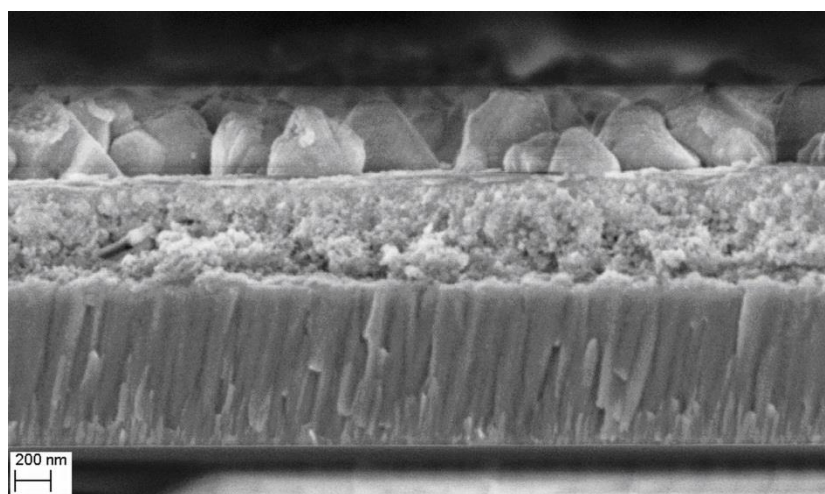
Figure 4.30: SEM cross section of the best performing solar cell (sol 1, TT). At the bottom Mo, very fine polycrystalline CZTS, with ZnO:Al (large grains) on top. The CdS layer is not visible.
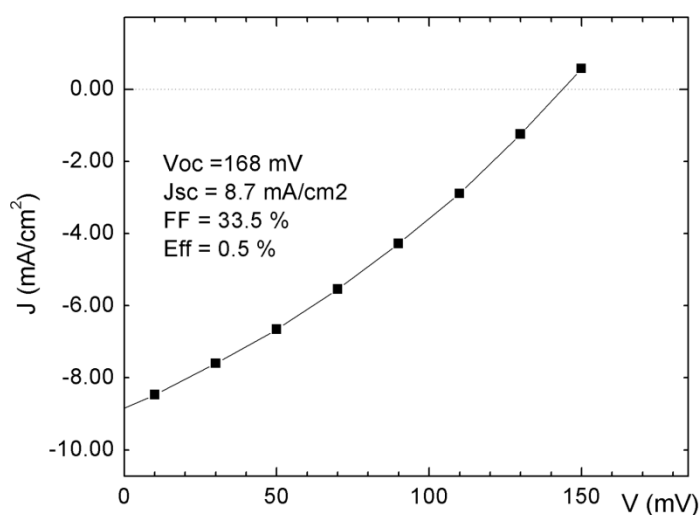
Figure 4.31: *J-V* curve of the cell with the best performance (sol I, TT) under AM1.5G illumination. The open circuit voltage (V_{oc}), short-circuit current (J_{sc}), fill factor (FF) and efficiency (Eff) are reported.

Using the same sol, a device was also prepared from a sample before the high temperature heat treatment. From data in Table 4.9, it can be seen clearly that the high temperature thermal treatment improves the properties of the device. The current density and fill factor are increasing, though the open circuit voltage is reduced. The dark *J-V* characterization shows that the great improvement of the series resistance, R_s, (with a reduction from values of the order of 5×10^2 Ωcm^2 to 3 Ωcm^2) which results upon the heat treatment, however, strongly lowers the shunt resistance, R_{sh}, (from about 5×10^4 Ωcm^2 to 86 Ωcm^2). Thus the V_{oc} is reduced. The dark *J-V* curve of the best device is reported in Figure 4.32, together with the fit of the experimental data and the dark parameters. The lack of the i:ZnO layer can be another factor which lowers the performance of the device.
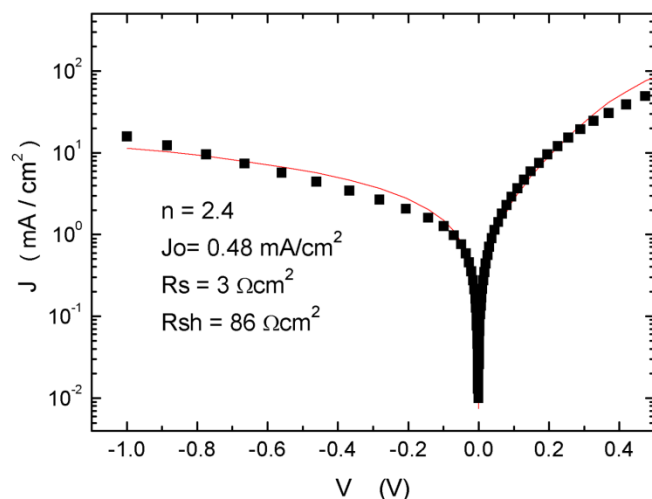
Figure 4.32: *J-V* curve of the cell with the best performance (sol I, TT) in dark condition. The fit is also reported (continuous line), together with the resulting dark parameters: ideality factor (*n*), reverse saturation current density (J_0), series (R_s) and shunt resistance (R_{sh}).

However, the solar cells prepared with sol II and III showed worse performance with respect to the cell from sol I. The reason might be ascribed to the nearly stoichiometric composition and therefore to the insufficient concentration of acceptor-like defects, which are needed to give the required p-type conductivity to the films.

Nevertheless, the addition of glycerin and ethylene glycol to ethanol results in more stable sols and the formation of precipitates is prevented. This will allow controlling the CZTS stoichiometry and preparing absorber layers with more suitable composition in future devices.

4.6.4 Conclusions

CZTS thin films were successfully synthesized using a sol-gel based approach in different preparation conditions. The use of different additives was proven to increase the stability of the starting sol, giving the possibility for a good control of the film composition by reduction of precipitates formation. Optical properties of the films are not influenced by the solvent used for the material preparation and an energy gap of about 1.48 eV was found in all cases. The different films were also tested as absorber layer. The best performing cell, with an efficiency of 0.5%, was obtained from an ethanol based sol after thermal treatment. The performances of the other two cells are limited by the composition of the absorber layer, being almost stoichiometric.

5   Summary

X-ray powder diffraction is a well-established technique to analyse structural and microstructural properties of materials. The possibility to record *in-situ* powder diffraction data allows studying changes within the structure and microstructure of a sample that occur in dependence on the applied external conditions (e.g. temperature, pressure). In the present thesis, *in-situ* X-ray powder diffraction was used to study structural and microstructural changes of different samples occurring at elevated temperature or upon UV illumination.

Several structural phase transitions were studied using the approach of parametric Rietveld refinement. In parametric Rietveld refinement a set of powder diffraction pattern is refined simultaneously, constraining the evolution of some parameters using mathematical models, so that only the variables of the model need to be refined. In order to model and analyse the behaviour of structural parameters, Landau theory and its corresponding equations were used, owing to the fact that structural parameters (e.g. lattice strain, changes in atomic positions or occupancy) comprise an order parameter as defined in Landau theory.

For description of the crystal structure of materials, several different approaches were tested:

1) Traditional atomic coordinates (AC) can always be used to follow structural changes that occur during phase transitions, though for crystal structures with many atoms on general Wyckoff positions in the unit cell or for phase transition with extensive movements of groups of related atoms other possibilities are more suitable.

2) Symmetry modes (SM) describe a crystal structure in dependence on a real or hypothetic structure of higher symmetry. Therefore this approach is ideally suited to study structural phase transitions. In comparison to the previously described AC, SM frequently reduce the number of parameters as only a fraction of all possible SM is activated during a transition. SM are ideally suited to describe transitions with linear movements of single atoms.

3) Phase transitions which involve extended rotations of groups of atoms would force that some symmetry modes cooperate in order to mimic the movement of these atomic groups. Instead such rigid body motions can be followed directly by investigation of position and orientation of the rigid body (RB) (rigid body rotations).

4) In order to enhance and facilitate the approach of rigid body rotations purely rotational symmetry modes (rigid body symmetry modes) (RM) were invented. This approach combines features of symmetry modes and rigid body rotations and is especially effective for phase transitions involving polyhedral rotations.

The high temperature phase transitions of $CsFeO_2$ from orthorhombic to cubic structure at about 80°C was analysed using the SM and the RB approach. It could be proven that these methods are closely related and give an equivalent description of the phase transition. Even though a first-order phase transition, as the present one, is not ideally suited for being described with a Landau model, it could be shown that the applied methods can be successfully applied.

$CuInSe_2$ undergoes a structural phase transition from tetragonal chalcopyrite to cubic sphalerite structure type at 808°C. The structural changes occurring at the phase transition were described in terms of SM. For this transition, it was demonstrated that parametric Rietveld refinement offers advantages with respect to traditional sequential Rietveld refinement as it reduces the estimated standard deviations of parameters leading to more reliable results.

The monoclinic-cubic phase transition of $[Mg(H_2O)_6]RbBr_3$, which happens at 138°C, was described using all previously described methods (AC, SM, RB and RM). During the phase transition the $Mg(H_2O)_6$ octahedra experience a substantial rigid-body rotation. The sequential refinement using AC is of sufficient quality, though the trends of the single parameters are not unambiguous due to correlation of parameters. In parametric Rietveld refinement, some trends of atomic positions are difficult to model, making AC futile for the present case. Using SM, both sequential and parametric refinements are of decent quality, though care has to be taken in the choice

of starting values and during refinements. Both RB and RM result in stable sequential and parametric refinement. The resulting esd's for the RM approach are relatively smaller making RM especially effective for this phase transition.

Furthermore the photodimerization of 9-methylanthracene was studied by time resolved X-ray powder diffraction. The application of quantitative parametric Rietveld refinement allowed extracting information about phase transformations kinetics using the Johnson-Mehl-Avrami-Kolmogorov model directly from powder diffraction data with high accuracy.

The dependence of preparation conditions on the properties of nanomaterials and their growth kinetics was studied using Whole Powder Pattern Modelling (WPPM). This method allows modelling X-ray powder diffraction pattern using the microstructure of the sample without the use of arbitrary profile functions. The Fourier transforms of frequently observed effects as crystallite shape and size distribution or density of various defects, like dislocations and stacking faults, are utilised in order to get the resulting diffraction profile. Two different systems with industrial application, CeO_2 and Cu_2ZnSnS_4, which were produced using a sol-gel approach, were investigated.

A set of ceria specimens was produced from cerium isopropoxide with and without the addition of water or of acetylacetone as chelating agent. A heat treatment performed at 80°C, aimed to remove the solvent, proved to be sufficient to start agglomeration and thus the incorporation of defects in the growing domains.

The isothermal growth of ceria was studied at 300°C, 350°C and 400°C. Several models were applied leading to comparable results of the activation energy of nanocrystalline growth which was determined to be about 50 kJ/mol. The mechanism of growth can be explained by processes occurring at the domain surface.

The domain growth of Cu_2ZnSnS_4 thin films and powders, which were prepared using three different solvents, was investigated by isothermal and isochronal high temperature synchrotron X-ray diffraction. It could be shown that diffraction line

profile analysis of powder diffraction data collected *in-situ* can be a valuable tool to follow growth kinetics in nanocrystalline materials.

Depending on the solvent used in preparation both, the activation energy of the Cu_2ZnSnS_4 growth process and the mechanism of growth proved to be different. Moreover, the stability of the starting sol and therefore the actual chemical composition of the obtained Cu_2ZnSnS_4 strongly depend on the solvent. However, the optical properties of the films are not influenced. A thermal treatment at high temperature (500°C) leads to a removal of residual material from preparation, e.g. chlorine. Tentative solar cells could be produced using any solvent. The best performing cell, with an efficiency of 0.5 %, was obtained from an ethanol based sol after thermal treatment.

6   Zusammenfassung

Pulverröntgenbeugung ist eine gängige Technik um strukturelle und mikrostrukturelle Eigenschaften von Materialen zu charakterisieren. Die Abhängigkeit dieser Eigenschaften von den Umgebungsbedingungen (wie z. B. Temperatur oder Druck) kann mittels *in-situ* Pulverröntgenbeugung untersucht werden. In der vorliegenden Arbeit wurde *in-situ* Pulverröntgenbeugung dazu verwendet, die strukturellen sowie mikrostrukturellen Veränderungen verschiedener Materialien, die bei erhöhten Temperaturen oder unter Einwirkung von UV-Licht auftreten, zu untersuchen.

Mehrere strukturelle Phasenumwandlungen wurden mit Hilfe von parametrischer Rietveldverfeinerung analysiert. Die parametrische Rietveldverfeierung verfeinert einen Satz von Pulverröntgendaten simultan, wobei der Verlauf mancher Parameter durch mathematische Modelle gegeben ist, so dass, statt der einzelnen Parameterwerte, nur die Parameter des Modells bestimmt werden müssen. Um das Verhalten von Parametern der Kristallstruktur über einen Phasenübergang hinweg zu untersuchen und interpretieren, wurde die Landautheorie sowie die damit verbundenen Gleichungen verwendet, da strukturelle Eigenschaften (wie Gitterspannungen oder Änderungen in Atomposition- oder besetzung) einen Ordnungsparameter nach Landau darstellen.

Mehrere verschiedene Ansätze wurden zur Beschreibung der Kristallstruktur des untersuchten Materials verwendet:

1) Die traditionellen Atomkoordinaten können immer dazu verwendet werden um strukturelle Veränderungen im Zuge einer Phasenumwandlung nachzuvollziehen. Für Kristallstrukturen mit vielen Atomen auf generellen Positionen oder Phasenumwandlungen, die mit umfassenden Bewegungen von Atomgruppen einhergehen, sind andere Beschreibungen besser geeignet.

2) Symmetriemoden beschreiben eine Kristallstruktur in Abhängigkeit einer reellen oder hypothetischen höher symmetrischen Struktur. Daher ist dieses Modell ideal dazu geeignet um strukturelle Phasenumwandlungen zu untersuchen Im Vergleich mit den zuvor beschriebenen Atomkoordinaten

reduziert sich häufig die Anzahl der benötigten Parameter, da nur ein Teil der möglichen Symmetriemoden bei einer Phasenumwandlung aktiv ist. Symmetriemoden sind ideal dazu geeignet um Phasenumwandlungen mit linearen Bewegungen einzelner Atome zu beschreiben.

3) Phasenumwandlungen mit Rotationen von festen Gruppen von Atomen würden erzwingen, dass Symmetriemoden zusammenwirken um solche Bewegungen zu ermöglichen. Stattdessen können solche Bewegungen von festen Atomgruppen (rigid bodies) untersucht werden, wenn man Position und Orientierung der Atomgruppe verfolgt.

4) Um den im vorherigen Punkt (3) vorgestellten Ansatz noch weiter zu vereinfachen und zu verbessern, wurden sogenannte „rigid body symmetry modes" entwickelt, die die Bewegung fester Einheiten, die bei Phasenumwandlungen auftreten, beschreiben. Diese Methode verwendet Eigenschaften der Symmetriemoden in Kombination mit Rotationen fester Atomgruppen und ist daher besonders effektiv, wenn Phasenumwandlungen durch Bewegungen von Polyeder beschreiben werden können.

Die temperaturabhängige Phasenumwandlung von $CsFeO_2$ zwischen seiner orthorhombischen und kubischen Phase, welche bei 80°C stattfindet, wurde mittels Symmetriemodenanalyse und unter Verwendung von Rotationen fester Struktureinheiten untersucht. Diese Methoden sind sehr ähnlich und ergeben eine vergleichbare Beschreibung der Phasenumwandlung. Obwohl eine Phasenumwandlung erster Ordnung, wie diese, weniger gut geeignet ist, um mit einem auf der Landautheorie basierenden Modell beschrieben zu werden, konnte dieser Ansatz erfolgreich verwendet werden.

$CuInSe_2$ zeigt eine strukturelle Phasenumwandlung von einer tetragonalen Chalkopyrit- zu einer kubischen Sphaleritstruktur bei 808°C. Die auftretenden strukturellen Veränderungen wurden mittels Symmetriemoden beschrieben. Dabei konnte gezeigt werden, dass die parametrische Rietveldverfeinerung Vorteile im Vergleich mit der sequentiellen Rietveldverfeinerung bietet, da die

Standardabweichung der Parameter reduziert wird und somit die Ergebnisse verlässlicher werden.

Die Phasenumwandlung zwischen monoklinem und kubischem [Mg(H$_2$O)$_6$]RbBr$_3$, welche bei 138°C stattfindet, wurde mit allen zuvor vorgestellten Methoden untersucht. Die Struktur des Materials kann durch zwei verschiedene Oktaeder (Mg(H$_2$O)$_6$ und RbBr$_6$) beschrieben werden. Im Zuge der Phasenumwandlung rotieren die Mg(H$_2$O)$_6$ Oktaeder beträchtlich. Die Trends, die für die einzelnen Parametern durch sequentielle Verfeinerung mit traditionellen Atomkoordinaten erhalten werden, sind nicht eindeutig, da die Parameter untereinander korrelieren. In der parametrischen Verfeinerung ist das Verhalten einiger Atompositionen schlecht zu beschreiben, was diesen Ansatz für die vorliegende Umwandlung sinnlos macht. Die Qualität der sequentiellen und parametrischen Verfeinerung mit Symmetriemoden ist jeweils gut, jedoch muss für die parametrische Verfeinerung auf eine gute Wahl der Startwerte und eine sorgfältige Verfeinerung geachtet werden. Die beiden anderen Methoden ergeben stabile Ergebnisse sowohl für die sequentielle wie auch für die parametrische Verfeinerung. Unter Verwendung der neuentwickelten „rigid body symmetry modes" reduziert sich die relative Standardabweichung wodurch diese Methode daher besonders geeignet für die vorliegende Phasenumwandlung ist.

Außerdem wurde die Photodimerisation von 9-Methylanthracen mittels zeitaufgelöster Pulverröntgenbeugung untersucht, da so Nachteile einer Einkristalluntersuchung umgangen werden können. Die Anwendung quantitativer parametrischer Rietveldverfeinerung ermöglichte es genaue Informationen über die Umwandlungskinetik mit dem Johnson-Mehl-Avrami-Kolmogorov-Model direkt aus den Röntgenbeugungsdaten zu erhalten.

Whole Powder Pattern Modelling wurde dazu verwendet, den Einfluss der Herstellungsbedingungen auf Nanomaterialien und ihr Wachstum zu untersuchen. Whole Powder Pattern Modelling modelliert Röntgenbeugungsdaten mit Hilfe der Mikrostruktur des untersuchten Materials ohne willkürlich gewählte Profilfunktionen zu verwenden. Stattdessen werden beobachtbare Effekte, wie die Form und

Größenverteilung der kristallinen Domänen oder ihre Defektdichte (z.B. durch Versetzungen oder Stapelfehler) genützt.

Für die vorliegende Arbeit wurden Untersuchungen an zwei Materialien mit (potentieller) industrieller Anwendung, CeO_2 und Cu_2ZnSnS_4, durchgeführt. Die Materialsynthese erfolgte mittels Sol-Gel-Methoden.

Verschieden CeO_2-Proben wurden aus Cerium-Isopropoxid hergestellt. Dabei wurden teilweise Wasser oder der Komplexbildner Acetylaceton der Synthese zugegeben. Durch eine Wärmebehandlung bei 80°C, die das erhaltene Material trocken sollte, wurde bereits ein beginnendes Sintern verursacht, wodurch Defekte in die Domänen eingebaut wurden. Verschiedene Modelle wurden dazu verwendet das Wachstum von nanokristallinem CeO_2 zu modellieren, wobei jeweils in etwa eine Aktivierungsenergie von 50kJ/mol erhalten wurde. Der Wachstumsprozess findet an der Oberfläche der einzelnen Domänen statt.

Das Domänenwachstum dünner Schichten und Pulvern aus Cu_2ZnSnS_4, die mit drei verschiedenen Lösemitteln hergestellt wurden, wurde mit temperaturabhängiger Synchrotronröntgenbeugung untersucht. Es wurden isotherme und isochrone Messungen durchgeführt. Es konnte gezeigt werden, dass Linienprofileanalyse von *in-situ* Röntgenbeugungsdaten gut dazu geeignet ist um das Wachstum nanokristalliner Materialien zu untersuchen.

Der Einfluss des Lösemittels zeigte sich sowohl bei der Aktivierungsenergie wie auch beim Wachstumsprozess des erhaltenen Materials. Auch die Stabilität des erhaltenen Sols sowie die tatsächliche chemische Zusammensetzung des daraus erhaltenen Cu_2ZnSnS_4 hängen vom Lösemittel ab. Die optischen Eigenschaften der erhaltenen dünnen Schichten sind jedoch davon unabhängig. Eine Temperaturbehandlung bei hohen Temperaturen (500°C) entfernt Rückstande, die von den zur Synthese eingesetzten Chemikalien stammen, wie zum Beispiel Chlor. Provisorische Solarzellen konnten für alle Lösemittel hergestellt werden. Die leistungsfähigste Solarzelle, mit einer Effektivität von 0.5 %, wurde von einem Sol mit Ethanol als Lösungsmittel nach Hochtemperaturbehandlung erhalten.

7   References

Aegerter M. A. , Almeida R., Soutar A., Tadanaga K., Yang H. & Watanabe T.: *Coatings made by sol–gel and chemical nanotechnology*. Journal of Sol-Gel Science and Technology (2008) 47(2), 203–236.

Ali N. Z., Nuss J., Sheptyakov D. & Jansen M.: *The AFeO$_2$ (A = K, Rb and Cs) family: A comparative study of structures and structural phase transitions*. Journal of Solid State Chemistry (2010) 183(3), 752–759.

Allen A. J., Hackley V. A., Jemian P. R., Ilavsky J., Raitano J. M. & Chan S.-W.: *In situ ultra-small-angle X-ray scattering study of the solution-mediated formation and growth of nanocrystalline ceria*. Journal of Applied Crystallography (2008) 41(5), 918–929.

Almeida R. M. & Xu J. (2005): *Sol gel processing of sulfide materials*. In: Sakka S. (Edt.): Handbook of Sol-gel Science and Technology: Processing, Characterization and Applications: Volume 1: Sol-Gel Processing, Kluwer Academic Publishers, Dordrecht.

Als-Nielsen J. A. & Dietrich O. W.: *Long-Range Order and Critical Scattering of Neutrons below the Transition Temperature in β-Brass*. Physical Review (1967) 153(3), 717–721.

Avrami M.: *Kinetics of phase change I - General theory*. Journal of Chemical Physics (1939) 7 (12), 1103–1112.

Bärnighausen H.: *Group-Subgroup Relations between Space Groups: a useful tool in Crystal Chemistry*. MATCH: Communications in Mathematical Chemistry (1980) 9, 139–175.

Bell P. R.: *The Use of Anthracene as a Scintillation Counter*. Physical Review (1948) 73(11), 1405–1406.

Benedict J. B. & Coppens P.: *Kinetics of the Single-Crystal to Single-Crystal Two-Photon Photodimerization of α-trans-Cinnamic Acid to α-Truxillic Acid*. Journal of Physical Chemistry A (2009) 113(13), 3116–3120.

Bertmer M., Nieuwendaal R. C., Barnes A. B. & Hayes S. E. J.: *Solid-State Photodimerization Kinetics of α-trans-Cinnamic Acid to α-Truxillic Acid Studied via Solid-State NMR*. Journal of Physical Chemistry B (2006) 110(12), 6270–6273.

Bish D. L. & Howard S. A.: *Quantitative Phase Analysis Using the Rietveld Method.* Journal of Applied Crystallography (1988) 21(2), 86–91.

Bloss F. D. (1994): *Crystallography and Chrystal Chemistry*. Mineralogical Society of America, Washington D. C..

Bouas-Laurent H., Castellan A., Desvergne J.-P. & Lapouyade R.: *Photodimerization of anthracenes in fluid solution: structural aspects*. Chemical Society Reviews (2000) 29(1), 43–55.

Bragg W. L.: *The Diffraction of Short Electromagnetic Waves by a Crystal.* Proceedings of the Cambridge Philosophical Society (1913) 17, 43–57.

Bratschkov C., Karpuzova P., Müllen K., Klapper M. & Schopov I.: *Synthesis and photochemical transformations of an anthracene containing methacrylic copolymer*. Polymer Bulletin (2001) 46(5), 345–349.

Bruker AXS (2009): TOPAS version 4.2, Karlsruhe, Germany.

Campbell B. J., Stokes H. T., Tanner D. E. & Hatch D. M.: *ISODISPLACE: a web-based tool for exploring structural distortions.* Journal of Applied Crystallography (2006) 39(4), 607–614.

Campbell B. J., Evans J. S. O., Perselli F. & Stokes H. T.: *Rietveld refinement of structural distortion-mode amplitudes.* IUCr Computing Commission Newsletter (2007) 8, 81–95.

Chakhmouradian A. R., Ross K., Mitchell R. H. & Swainson I.: *The crystal chemistry of synthetic potassium bearing neighborite, $(Na_{1-x}K_x)MgF_3$.* Physics and Chemistry of Minerals (2001) 28(4), 277-284.

Cheary R. W. & Coelho A.: *A fundamental parameters approach to X-ray line-profile fitting*. Journal of Applied Crystallography (1992) 25(2), 109–121.

Chen S., Gong X. G., Walsh A. & Wei S.-H.: *Crystal and electronic band structure of Cu_2ZnSnX_4 (X=S and Se) photovoltaic absorbers: First-principles insights*. Applied Physics Letters (2009) 94(4), 041903.

Chen S., Gong X. G., Walsh A., Wei S.: *Defect physics of the kesterite thin-film solar cell absorber Cu_2ZnSnS_4*. Applied Physics Letters (2010) 96(2), 021902.

Chern G. C. & Lauks I.: *Spin-coated amorphous chalcogenide films*. Journal of Applied Physics (1982) 53(10), 6979–6982.

Christian, J. W. (1965): *The Theory of Transformations in Metals and Alloys*. Pergamon press, Oxford.

Chory C., Parisi J. & Riedel I. (2010) patent WO/2010/094779.

Cowley R. A.: *Structural phase transitions I. Landau theory*. Advances in Physics (1980) 29(1), 1–110.

Delbos S.: *Kësterite thin films for photovoltaics: a review*. EPJ Photovoltaics (2012) DOI: 10.1051/epjpv/2012008.

De Smedt J. & Keesom W. H.: *Das Gitter des festen Kohlendioxyds*. Zeitschrift für Kristallographie (1925) 62, 312–313.

Di Maggio R., Campostrini R., Guella G.: *Gels from modified zirconium N-butoxide: A pyrolysis study by coupled thermogravimetry, gas chromatographic, and mass spectrometric analyses*. Chemistry of Materials (1998) 10(12), 3839–3847.

Dinnebier R. E.: *Rigid Bodies in Powder Diffraction: A Practical Guide*. Powder Diffraction (1999) 14(2), 84–92.

Dinnebier R. E. & Billinge S. J. L. (2008): *Principles of Powder Diffraction*. In: Dinnebier, R. E. & Billinge S. L. J. (Edts.): Powder Diffraction − Theory and Practice. RSC Publishing, Cambridge.

Dinnebier R. E., Liebold-Ribeiro Y. & Jansen M.: The Low and High Temperature Crystal Structures of $[Mg(H_2O)_6]XBr_3$ Double Salts (X = Rb, Cs) Zeitschrift für anorganische und allgemeine Chemie (2008) 634(11), 1857–1862.

Dinnebier R. E. & Müller M. (2012): *Modern Rietveld refinement, a practical guide*. In: Mittemeijer E. J. & Welzel U. (Edts.): Modern Diffraction Methods. Wiley-VCH.

Dvornikov A. S. & Rentzepis P. M.: *Anthracene Monomer-Dimer Photochemistry: High Density 3D Optical Storage Memory*. Research on Chemical Intermediates (1996) 22(2), 115–128.

Ehrenfest P.: *Phasenumwandlungen im ueblichen und erweiterten Sinn, classifiziert nach den entsprechenden Singularitaeten des thermodynamischen Potentiales*. Proceedings Koninklijke Akademie van Wetenschappen (1933) 36, 153–157.

Emons H.-H., Naumann R., Pohl T., Voigt H.: *Thermoanalytical investigations on the decomposition of double salts*. Journal of Thermal Analysis and Calorimetry (1984) 29(3), 571–579.

Emons H.-H., Voigt H., Pohl T. & Naumann R.: *Thermoanalytical investigations on the decomposition of double salts: Part II. The decomposition of double salts $MeCl \cdot MgCl_2 \cdot 6H_2O$ (Me = NH_4, Rb, Cs)*. Thermochimica Acta (1987) 121, 151–163.

Emons H.-H., Voigt H., Pohl T. & Naumann R.: *Thermoanalytical investigations on the decomposition of double salts: Part III. The decomposition of double salts $MBr \cdot MgBr_2 \cdot 6H_2O$*, Journal of Thermal Analysis and Calorimetry (1991) 37(7), 1605–1619.

Fischereder A., Rath T., Haas W., Amentisch H., Albering J., Meischler D., Larissegger S., Edler M., Saf R., Hofer F. & Trimmel G.: *Investigation of Cu_2ZnSnS_4 Formation from Metal Salts and Thioacetamide*. Chemistry of Materials (2010) 22(4), 3399–3406.

Frisch G. & Röhr C.: *$Cs_6[Fe_2O_6]$ and $Rb_4[Fe_2O_5]$: New oxoferrates(III) with edge sharing FeO_4 tetrahedra*. Zeitschrift für Kristallographie (2005) 220(2), 135–141.

Giddy A. P., Dove M. T. & Heine V.: *What do Landau free energies really look like for structural phase transitions?* Journal of Physics: Condensed Matter (1989) 1(44), 8327–8335.

Goodwin A. L., Redfern S. A. T., Dove M. T., Keen D. A. & Tucker M. G.: *Ferroelectric nanoscale domains and the 905 K phase transition in SrSnO3: A neutron total-scattering study*. Physical Review B (2007) 76(17), 174114.

Grundy P. J., Lacey E. T. M. & Wright C. D.: *Stability and Microstructural Phenomena in RE-TM Films for Thermo-Magneto-optic Recording*. IEEE Transactions on Magnetics (1987) 23(5), 2632–2634.

Hammersley A. P., Svensson S. O., Hanfland M., Fitch A. N. & Häusermann D.: *Two-Dimensional Detector Software: From Real Detector to Idealised Image or Two-Theta Scan*. High Pressure Research (1996) 14(4-6), 235–248.

Han W.-Q. (2012): *One-Dimensional Oxygen-Deficient Metal Oxides*. In: Wu J., Cao J., Han W.-Q., Janotti A. & Kim H.-C.: Functional Metal Oxide Nanostructures, Springer, New York.

Hancock J. D. & Sharp J. H.: *Method of Comparing Solid-State Kinetic Data and Its Application to the Decomposition of Kaolinite, Brucite, and BaCO$_3$.* Journal of the American Ceramic Society (1972) 55(2), 74–77.

Hewat A. W.: *Cubic-tetragonal-orthorhombic-rhombohedral ferroelectric transitions in perovskite potassium niobate: neutron powder profile refinement of the structures.* Journal of Physics C: Solid State Physics (1973) 6(16), 2559–2572.

Hill R. J. & Howard C. J.: *Quantitative phase analysis from neutron powder diffraction data using the Rietveld method.* Journal of Applied Crystallography (1987) 20(6), 467–474.

Hinrichsen B., Dinnebier R. E. & Jansen M.: *Powder3D: An easy to use programm for data reduction and graphical presentation of large numbers of powder diffraction patterns.* Proceedings of European Powder Diffraction Conference (EPDIC 9), Prague, Czech Republic, 2004. Zeitschrift für Kristallographie Supplement 23 (2006), 231–236.

Huang F., Zhang H. & Banfield J. F.: *Two-Stage Crystal-Growth Kinetics Observed during Hydrothermal Coarsening of Nanocrystalline ZnS.* NANO LETTERS (2003) 3(3), 373–378.

Jackson P., Hariskos D., Lotter E., Paetel S., Wuerz R., Menner R., Wischmann W. & Powalla M.: *New world record efficiency for Cu(In,Ga)Se$_2$ thin film solar cells beyond 20%.* Progress in Photovoltaics: Research and Application (2011) 19(7), 894–897.

Johnson W. A. &. Mehl R. F: *Reaction Kinetics in processes of nucleation and growth.* Transactions of American Institute of Mining and Metallurgical Engineers (1939) 135, 416–458.

Kameyama T., Osaki T., Okazaki K., Shibayama T. Kudo A. Kuwabata S. & Torimoto T.: *Preparation and photoelectrochemical properties of densely immobilized Cu$_2$ZnSnS$_4$ nanoparticle films.* Journal of Materials Chemistry (2010) 20(25), 5319–5324.

Kamoun N., Bouzouita H. & Rezig B.: *Fabrication and characterization of Cu$_2$ZnSnS$_4$ thin films deposited by spray pyrolysis technique.* Thin Solid Films (2007) 515(15), 5949–5952.

Katagiri H., Ishigaki N. & Ishida T.: *Characterization of Cu_2ZnSnS_4 Thin Films Prepared by Vapor Phase Sulfurization*. Japanese Journal of Applied Physics (2001) 40(2), 500–504.

Kerman S., Campbell B. J., Satyavarapu K. K., Stokes H. T., Perselli F. & Evans J. S. O.: *The superstructure determination of displacive distortions via symmetry-mode analysis.* Acta Crystallographica (2012) A68(2), 222–234.

Khattak C. P. & Cox D. E.: *Profile analysis of X-ray powder diffractometer data: structural refinement of $La_{0.75}Sr_{0.25}CrO_3$.* Journal of Applied Crystallography (1977) 10(5), 405–411.

Kim S., Kim W. K., Kaczynski R. M., Acher R. D., Yoon S., Anderson T. J., Crisalle O. D., Payzant E. A. & Li, S. S.: *Reaction kinetics of $CuInSe_2$ thin films grown from bilayer InSe/CuSe precursors*. Journal of Vacuum Science & Technology A (2005) 23(2), 310–315.

Kishore Kumar Y. B., Suresh Babu G., Uday Bhaskar P. & Sundara Raja V.: *Preparation and characterization of spray-deposited Cu_2ZnSnS_4 thin films*. Solar Energy Materials and Solar Cells (2009) 93(8), 1230–1237.

Kobayashi T., Jimbo K., Tsuchida K., Shinoda S., Oyanagi T. & Katagiri H.: *Investigation of Cu_2ZnSnS_4-Based Thin Film Solar Cells Using Abundant Materials*. Japanese Journal of Applied Physics (2005) 44(2), 783–787.

Kolmogorov A. N.: *Statistical theory of crystallization of metals.* (in russian), Izvestia Akademia Nauk SSSR Ser. Mathematica (1937) 1, 355–359.

Kopský V.: *What can the group theory say about the theory of phase transitions?*. Ferroelectrics (1980) 24(1), 3–10.

Krill C. E., Helfen L., Michels D., Natter H., Fitch A., Masson O. & Birringer R.: *Size-Dependent Grain-Growth Kinetics Observed in Nanocrystalline Fe*. Physical Review Letters (2001) 86(5), 842–845.

Landau L.: *On the theory of phase transition*. Originally published in: Pisma v Zhurnal Eksperimentalnoi i Teoreticheskoi Fiziki (1937), 19–32. English translation: Ukrainian Journal of Physics (2008) 53(special issue), 25–35.

Le Bail A., Duroy H. & Fourquet J. L.: *Ab-initio structure determination of $LiSbWO_6$ by X-ray powder diffraction.* Materials Research Bulletin (1988) 23, 447–452.

Le Bail A. (2008): *The Profile of a Bragg Reflection for Extracting Intensities.* In: Dinnebier R. E. & Billinge S. L. J. (Edts.): Powder Diffraction − Theory and Practice. RSC Publishing, Cambridge.

Leach A. (2001): *Molecular Modelling, Principles and Applications.* Pearson Education Limited, Harlow.

Lee J., Mahendra S. & Alvarez P. J. J.: *Nanomaterials in the Construction Industry: A Review of Their Applications and Environmental Health and Safety Considerations.* ACS Nano (2010) 4(7), 3580–3590.

Lee Y. & Choi S.: *Controlled nucleation and crystallization in Fe_2O_3–CaO–SiO_2 glass.* Journal of Material Science (1997) 32(2), 431–436.

Leoni, M. & Scardi, P.: *Nanocrystalline domain size distributions from powder diffraction data.* Journal of Applied Crystallography (2001) 37(4), 629–634.

Leoni M., Di Maggio R., Polizzi S. & Scardi P.: *X-ray Diffraction Methodology for the Microstructural Analysis of Nanocrystalline Powders: Application to Cerium Oxide.* Journal of the American Ceramic Society (2004) 87(6), 1133–1140.

Leoni M., Confente T. & Scardi P.: *PM2K: a flexible program implementing Whole Powder Pattern Modelling.* Zeitschrift für Kristallographie Supplements (2006) 23, 249–254.

Loopstra B. O.: *The phase transition in α-U_3O_8 at 210°C.* Journal of Applied Crystallography (1970) 3(2), 94–96.

Mabied F., Müller M., Dinnebier R. E., Nozawa S., Hoshino M., Tomita A., Sato T. & Adachi S.: *A Time-Resolved Powder Diffraction Study of In-situ Photodimerization Kinetics of 9-methylanthracene using a CCD Area Detector and Parametric Rietveld Refinement.* Acta Crystallographica (2012) B68(4), 424–430.

Malerba C., Biccari F., Azanza Ricardo C. L., Valentini M., Chierchia R., Müller M., Santoni A., Esposito E., Mangiapane P., Scardi P. & Mittiga A.: *CZTS stoichiometry effects on the band gap energy.* Journal of Alloy and Compounds (2014) 582, 528-534.

Malmros G. & Thomas J. O.: *Least squares structure refinement based on profile analysis of powder film intensity data measured on an automatic microdensitometer.* Journal of Applied Crystallography (1977) 10(1), 7–11.

Malow T. R & Koch C. C.: *Grain growth in nanocrystalline iron prepared by mechanical attrition*. Acta Materialia (1997) 45(5), 2177–2186.

Mann J. R., Vora N. & Repins I. L.: *In Situ Thickness Measurements of Chemical Bath Deposited CdS*. Solar Energy Materials and Solar Cells (2010) 94(2), 333–337.

Marsh R. E.: *Structure of $MgCl_2 \cdot RbCl_6 \cdot H_2O$. Corrigendum*. Acta Crystallographica (1992). C48, 218–219.

Martinez-Garcia J., Leoni M. & Scardi P.: *A general approach for determining the diffraction contrast factor of straight-line dislocations*. Acta Crystallographica (2009) A65(2), 109–119.

Mattox D. M. (1998). *Handbook of physical vapour deposition (PVD) processing*. Noyes Publications, Westwood.

Matusita K., Komatsu T. & Yokota R.: *Kinetics of non-isothermal crystallization process and activation energy for crystal growth in amorphous materials*. Journal of Material Science (1984) 19(1), 291–296.

Molard Y., Bassani D. M., Desvergne J.-P., Moran, N. & Tucker, J. H. R.: *Structural Effects on the Ground and Excited-state Properties of Photoswitchable Hydrogen-Bonding Receptors*. Journal of Organic Chemistry (2006) 71(22), 8523–8531.

Moriya K., Watabe J., Tanaka K. & Uchiki H.: *Characterization of Cu_2ZnSnS_4 thin films prepared by photochemical deposition*. Physica Status Solidi C (2006) 3(8), 2848–2852.

Moré R., Busse G., Hallmann J., Paulmann C., Scholz M. & Techert S.: *Photodimerization of Crystalline 9-Anthracenecarboxylic Acid: A Nontopotactic Autocatalytic Transformation*. Journal of Physical Chemistry C (2010) 114(9), 4142–4148.

Mountstevens E. H., Redfern S. A. T. & Attfield J. P.: *Order-disorder octahedral tilting transitions in $SrSnO_3$ perovskite*. Physical Review B (2005) 71(22), 220102.

Müller M., Dinnebier R. E., Jansen M., Wiedemann S. & Plüg C.: *Kinetic analysis of the phase transformation from α- to β-copper phthalocyanine: A case study for sequential and parametric Rietveld refinements*. Powder Diffraction (2009) 24(3), 191–199.

Müller M., Dinnebier R. E., Ali N. Z., Campbell B. & Jansen M.*: Direct Access to the Order Parameter: Parameterized Symmetry Modes and Rigid Body Movements as a Function of Temperature*. Materials Science Forum (2010), 651 79–95.

Müller M., Dinnebier R. E. & Schorr S.: *A case study of parameterized Rietveld refinement: The structural phase transition of CuInSe$_2$.* Zeitschrift für Kristallographie (2011) 226(12), 956–962.

Müller M., Dinnebier R. E., Dippel A.-C., Stokes H. T. & Campbell B. J.: *A symmetry-mode description of rigid-body-rotations in crystalline solids: a case study of Mg[H$_2$O]$_6$RbBr$_3$* (2013; submitted)

Müller M., Leoni M., Di Maggio R. & Scardi P.: *Defects in nanocrystalline ceria xerogel*. Zeitschrift für Kristallographie Proceedings (2011b) 1, 81-86.

Müller M., Azanza Ricardo C. L., Di Maggio R. & Scardi P.: *Growth kinetics of Cu$_2$ZnSnS$_4$ thin films and powders*. Powder Diffraction (2013b) S2, S228–S214.

Müller M., Azanza Ricardo C. L., Malerba C., Biccari F., Mittiga A., Maggini S., Di Maggio R. & Scardi P.: *Influence of different solvents on the properties of CZTS thin films prepared by sol-gel* (2013c; in preparation).

Müller U. (2012): *Symmetriebeziehungen zwischen verwandten Kristallstrukturen*, Vieweg & Teubner, Wiesbaden.

Nakayama N. & Ito K.: *Sprayed films of stannite Cu$_2$ZnSnS$_4$*. Applied Surface Science (1996) 92, 171–175.

Nichtová L., Kužel R., Matěj Z., Šícha J. & Musil J.: *Time and thickness dependence of crystallization of amorphous magnetron deposited TiO$_2$ thin films*. Zeitschrift für Kristallographie Supplement (2009) 30, 235–240.

Niemann M. U., Srinivasan S. S., Phani A. R., Kumar A. Goswami Y. & Stefanakos E. K.: *Nanomaterials for Hydrogen Storage Applications: A Review*. Journal of Nanomaterials (2008) doi:10.1155/2008/950967.

Norby P. & Schwarz U. (2008): *Powder Diffraction under Non-ambient Conditions.* In: Dinnebier, R. E. & Billinge S. L. J. (Edts.): Powder Diffraction – Theory and Practice. RSC Publishing, Cambridge.

Nozawa S. Adachi S., Takahashi J., Tazaki R., Guerin L., Daimon M., Tomita A., Sato T., Chollet M., Collet E., Cailleau H., Yamamoto S., Tsuchiya K., Shioya T., Sasaki H., Mori T., Ichiyanagi K., Sawa H., Kawata H. & Koshihara S.: *Developing 100 ps-resolved X-ray structural analysis capabilities on beamline NW14A at the Photon Factory Advanced Ring*. Journal of Synchrotron Radiation (2007) 14(4), 313–319.

Nuss J., Ali N. Z. & Jansen M.: *Structure of RbFeO$_2$, refined from a reticular pseudomerohedrally twinned crystal with six domains*. Acta Crystallographica (2007) B63(5), 719–725.

Olekseyuk I., Dudchak I. & Piskach L. V.: *Phase equilibria in the Cu$_2$S–ZnS–SnS$_2$ system*. Journal of Alloys and Compounds (2004) 368(1-2), 135–143.

Orobengoa D., Capillas C., Aroyo M. I. & Perez-Mato J. M.: *AMPLIMODES: symmetry-mode analysis on the Bilbao Crystallographic Server.* Journal of Applied Crystallography (2009) 42(5), 820–833.

Ostwald W.: *Studien über die Bildung und Umwandlung fester Körper*. Zeitschrift für Physikalische Chemie (1897) 22, 289–330.

Ozawa T.: *Kinetic analysis of derivative curves in thermal analysis*. Journal of Thermal Analysis (1970) 2(3), 301–324.

Paulik F. & Paulik J.: *Thermoanalytical examination under quasi-isothermal—quasi-isobaric conditions*. Thermochimica Acta (1986) 100(1), 23–59.

Pawley G. S.: *Unit-cell refinement from powder diffraction scans.* Journal of Applied Crystallography (1981) 14(6), 357–361.

Penn R. L. & Banfield J. F.: *Imperfect Oriented Attachment: Dislocation Generation in Defect-Free Nanocrystals*. Science (1998) 281(5379), 969–971.

Percharsky V. K. & Zavalij P. Y. (2009): *Fundamentals of Powder Diffraction and structural Characterization of Materials*, Springer, New York.

Perez-Mato J. M., Orobengoa D. & Aroyo M. I.: *Mode crystallography of distorted structures*. Acta Crystallographica (2010) A66(5), 558–590.

Pierron E. D., Rashkin J. A. & Roth J. F.: *Copper oxide on alumina: I. XRD studies of catalyst composition during air oxidation of carbon monoxide.* Journal of Catalysis (1967) 9(1), 38–44.

Popa N. C.: *Texture in Rietveld Refinement.* Journal of Applied Crystallography (1992) 25(5), 611–616.

Pyldme M. & Utsal K.: *Effect of water vapor upon thermal dehydration of $Mg(H_2PO_4)_2 \cdot 2H_2O$.* Journal of Thermal Analysis (1989) 35(6), 1953–1958.

Radescu S., Etxebarria I. & Perez-Mato J.M.: *The Landau free energy of the three-dimensional Φ^4 model in wide temperature intervals.* Journal of Physics: Condensed Matter (1995) 7(3), 585–595.

Rao C. N. R., Müller A. & Cheetham A. K. (Edts.) (2004): *The Chemistry of Nanomaterials*, Wiley-VCH, Weinheim.

Ribot F., Tolédano P. & Sanchez C.: *Hydrolysis-condensation process of β-diketonates-modified cerium(IV) isopropoxide.* Chemistry of Materials (1991) 3(4), 759–764.

Rietveld H. M: *Line Profiles of Neutron Powder-diffraction Peaks for Structure Refinement.* Acta Crystallografica (1967) 22(1), 151–152.

Rietveld H. M: *A Profile Refinement Method for Nuclear and Magnetic Structures.* Journal of Applied Crystallography (1969) 2(2), 65–71.

Rietveld H. M. (1993): *The early days: a retrospective view.* In: Young R.A. (Edt.): The Rietveld Method. Oxford University Press, Oxford.

Rodríguez C., Sanchez E., Hernández J., Prokhorov E., Saldaña J. & Martínez G.: *Estimate of the Crystallization Kinetics in Stoichiometry Compositions Films of Ge:Sb:Te.* Journal of Surface Engineered Materials and Advanced Technology, (2012) 2(1), 44–46.

Rupp J. L. M., Scherrer B. & Gauckler L. J.: *Engineering disorder in precipitation-based nano-scaled metal oxide thin films.* Physical Chemistry Chemical Physics (2010) 12(36), 11114–11124.

Salata O. V.: *Applications of nanoparticles in biology and medicine.* Journal of Nanobiotechnology (2004) 2(3) doi:10.1186/1477-3155-2-3-2.

Salje E. K. H. (1990): *Phase transitions in ferroelastic and co-elastic crystals*, Cambridge University press.

Šatava V.: *Mechanism and kinetics from non-isothermal TG traces*. Thermochimica Acta (1971) 2(5), 423–428.

Scardi P. & Leoni M.: *Whole powder pattern modelling.* Acta Crystallographica (2002) A58(2), 190–200.

Scardi P. & Leoni M. (2004): *Whole Powder Pattern Modelling: Theory and Applications.* In: Mittemeijer E.J & Scardi P. (Edts): Diffraction Analysis of the Microstructure of Materials, Springer-Verlag, Berlin.

Scardi P. & Leoni M.: *Advances in Line Profile Analysis for the Study of Nanocrystalline Systems*. ECS Transactions (2006) 3(9), 125–132.

Scardi P., Leoni M., & D'Incau M.: *Whole Powder Pattern Modelling of cubic metal powders deformed by high energy milling.* Zeitschrift für Kristallographie - Crystalline Materials (2007) 222(3-4), 129–135.

Scardi P., Leoni M., Müller M. & Di Maggio R.: *In situ size-strain analysis of nanocrystalline ceria growth*. Materials Science and Engineering: A (2010) 528(1), 77–82.

Scherrer P.: *Bestimmung der Größe und der inneren Struktur von Kolloidteilchen mittels Röntgenstrahlen.* Göttinger Nachrichten für Mathematik und Physik (1918) 2, 98–100.

Schmidt, G. M. J.: *Photodimerization in the Solid State*. Pure and Applied Chemistry (1971) 27(4), 647–678.

Schorr S. & Geandier G.: *In-situ investigation of the temperature dependent phase transition in $CuInSe_2$ by synchrotron radiation*. Journal of Crystal Research and Technology (2006) 41(5), 450–457.

Schorr S., Hoebler H. & Tovar M.: *A neutron diffraction study of the stannite kesterite solid solution series*. European Journal of Mineralogy (2007) 19(1), 65–73.

Schorr S. & Gonzalez-Aviles G.: *In-situ investigation of the structural phase transition in kesterite*. Physica Status Solidi *(a)* (2009) 206(5), 1054–1058.

Schubert U. & Hüsing N. (2012): *Synthesis of Inorganic Materials*, Wiley-VCH, Weinheim.

Shay J. L. & Wernick J. H. (1975): *Ternary Chalcopyrite Semiconductors: Growth, Electronic Properties and Applications*, Pergamon Press, Oxford.

Shockley W. & Queisser H. J.: *Detailed Balance Limit of Efficiency of p-n Junction Solar Cells*. Journal of Applied Physics (1961) 32(3), 510-519.

Shoval S., Yariv S., Kirsh Y. & Peled H.: *The effect of alkali halides on the thermal hydrolysis of magnesium chloride and magnesium bromide*. Thermochimica Acta (1986) 109(1), 207–226.

Sofin M., Peters E.-M. & Jansen M.: *Ein neuartiges Polyoxocobaltat(II)-Anion in $Rb_2Co_2O_3$*. Zeitschrift für allgemeine und anorganische Chemie (2002) 628(12), 2697–2700.

Solans X., Font-Altaba M., Aguilo M., Solans J. & V. Domenech: *Crystal form and structure of ammonium hexaaquamagnesium trichloride $NH_4[Mg(H_2O)_6]Cl_3$*. Acta Crystallographica (1983) C39(11), 1488–1490.

Spassov T., Lyubenova L., Köster U. & Baró M. D.: *Mg–Ni–RE nanocrystalline alloys for hydrogen storage*. Materials Science and Engineering: A (2004) 375–377, 794–799.

Sperling L. H. (1992). *Introduction to Physical Polymer Science*. John Wiley & Sons, New York.

Stephens P. W.: *Phenomenological model of anisotropic peak broadening in powder diffraction*. Journal of Applied Crystallography (1999) 32(2), 281–289.

Stinton G. W. & Evans J. S. O.: *Parametric Rietveld refinement*. Journal of Applied Crystallography 40(1) (2007), 87–95.

Stokes H. T., Hatch D. M. & Wells J. D.: *Group-theoretical methods for obtaining distortions in crystals: Applications of vibrational modes and phase transitions*. Physical Review B (1991) 43(13), 11010–11018.

Sun C., Li H. & Chen L.: *Nanostructured ceria-based materials: synthesis, properties and applications*. Energy & Environmental Science (2012) 5(9), 8475–8505.

Svensson S. O., Birch J., Moiler H. & Kvick A.: *Time-Resolved X-ray Powder Diffraction Using a Large-Area CCD-Based Detector and Rietveld Refinement: Solid-State Polymerization of S_2N_2 to $(SN)_x$*. Journal of Synchrotron Radiation (1997) 4(2), 83–94.

Takegoshi K., Nakamura S. & Terao T.: *Solid-state photodimerization of 9-methyl-anthracene as studied by solid-state ^{13}C NMR*. Solid State Nuclear Magnetic Resonance (1998) 11(3-4), 189–196.

Tanaka K., Moritake N. & Uchiki H.: *Preparation of Cu_2ZnSnS_4 thin films by sulfurizing sol – gel deposited precursors*. Solar Energy Materials and Solar Cells (2007) 91, 1199–1201.

Thompson P., Cox D. E. & Hastings J. B.: *Rietveld refinement of Debye-Scherrer synchrotron X-ray data from Al_2O_3*. Journal of Applied Crystallography (1987) 20(2), 79–83.

Todorov T., Kita M., Carda J. & Escribano P.: *Cu_2ZnSnS_4 films deposited by a soft-chemistry method*. Thin Solid Films (2009) 517(7), 2541–2544.

Turowska-Tyrk I. & Trzop E.: *Monitoring structural transformations in crystals: 6. The [4 + 4] photodimerization of 9-methylanthracene*. Acta Crystallographica (2003) B59(6), 779–786.

Turro N. J. (1991): *Modern Moelcular Photochemisty*. University Science Books, Sausolito.

Trinschek D. & Jansen M.: *Ein neuer, einfacher Zugang zu Alkalimetalloxometallaten*. Angewandte Chemie (1999) 11(1-2), 234–235 and Angewandte Chemie International Edition (1999) 38(1-2), 133–135.

Tsunekawa S., Sahara R., Kawazoe Y. & Ishikawa K.: *Lattice relaxation of monosize $CeO_{2−x}$ nanocrystalline particles*. Applied Surface Science (1999) 152(1-2), 53–56.

Tsudera T., Ikeda A. & Shinkai S.: *Light-switched Metal-tunneling across a π-Basic Tube of 1,3-Alternate-calix[4]arenes*. Tetrahedron (1997) 53(40), 13609–13620.

Ungár T. & Gubicza J.: *Nanocrystalline materials studied by powder diffraction line profile analysis*. Zeitschrift für Kristallographie - Crystalline Materials (2007) 222(3-4), 114–128.

Vaughan D. J. & Tossell J. A.: *The chemical bond and the properties of sulfide minerals. I. Zn, Fe and Cu in tetrahedral and triangular coordination with sulfur*. Canadian Mineralogist (1980) 18(2), 157–163.

Vegard L.: *Die Struktur derjenigen Form von festem Stickstoff, die unterhalb 35.5 °K stabil ist*. Zeitschrift für Physik (1929) 58(7-8), 497–510.

Wadhawan V. K.: *Ferroelasticity and related properties of crystals*. Phase Transitions - A Multinational Journal (1982) 3(1), 3–103.

Wang K., Shin B., Reuter K. B., Todorov T. K. Mitzi, D. B. & Guha, S.: *Structural and elemental characterization of high efficiency Cu$_2$ZnSnS$_4$ solar cells*. Applied Physics Letter (2011) 98(5), 051912.

Weber A., Mainz R., Unold T., Schorr S. & Schock H.-W.: *In-situ XRD on formation reactions of Cu$_2$ZnSnS$_4$ thin films*. Physica Status Solidi C (2009) 6(5), 1245–1248.

Wei S. & Zunger A.: *Band offsets and optical bowings of chalcopyrites and Zn-based II-VI alloys*. Journal of Applied Physics (1995) 78(6), 3846–3856.

Wernick D. L. & Schochet S.: *Kinetics of dimerization in stack crystal structures*. Journal of Physical Chemistry (1988) 92(23), 6773–6778.

Williamson G. K. & Hall W. H.: *X-Ray line broadening from filed aluminum and wolfram*. Acta Metallurgica (1953) 1(1), 22–31.

Yashima M., Kobayashi S. & Yasui T.: *Crystal structure and the structural disorder of ceria from 40 to 1497 °C*. Solid State Ionics (2006) 177(3-4), 211–215.

Yeh M. Y., Lee C. C. & Wuu D. S.: *Influences of synthesizing temperatures on the properties of Cu$_2$ZnSnS$_4$ prepared by sol – gel spin-coated deposition*. Journal of Sol-Gel Science and Technology (2009) 52, 65–68.

Young R. A., Mackie P. E. & Von Dreele R. B: *Application of the pattern-fitting structure-refinement method of X-ray powder diffractometer patterns.* Journal of Applied Crystallography (1977) 10(4), 262–269.

Zhang H. & Banfield J. F.: *Kinetics of Crystallization and Crystal Growth of Nanocrystalline Anatase in Nanometer-Sized Amorphous Titania*. Chemistry of Materials (2002) 14(10), 4145–4154.

Zhang J., Wang Y., Zheng J., Huang F., Chen D., Lan Y. Ren G. Lin Z. & Wang C.: *Oriented Attachment Kinetics for Ligand Capped Nanocrystals: Coarsening of Thiol-PbS Nanoparticles*. Journal of Physical Chemistry B (2003) 111(6), 449–454.

Zhang J., Huang F. & Lin Z.: *Progress of nanocrystalline growth kinetics based on oriented attachment*. Nanoscale (2010) 2(1), 18–34.

Zhou X.-D. & Huebner W.: *Size-induced lattice relaxation in CeO$_2$ nanoparticles*. Applied Physics Letters (2001) 79(21), 3512–3514.

Zouev I., Cao D.-K. Sreevidya T. V., Telzhensky M., Botoshanskya M. & Kaftory M.: *Photodimerization of anthracene derivatives in their neat solid state and in solid molecular compounds*. CrystEngComm (2011) 13(13), 4376–4381.

Zuñiga F. J., Capuis G., Mañes J. L., Perez-Mato J. M. & Tello M. J.: *Group theoretical analysis of the structural phase transition sequence in the quasi-one dimensional compound ((CH$_3$)$_3$NH)CdCl$_3$*. Journal of Physics C: Solid State Physics (1982) 15(25), 5192-5201.

List of Tables

List of Figures

Curriculum Vitae

Name:	Melanie Müller
Date of birth:	20. August 1980
Place of birth:	Stuttgart, Germany
Nationality:	German

Education:

since 11/2009:	PhD student at the Doctoral School in Materials Science and Engineering at the University of Trento (Italy)
since 04/2009:	PhD student at Max-Planck-Institute for Solid State Research, Stuttgart (Germany)
03/2009:	degree in mineralogy (emphasis: crystallography)
03/2008 – 02/2009:	diploma thesis: Kinetics of phase transformations of copper phthalocyanine pigments, Max-Planck-Institute for Solid State Research, Stuttgart (Germany)
10/2002 – 03/2009:	studies of geosciences (specialisation: mineralogy/ crystallography), University of Tübingen (Germany) and University of Stuttgart (Germany)
10/2000 – 09/2002:	studies of physics, University of Stuttgart (Germany)
07/2000:	graduation from school

Publications

1) M. Müller, R. E. Dinnebier, M. Jansen, S. Wiedemann and C. Plüg: *Kinetic analysis of the phase transformation from α- to β-copper phthalocyanine: A case study for sequential and parametric Rietveld refinements*. Powder Diffraction (2009) 24(3), 191-199.

2) M. Müller, R. E. Dinnebier, M. Jansen, S. Wiedemann and C. Plüg: *The influence of temperature, additives and polymorphic form on the kinetics of the phase transformation of copper phthalocyanine*. Dyes and Pigments (2010) 85(3), 152-161.

3) M. Müller, R. E. Dinnebier, N. Z. Ali, B. J. Campbell and M. Jansen: *Direct Access to the Order Parameter: Parameterized Symmetry Modes and Rigid Body Movements as a Function of Temperature*. Materials Science Forum (2010) 651, 79-95.

4) P. Scardi, M. Leoni, M. Müller and R. Di Maggio: *In situ size-strain analysis of nanocrystalline ceria growth*. Materials Science and Engineering: A (2010) 528(1), 77–82.

5) M. Müller, M. Leoni, R. Di Maggio and P. Scardi: *Defects in nanocrystalline ceria xerogel*. Zeitschrift für Kristallographie Proceedings (2011) 1, 81-86.

6) M. Müller, R. E. Dinnebier and S. Schorr: *A case study of parameterized Rietveld refinement: The structural phase transition of $CuInSe_2$.* Zeitschrift für Kristallographie (2011) 226(12), 956–962.

7) F. Mabied, M. Müller, R. E. Dinnebier, S. Nozawa, M. Hoshino, A. Tomita, T. Sato and S. Adachi: *A Time-Resolved Powder Diffraction Study of In-situ Photodimerization Kinetics of 9-methylanthracene using a CCD Area Detector and Parametric Rietveld Refinement*. Acta Crystallographica B (2012) 68, 424-430.

8) R. E. Dinnebier and M. Müller: *Modern Rietveld refinement, a practical guide*. In: Modern Diffraction Methods, edited by E. J. Mittemeijer and U. Welzel (2012) (Wiley, Germany)

9) C. L. Azanza Ricardo, M. S. Su'ait, M. Müller and P. Scardi: *Production and structural characterization of high energy ball-milled $Cu_2(Zn,Fe)SnS_4$*. Journal of Powder Sources (2013) 230, 70-75.

10) M. Müller, C. L. Azanza Ricardo, R. Di Maggio and P. Scardi: *Growth kinetics of Cu_2ZnSnS_4 thin films and powders*. Powder Diffraction (2013) S2, S228-S241.

11) C. Malerba, F. Biccari, C. L. Azanza Ricardo, M. Valentini, R. Chierchia, M. Müller, A. Santoni, E. Esposito, P. Mangiapane, P. Scardi and A. Mittiga: *CZTS stoichiometry effects on the band gap energy*. Journal of Alloy and Compounds (2014) 582, 528-534.

12) M. Etter, M. Müller, M. Hanfland and R. E. Dinnebier: *Possibilities and limitations of parametric Rietveld refinement on high pressure data: The case study of $LaFeO_3$* (accepted, Zeitschrift für Kristallographie)

13) O. V. Magdysyuk, M. Müller, R. E. Dinnebier, C. Lipp and T. Schleid: *Parameterization of the coupling between strain and order parameter for $LuF[SeO_3]$* (submitted).

14) M. Etter, M. Müller, M. Hanfland and R. E. Dinnebier: *High pressure phase transitions in the rare-earth orthoferrite $LaFeO_3$* (submitted).

15) M. Müller, R. E. Dinnebier, A.-C. Dippel, H. T. Stokes and B. J. Campbell: *A symmetry-mode description of rigid-body-rotations in crystalline solids: a case study of $Mg[H_2O]_6RbBr_3$* (submitted)

16) M. Müller, C. L. Azanza Ricardo, C. Malerba, F. Biccari, A. Mittiga, S. Maggini, R. Di Maggio and P. Scardi: *Influence of different solvents on the properties of CZTS thin films prepared by sol-gel* (in preparation).

Erklärung über die Eigenständigkeit der Dissertation

Ich versichere, dass ich die vorliegende Arbeit mit dem Titel „Advances in the modelling of *in-situ* powder diffraction data" selbständig verfasst und keine anderen als die angegebenen Quellen und Hilfsmittel benutzt habe; aus fremden Quellen entnommene Passagen und Gedanken sind als solche kenntlich gemacht.

Melanie Müller   Stuttgart, 08.10.2013

Declaration of Authorship

I hereby certify that the dissertation entitled "Advances in the modelling of *in-situ* powder diffraction data" is entirely my own work except where otherwise indicated. Passages and ideas from other sources have been clearly indicated.

Melanie Müller   Stuttgart, 08.10.2013

Acknowledgements